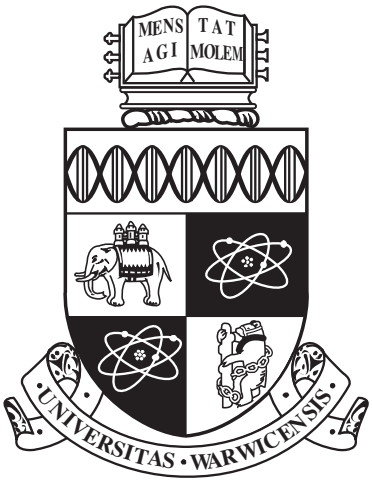

A Network Analysis of Space Weather

by

Joe Dods

Thesis

Submitted to the University of Warwick

for the degree of Doctor of Philosophy

Doctor of Philosophy

Physics

THE UNIVERSITY OF
WARWICK

Contents

Glossary

AMIE Assimilative Mapping of Ionospheric Electrodynamics.

CD Current Disruption.

EUV Extreme Ultra Violet.

FAC Field Aligned Current.

HLBL High Latitude Boundary Layer.

IMF Interplanetary Magnetic Field.

LLBL Low Latitude Boundary Layer.

MHD Magnetohydrodyanmics.

MLat Magnetic Latitude.

MLT Magnetic Local Time.

NENL Near Earth Neutral Line.

PSBL Plasma Sheet Boundary Layer.

SMC Steady Magnetic Convection.

Acknowledgments

I thank my supervisor Prof. Sandra C. Chapman for her help, patience and ideas as well as our collaborator Jesper Gjerloev for many fruitful discussions. I would also like to thank my friends and family for their support.

Declarations

I declare that the work presented in this thesis is my own original work, unless otherwise indicated, and has not been submitted, partially or entirely, for the attainment of a degree in this or other academic institution. All the work presented here was carried out during the period from October 2012 to September 2016 under the supervision of Prof. Sandra C. Chapman.

Abstract

Geomagnetic perturbations (space weather) can have a significant impact for an ever increasingly technological society. Substorms can cause disturbances that effect radio communication and technologies such as magnetic guidance drilling. Understanding the processes underlying space weather has been a central topic of magnetospheric research for several decades. While current advances in research have been driven by in-situ satellite based observations, historically magnetic field perturbations that were measured from ground and inspected by the human eye were used. With the inception of SuperMAG, an initiative the collates and processes the data from almost all ground magnetometer stations observations into a single repository, new ways of analysing this historical data are now possible.

In this thesis we use a dynamical network framework to analyse the magnetospheric/ionospheric system for the time. We utilise all available ground based magnetometer measurements in the northern hemisphere to construct dynamical networks. The stations are connected in the network when the correlation between the vector magnetometer time series from pairs of stations within a running time window exceeds a threshold. We develop methods to optimise the choice of correlation threshold to account for the differing local characteristics of the different magnetometer station groups.

We use this framework to approach two different aspects of magnetopheric research. We apply network methodology to analyse four isolated substorm test cases as well as a steady magnetic convection (SMC) event and a day in which no substorms occur. The events were chosen so as to have similar magnetometer station coverage at the onset of the events. Dimensionless parameters can then be obtained that characterise the network and by extension, the spatio-temporal dynamics of the substorms under observation. These test case substorms are found to give a consistent characteristic network response at onset in terms of their spatial correlation. Such responses are differentiable from responses to the SMC event and non-substorm times.

We also characterise the response of the quiet-time large scale ionospheric convection system to north-south and south-north interplanetary magnetic field (IMF) turnings by using dynamical networks. We map network information on to a regular grid in magnetic local time and magnetic latitude (MLT and Mlat) and aggregate over several hundred events. We find that regions that experience large increases in correlation post-turning coincide with typical locations of a two cell convection system and are influenced by the IMF By. Our method determines the time between the turnings reaching the magnetopause and a network response to be 8-10 minutes.

.

Chapter 1

Introduction

1.1 Introduction - The Solar Wind, the Magnetosphere and the Ionosphere

Space weather is the result of the interaction between Earth's near Earth plasma environment and the solar wind plasma. Space weather manifests as perturbations in the Earth's magnetic field and plasma content over a range of spatial and temporal timescales. Such perturbations can have significant consequences for an increasingly technological society , with satellites in orbit around Earth being particularly susceptible [Baker et al., 2004]. It is therefore essential to understand the physical processes that underpin space weather. In this thesis we apply dynamical network analysis in an attempt to quantitatively characterise isolated substorms and the magnetospheric convection system.

In this chapter we outline the plasma physics that underpins the dynamics of the systems. To fully describe the important physics on all scales it is essential to consider both a single particle and magnetohydrodynamics

(Magnetohydrodyanmics (MHD)) framework for plasmas. We describe important large scale dynamical processes that occur in the magnetosphere, the convection of the magnetic field towards tail and their subsequent storage and release in the form of magnetic substorm events. We also briefly outline the basics of networks and its terminology.

1.2 The Physics of Magnetised Plasmas

Charged particles experience a force when in the presence of electric and magnetic fields. The forces acting on a charged particle i are described by the Lorentz equation,

$$m_i \ddot{\mathbf{r}}_\mathbf{i} = q_i(\mathbf{E}(\mathbf{r_i}, t) + \dot{\mathbf{r}}_\mathbf{i} \times \mathbf{B}(\mathbf{r_i}, t)), \tag{1.1}$$

where m_i is the mass and q_i the charge of a charged particle i, $E(\mathbf{r}, t)$ the background electric field, $\mathbf{B}$ the background magnetic field and $\mathbf{r}$ the position vector. Together with Maxwell's equations,

$$\nabla \times \mathbf{B} = \mu_0 \mathbf{j}(\mathbf{r}, t) + \frac{1}{c^2}\frac{d\mathbf{E}}{dt} \tag{1.2}$$

$$\nabla \cdot \mathbf{B} = 0, \tag{1.3}$$

$$\nabla \times \mathbf{E} = -\frac{d\mathbf{B}}{dt} \tag{1.4}$$

$$\nabla \cdot \mathbf{E} = \frac{\rho(\mathbf{r}, t)}{\epsilon_0}, \tag{1.5}$$

where ρ and $\mathbf{j}$ are the charge density and current density respectively, they form the governing equations for classical electrodynamics. In a plasma there

are N charged particles, hence, the charge density and current density are

$$\rho(\mathbf{r}, t) = \sum_{i}^{N} q_i \delta(\mathbf{r} - \mathbf{r_i}(t)) \tag{1.6}$$

and

$$\mathbf{j}(\mathbf{r}, t) = \sum_{i}^{N} q_i \dot{\mathbf{r}}_\mathbf{i}(t) \delta(\mathbf{r} - \mathbf{r_i}(t)) \tag{1.7}$$

respectively, where δ is the Dirac delta distribution. Solutions to the group of equations 1.1 to 1.7 is not possible with a general form for E and B. However, solutions to the equations for individual charged particles motion is possible.

1.2.1 Single Particle Dynamics

Many important features and current systems in the magnetosphere, such as the ring currents (section 1.3.2), can be explained by considering the dynamics of single particles. The majority of derivations in this section follows those found in Boyd and Sanderson [1969]. Given the absence of an electric field and constant magnetic field pointing in the z direction the solutions to equation 1.1 are trivial. The charged particles have a constant guiding centre motion, $\frac{dv_{gc}}{dt} = 0$, and gyration about the z axis,

$$x = \frac{v_\perp}{\Omega} cos(\Omega t + \phi) + x_0 \tag{1.8}$$

and

$$y = \frac{v_\perp}{\Omega} cos(\Omega t + \phi) + y_0. \tag{1.9}$$

Where $\Omega = \frac{qB}{m}$ is the gyro-frequency, ϕ is the phase determined by the initial conditions, x_0, y_0 the initial positions and $v_\perp = \sqrt{\dot{x}^2 + \dot{y}^2}$. Positive and

negative particles gyrate in opposite directions.

In the context of the Earth's magnetosphere, the magnetic field is not spatially uniform but varies as a function of distance from the Earth. As well as this, the field is curved and the system itself is dynamic ($B = B(t)$) due to variable external forcing by the solar wind. There are also additional forces present, namely gravity and external imposed electric fields. The particle trajectories can be solved for these conditions given that the length scale L_B associated with the spatial variations of B, $\nabla B(\mathbf{r}) \sim \frac{B}{L_B}$, is $L_B \gg r_l$ (typical gyro-radius for 1 keV electrons is $r_l \sim$1.5km [Williams, 1985]). That is, simple solutions are possible as long as the field does not vary significantly over a gyration. The case is similar for the temporal variations $t_B \gg \frac{1}{\Omega}$ (typical gyro-period of a 1 keV electron is $\frac{1}{\Omega} \sim 7.5 \times 10^{-5}$s) where t_B represents the characteristic temporal variation timescale. Second order temporal and spatial variations terms are then considered small enough to ignore.

The spatial inhomogeneities, temporal inhomogeneities, and external forces introduce drift velocities in addition to the gyro and guiding centre velocities. In general, a drift v_d due to an arbitrary force F is given by

$$v_d = \frac{(\mathbf{F} \times \mathbf{B})}{qB^2}. \tag{1.10}$$

The drift velocity v_d is perpendicular to both $\mathbf{F}$ and $\mathbf{B}$. The forces due to gradients and curvatures in the magnetic field, F_g and F_c respectively, can be shown to be

$$\mathbf{F_g} = \mu \cdot \nabla B \tag{1.11}$$

and

$$\mathbf{F_c} = \frac{mv_{\parallel}^2 \hat{\mathbf{n}}}{R_c} \tag{1.12}$$

where $\hat{\mathbf{n}}$ is the unit vector which is perpendicular to $\mathbf{B}$ and points away from the centre of curvature and the magnetic moment is

$$\mu = \frac{\frac{1}{2}mv_{\perp}^2}{B}\hat{\mathbf{b}}. \tag{1.13}$$

The $\hat{\mathbf{b}}$ unit vector points in the direction of $\mathbf{B}$. The direction drifts produced by these forces are dependent on the sign of the charged particles, consequently currents are produced by these drifts.

Drifts can also occur due to a background electric field that has a component perpendicular to the magnetic field,

$$v_e = \frac{\mathbf{E} \times \mathbf{B}}{B^2}. \tag{1.14}$$

Note that this drift does not have a dependence on the sign of the charged particle and will not produce currents for a neutral plasma.

Adiabatic Invariants

Adiabatic invariants are quantities that are constants of motion under the condition that the magnetic field varies slowly with respect to the gyro-radius and gyro-periods of the charged particles. The magnetic moment of a gyrating charged particle is an adiabatic invariant. By considering an axially symmetric $\frac{dB}{d\phi} \neq 0$) in cylindrical polar coordinates equation 1.3 is

$$\nabla \cdot \mathbf{B} = \frac{1}{r}\frac{d}{dr}(rB_r) + \frac{dB_z}{dz}. \tag{1.15}$$

Which when integrated over a Lamor orbit, assuming $\frac{dB_z}{dz}$ is approximately constant over the orbit, gives

$$B_r \simeq -\frac{r_l}{2}\frac{dB_z}{dz} \tag{1.16}$$

and since B_r is small,

$$B_r \simeq -\frac{r_l}{2}\frac{dB_z}{dz} \simeq -\frac{r_l}{2}\frac{dB}{dz}. \tag{1.17}$$

The dot product of the parallel component of the velocity with equation 1.1 can be expressed as

$$\frac{d\frac{1}{2}v_\parallel^2}{dt} = -\mu v_\parallel \frac{\delta B}{\delta z} = -\mu \frac{dB}{dt}, \tag{1.18}$$

since B only depends implicitly on time ($B = B(\mathbf{r}(t))$). By multiplying equation 1.13 by B, differentiating with respect to time, adding to equation 1.18 and using energy conservation the following is obtained,

$$\frac{d\mu B}{dt} - \mu\frac{dB}{dt} = 0. \tag{1.19}$$

Then

$$\frac{d\mu}{dt} = 0, \tag{1.20}$$

and the magnetic moment is invariant under slow changing B fields.

Figure 1.1(a) shows a magnetic mirror field configuration. The adiabatic invariance of μ is of importance in such a field configuration. As a charged particle moves from a weak field region to a strong field region, both μ and the total energy must remain constant. As a consequence $v_\parallel$ must decrease (since $v_\perp$ must increase). If $v_\parallel = 0$ then the particle cannot move further into the

stronger field region and is reflected. Whether a particle is reflected depends on its pitch angle

$$\tan\theta = \frac{v_\perp}{v_\parallel} \tag{1.21}$$

and the strength of the mid points B_0 relative to B_m, $R = B_m/B_0$, where R is the mirror ratio. The particles are reflected if

$$sin(\theta_0) \geq R^{-\frac{1}{2}} \tag{1.22}$$

where θ_0 is the pitch angle of the particle at the midpoint.

The Earth's magnetic field is an example of a naturally occurring magnetic mirror trap, figure 1.1 (b). Charged particles are trapped in oscillating motion between the north and south poles where the field is strongest, with periods on the order of seconds [Williams, 1985]. Particles remained trapped unless they undergo pitch angle scattering which occurs when the assumption for adiabatic invariance are violated. Pitch angle scattering occurs via two main mechanisms, coulomb collisions with atmospheric constituents and resonant scattering by plasma waves [Abel and Thorne, 1998].

Another adiabatic invariant is the longitudinal invariant,

$$J = \oint v_\parallel ds, \tag{1.23}$$

where ds is an element of the guiding centre path. The integral is evaluated over one complete transit between mirror points. This is a conserved quantity as long as the timescale of variation of B is much longer than the the transit time between mirror points.

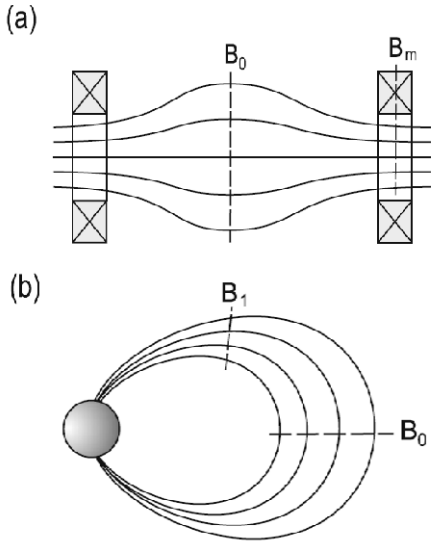

Figure 1.1: (a) shows a basic magnetic mirror configuration. (b) the Earth's magnetic field configuration. Reproduced from [Piel and Brown, 2011]

1.2.2 The Fluid Model of Plasmas - Magnetohydrodynamics

The solutions to equations 1.1 to 1.7 for a large collection of interacting charged particles are not possible without a set of simplifying assumptions. Magnetohydrodynamics attempts to do this by applying a fluid approach to plasmas. A plasma is an electrically neutral fluid consisting of positive and negative particles. Unlike regular fluids where particles interact through direct collisions, plasma particles interact through the longer range electromagnetic force thereby exhibit collective effects. Each charged particles interacts simultaneously with a large number of other charged particles. For this to occur the number of charges within a Debye sphere (the sphere of influence of a charged

particle) $N_D = 4\pi n\lambda_D^3/3 \gg 1$, where λ_D is the Debye length given by,

$$\lambda_D = \left(\frac{\epsilon_0 kT}{ne^2}\right)^{-\frac{1}{2}}. \tag{1.24}$$

The Debye length is independent of any applied magnetic field, hence, is a characteristic length scale of unmagnetised plasma. In addition, if the Debye length is much shorter than the physical size of the plasma the plasma is quasi-neutral. Figure 1.2 shows typical plasma parameters for a variety of real world plasmas. The magnetosphere and most of the ionosphere comfortably satisfy the quasi-neutrality condition. The neutrality condition implies that $\nabla \cdot \mathbf{E} = 0$ and $\nabla \cdot \mathbf{j} = 0$. Unmagnetised plasmas also have a characteristic frequency known as the plasma frequency,

$$\omega_{pe} = \sqrt{\frac{n_e e^2}{m_e \epsilon_0}}, \tag{1.25}$$

where n_e is the number density of electrons, m_e is the mass an electron and ϵ_0 the permittivity of free. The frequency is associated with the Coulomb restoring force if one were to displace a number of electrons within the quasi-neutral plasma. In deriving this the mass of the electron is considered insignificant compared with the mass of ions. If the plasma frequency is large compared to the collision frequency, then the electromagnetic interactions dominate.

The governing equations for MHD combine Maxwell's equations and the fluid equations, and can be applied under the following assumptions. The characteristic speed of the plasma is much less than the speed of light. The characteristic timescales of variations of plasma properties is much longer than the gyro and plasma frequency period. The collision period and mean free path

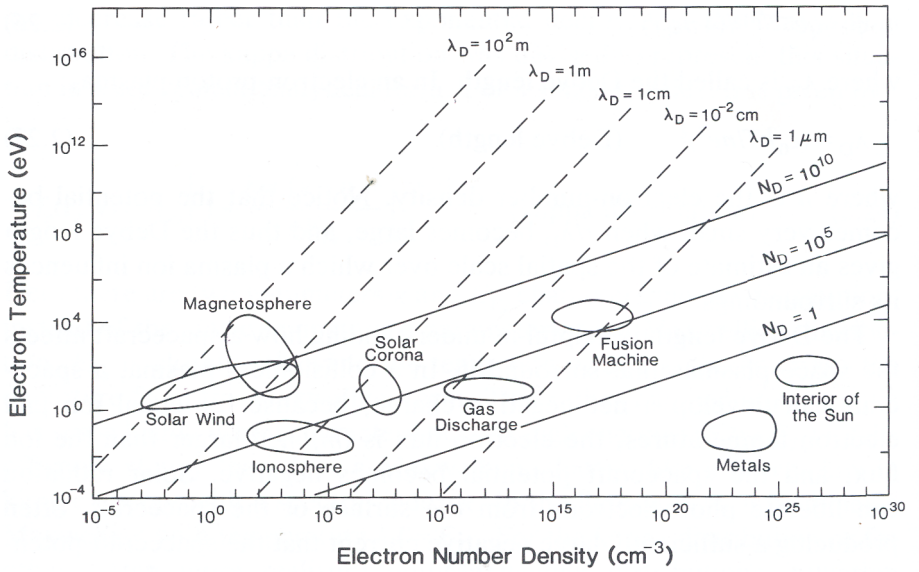

Figure 1.2: The electron temperature and number density ranges of various plasmas. Also plotted are the number of particles in a Debye sphere and the the Debye length. Reproduced from [Kivelson and Russel, 1995]

are much less than the characteristic time and spatial scales of variation. And that the plasma is neutral, $n_e = n_i$ (for singularly ionised ions).

In ideal MHD the resistivity of the plasma, η, is assumed to be low enough to ignore. This is generally a property of collisionless plasma such as those found in the majority of the magnetosphere. This has consequence of magnetic field lines are "frozen" into the plasma. This condition fixes the topology of the field configuration. The mass continuity equation,

$$\frac{d\rho}{dt} + \nabla \cdot (\rho \mathbf{u}) = 0 \tag{1.26}$$

where $\mathbf{u}$ is the velocity of the fluid and it is assumed that there are no sources or sinks. The momentum equations is simply momentum equation for fluids

with the addition of a force term due to the Lorenz force,

$$m(\frac{d\mathbf{u}}{dt} + \mathbf{u} \cdot \nabla \mathbf{u}) = -\nabla P + \mathbf{J} \times \mathbf{B}. \tag{1.27}$$

Where the $\mathbf{J} \times \mathbf{B}$ term originates by considering the Lorentz force combined for both positive and negative species. The Maxwell equations 1.3 and 1.4 remain unchanged, however, equation 1.2 becomes

$$\nabla \times \mathbf{B} = \mu_0 \mathbf{j}(\mathbf{r}, t), \tag{1.28}$$

that is the displacement current term is considered small enough to ignore. This is satisfied if the characteristic velocity of the plasma is much less than the speed of light. Ohm's law is,

$$\eta \mathbf{j} = \mathbf{E} + \mathbf{u} \times \mathbf{B}. \tag{1.29}$$

By substituting for $\mathbf{E}$ in equation 1.4 (and using equation 1.2), the following form for the induction equation can be obtained,

$$\frac{d\mathbf{B}}{dt} = \eta \nabla^2 \mathbf{B} + \nabla \times (\mathbf{u} \times \mathbf{B}) \tag{1.30}$$

If either the length scale of variation is large or η is very small (as is the case in the magnetosphere) then the diffusion term (first term on the right) can be neglected. This results in the frozen in condition. Plasma elements are now tied to the field lines and plasma and field move together. The very low

resistivity also implies that ohms law now is,

$$\mathbf{E} = -\mathbf{u} \times \mathbf{B}. \tag{1.31}$$

The adiabatic energy equation is,

$$\frac{Dp\rho^{-\gamma}}{Dt} = 0 \tag{1.32}$$

where γ is the ratio of specific heats. These equations provide a single fluid description of a plasma.

There are three main modes of waves can exist in this framework, pure Alfven and fast and slow compressional. Alfven waves are supported solely by bends in the magnetic field where the restoring force is magnetic tension, analogous to waves on a string. Fast compressional waves involve perturbations of the magnetic and gas pressure. For fast waves these perturbations are in phase. Slow waves involved the same compressional perturbation but with the magnetic and gas pressure perturbion, however, they are out of phase. The propagation velocities of the waves obeys the following, $v_F \geq v_A \geq v_S$, where v_F, v_A and v_S are the fast, Alfven, and slow wave velocities respectively. Plasma waves are important in the context of the magnetosphere because they can affect the the pitch angle of particles trapped in the Earth's mirror configuration (see section 1.2.1) via resonant wave particle interactions.

1.3 The Solar Wind, The Magnetosphere, the Ionosphere and Space Weather

In isolation, the Earth's magnetic field would be close to dipolar. The presence of the solar wind distorts the shape of the magnetosphere and is the supplier of energy for the majority of its internal dynamics. That is, the solar wind provides the energy for space weather. The coordinate system we use in the following sections is the Geocentric Solar Magnetospheric (GSM) system. In this coordinate system the x-axis points outwards along the Earth-Sun line and the z-axis is the projection of the magnetic dipole axis on to the plane perpendicular to the x-axis. This coordinate system is ideal for investigating driving phenomena at the front of the magnetosphere, an important concept in the generation of space weather [Russell, 1971].

In the following section we outline the fundamental concepts underpinning the magnetosphere and its interaction with the solar wind, the ionosphere and its coupling to the magnetosphere and space weather.

1.3.1 The Solar Wind

The Sun is the primary source of energy and the driver of dynamics in the solar system. Along with electromagnetic radiation, the Sun also emits a constant stream of plasma, discovered through observations of comet tails [Biermann, 1951]. In addition, the Sun has a magnetic field, which is generated through the dynamo effect as a result of convection within the Sun's interior [Gough and McIntyre, 1998]. The Sun undergoes a cycle of field reversal with a half period of 11 years and is accompanied by variations in solar activity

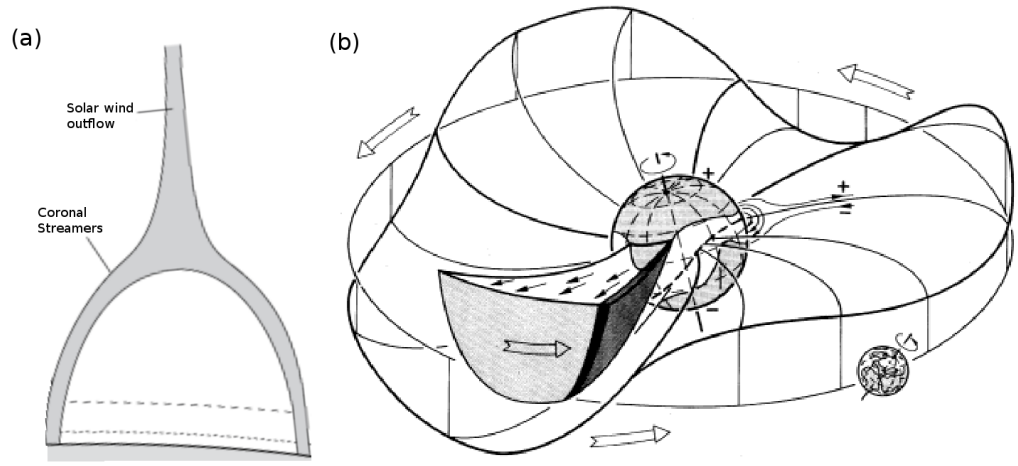

Figure 1.3: (a) A cartoon model of a coronal streamer. (b) Shows the boundary between opposite magnetic polarities (the magnetic neutral line). The magnetic field forms a spiral due to the rotation of the Sun. Reproduced from [Aschwanden, 2006]

(number of sunspots) [Hale, 1908]. During the Sun's active periods there are a larger number of sunspots as well as increased flare and coronal mass ejection frequency. Consequentially, these periods are also associated with elevated levels of space weather activity on Earth.

In general the wind can be split into two categories, slow and fast. Typical speeds of the slow and fast solar wind are $\sim 400 kms^{-1}$ and $\sim 750 kms^{-1}$ respectively. The two categories of solar wind have different physical origins. The fast wind originates from coronal holes (regions of open flux) usually found at high latitudes, except during periods of high activity. The composition of the fast wind is of photospheric origin. The slow wind originates from coronal streamers, structures that have both closed and open field lines, figure 1.3(a).

The resistance of the solar wind plasma is very low, as a consequence the frozen in condition applies. The wind flows radially outward and carriers the frozen in field with it. As a result the rotation of the Sun causes field lines to be drawn out into a Parker spiral [Parker, 1958]. In addition, there exists

a neutral line (or boundary layer) between the north and south polarities, the latitudinal position which is not static. As a result, the topology of the solar wind has a ballerina skirt appearance, figure 1.3(b), this has consequences for the statistical properties of the magnetic field at the Earth's magnetopause. Parker also showed that by the time the solar wind reaches Earth the velocity is above that of the Alfven speed [Parker, 1958].

While figure 1.3(b) highlights the large scale variations of the solar wind, in reality the solar wind also contains variations in magnetic field, density and velocity on many spatial scales [Goldstein and Roberts, 1999]. In addition, solar events, such as coronal mass ejections, introduce highly structured embedded magnetic fields that deviates significantly from the ambient wind. Such events are a major factor in the interactions between the Earth's magnetosphere and the solar wind.

In the Earth's rest frame the solar wind has an electric field given by

$$\mathbf{E} = -\mathbf{u_{sw}} \times \mathbf{B_{sw}}, \tag{1.33}$$

where $\mathbf{u_{sw}}$ and $\mathbf{B_{sw}}$ are the bulk solar wind velocity and solar wind magnetic field respectively. A varying amount of the potential is felt within the magnetosphere depending on the coupling between the solar wind and the magnetosphere.

1.3.2 The Magnetosphere

Figure 1.4 shows a basic view of Earth's magnetosphere. In isolation the Earth's magnetic field would be close to dipolar. The presence of the solar wind causes changes in this topology. The solar wind, which consists of a

fast moving stream of mostly protons and electrons, impinges on the magnetosphere from the left, as shown in figure 1.4. The supersonic solar wind undergoes a bow shock as it encounters the magnetosphere. The magnetosheath is the region of shocked sub-sonic solar wind. The magnetosphere acts as an effective barrier to the solar wind, which causes the magnetic field to be compressed on the dayside [Kivelson and Russel, 1995]. The majority of the solar wind is diverted around the magnetosphere. The flow of the solar wind around the magnetosphere causes a stretching of the nightside dipole field into a tail like structure via tangential stress. The tangential stress manifests through the diffusion of particles from the shocked wind into the magnetosphere via several non-MHD processes including reconnection [Kivelson and Russel, 1995]. By construction, the topological deviations from a dipole magnetic field configuration necessitate the existence of additional currents within the magnetosphere. There are four main current systems in the outer-magnetosphere: the magnetopause currents, the tail current, the ring current and the field aligned currents (FAC), all of which will be discussed later.

Outer Magnetosphere

The outer magnetosphere is distinct from the inner magnetosphere which is characterised by the dominant co-rotation of the plasma sphere with the Earth [Nishida, 1966]. The outer magnetosphere is almost a true magnetic cavity, with a low density of plasma in comparison to the solar wind and inner plasmasphere. The magnetopause is the boundary that separates the geomagnetic field and plasma that is considered terrestrial from the solar wind plasma. The boundary was first proposed by Chapman and Ferraro [1931], who considered the solar wind intermittent and hence the boundary intermittent. The

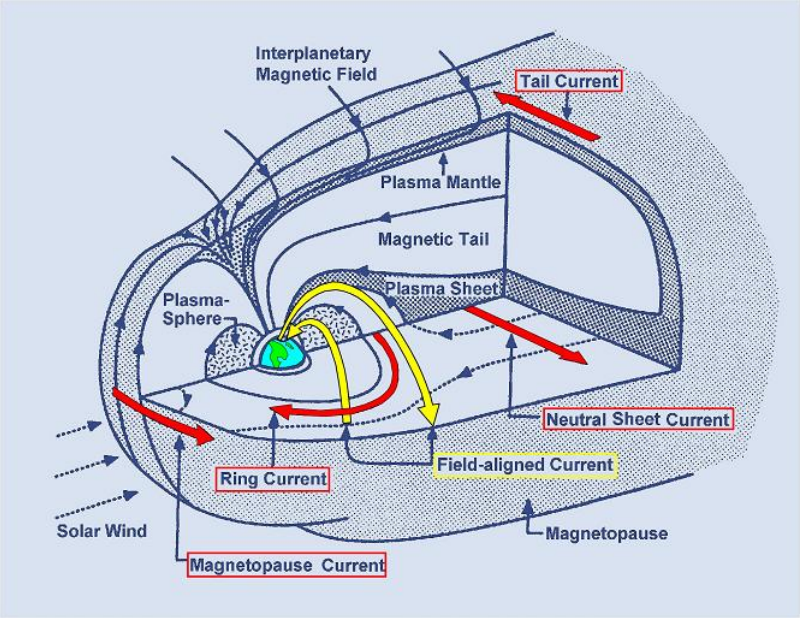

Figure 1.4: A basic view of the magnetosphere with the important regions and current systems labelled. Reproduced from [Kivelson and Russel, 1995]

solar wind was later shown to be a constant feature. Dungey [1955] predicted the magnetopause was likely to be a permanent boundary. The stand-off distance of the magnetopause, in a first order approximation, is determined by the balance between the solar wind ram pressure and the magnetic pressure of Earth's inherent magnetic field (under the assumption that the magnetosphere's thermal plasma pressure is insignificant compared to the magnetic pressure),

$$\rho_{sw} u_{sw}^2 = \frac{B_{MS}^2}{2\mu_0}, \tag{1.34}$$

where the ρ_{sw} is the solar wind density. The shape of the magnetopause boundary can vary, becoming flatter in the presence of southward IMF ($B_z < 0$) and more curved otherwise [Sibeck et al., 1991]. The polar cusps, shown in figure 1.5, are regions in which the solar wind can enter the magnetosphere. It is the region that separates the field lines that form the dayside magnetosphere

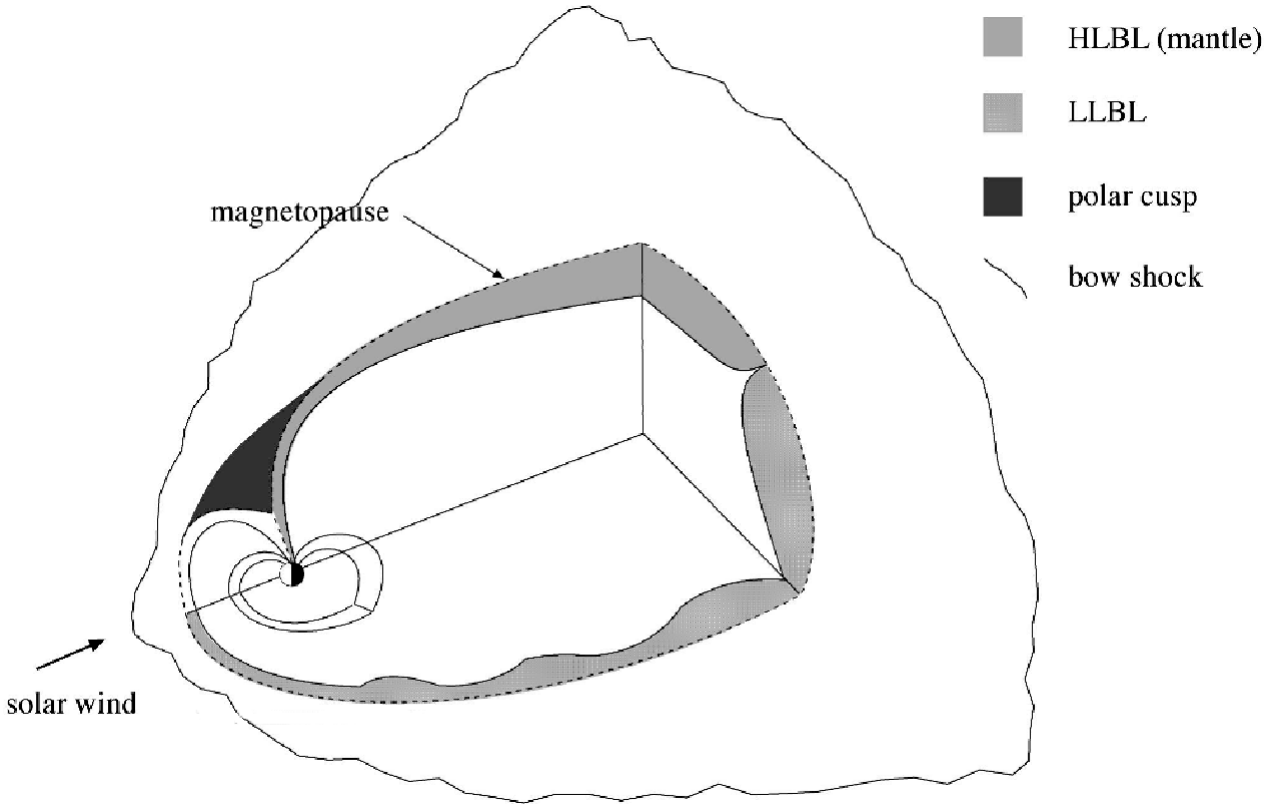

Figure 1.5: Shows the polar cusps regions highlighted in black. Reproduced from [Koskinen, 2011]

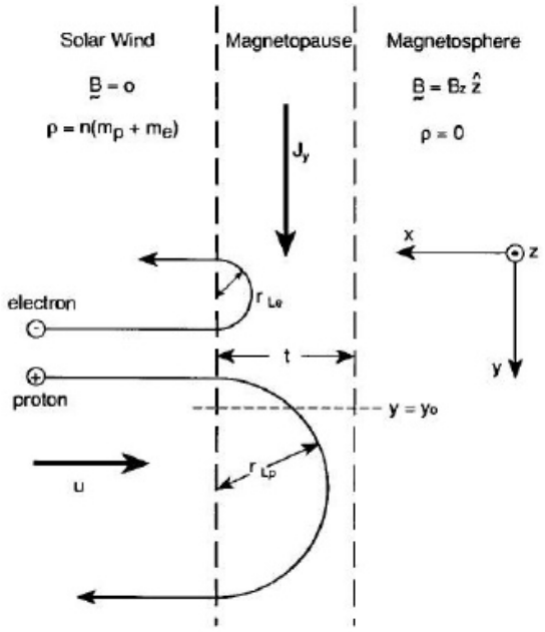

Figure 1.6: The magnetopause boundary between the the solar wind and the magnetosphere. Ions and electrons cross the boundary undergo a half gyro-orbit and re-enter the magnetosheath solar wind. Reproduced from [Koskinen, 2011]

and those that form the nightside magnetotail.

The magnetopause is closed (sometimes) and, like other magnetised plasma boundaries, carries a sheet of current. The magnetopause currents close with the currents in the tail. In a simplified particle viewpoint, the magnetopause currents (Chapman-Ferraro currents) arise from the half gyro-orbits of the protons and electrons of the solar wind. As the particles cross the magnetopause boundary the protons and electrons feel the much stronger magnetic field within the magnetosphere and under half gyro-orbits before leaving the magnetopause. The summation of the paths of the ion half gyro-orbits, shown in figure 1.6, provide the majority of the current is from the ions since they have a larger Larmor radius, hence, move a greater total distance. The magnetopause currents close with the magnetotail currents. The magnetotail consists

of a north and south lobe that contain oppositely directed magnetic flux, with the north lobe's field directed towards Earth. As a consequence, there is a magnetic neutral point at the boundary between the lobes. The magnetotial can stretch as far as $\sim 100R_E$ anti-sunward. The configuration in the tail is like that of a Harris sheet [Harris, 1962], as such there is a current sheet at the boundary consisting of comparatively dense plasma that maintains the total pressure balance across the lobes. The currents in the magnetail close around the lobes and with the dayside magnetopause currents. The amount of magnetic flux in the lobes is dynamic; reconnection at the magnetopause will transport flux anti-sunward into the tail. Similarly, reconnection in the tail will transport flux from the tail to the dayside. Such processes are known as magnetospheric convection which is discussed in section 1.4.

The Inner Magnetosphere

Moving towards the Earth from the outer magnetotail, where the configuration is Harris sheet like, the field becomes more dipolar. The plasma sheet boundary layer is the transition region between the near empty tail lobes and the dense plasma sheet and is shown in figure 1.7. Where this region is located is strongly dependent on the levels of forcing by the solar wind, along with internal processes, but is usually found at $\sim 6.6R_E$ [Eastman et al., 1984]. During high levels of activity, when the cross-tail current is intensified and the plasma sheet boundary layer (Plasma Sheet Boundary Layer (PSBL)) can be found closer to Earth. Inside the PSBL the cross-tail currents become the ring current that encircles the Earth in the East to West direction. The ring current has a net westward current and arises from the particle drifts due to curvature and gradients in the Earth's dipole magnetic field [Chapman and

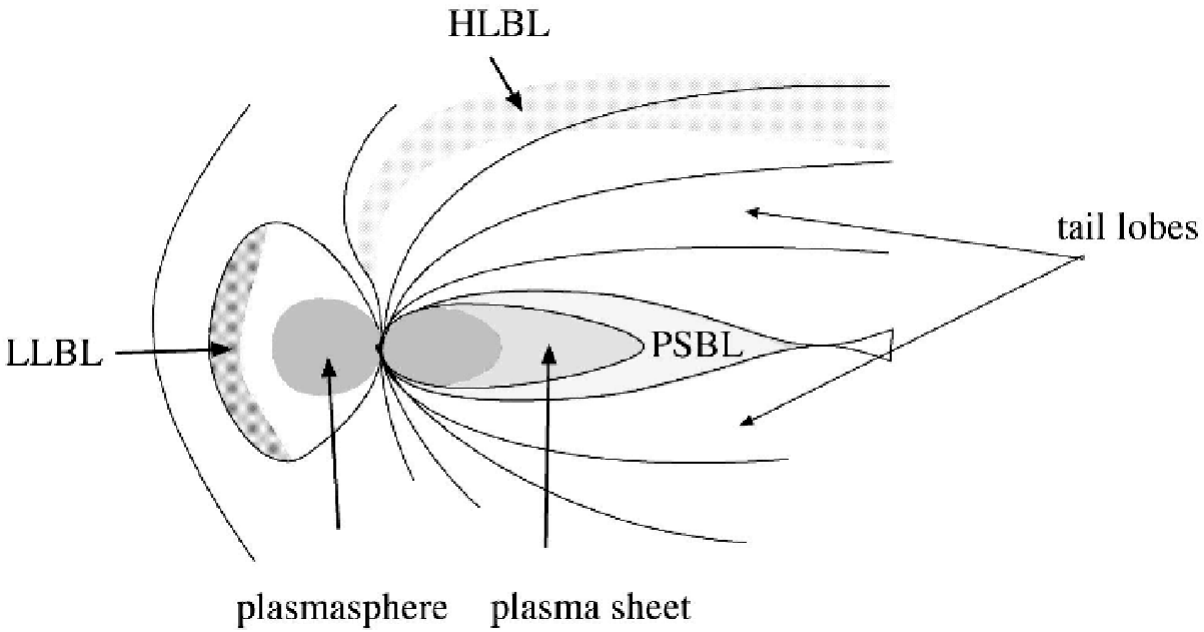

Figure 1.7: Labels some key plasma regions of magnetosphere. The plasma sheet boundary layer (PSBL), the low latitude boundary layer (LLBL) and the high latitude boundary layer (HLBL) as well as the plasmasphere and plasma sheet are labelled. Reproduced from [Koskinen, 2011]

Ferraro, 1941] (see section 1.2.1). The majority of the ring current is carried by protons of energies in the 10 to 200 keV range.

Closer to Earth there is the plasmasphere, shown in figure 1.7. The ring current and the plasmasphere are not distinct, that is, the charged particles in the plasmasphere plasma support the ring current. The westward currents are a result of the drift motion of ions and electrons, where the drifts are due to the gradients and curvature of the Earth's field. The plasma in this region are trapped in the Earth's magnetic mirror configuration outlined earlier in section 1.2.1.

Co-located with the ring current and plasmasphere are the Van Allen radiation belts [Allen, 1958], the belts, with the respective proton and electron

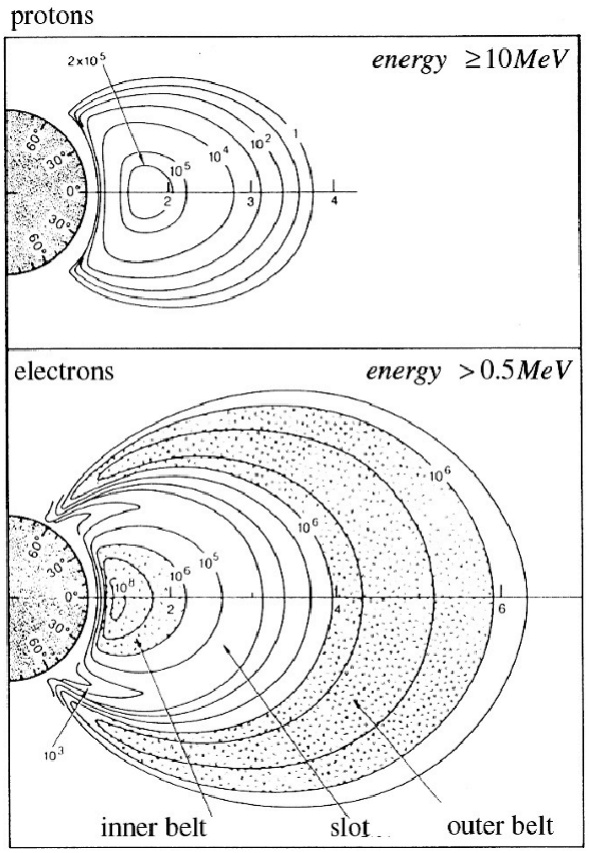

Figure 1.8: The proton and electron fluxes in different regions of the magnetosphere. The electron flux has a drop-out in the slot regions between the inner and outer belts. Kivelson and Russel [1995]

fluxes, are shown in figure 1.8. The belts contain a population of high energy particles. The inner Van Allen belt ($L \sim 1.5$-3) are dominated by high energy protons of energies ($\sim$ MeV) with a significant electron population. The outer belts ($L > 4$) are dominated by high energy electrons in the keV to MeV range. The high energy proton flux falls off gradually for larger L shell values, whereas there is a conspicuous lack of high energy electrons in the slot region shown in figure 1.8, which changes during large scale magnetospheric activity. L shells defines a set of field lines, L=2 defines the magnetic fields lines intersecting a circle in the equatorial plane of radius 2 R_E.

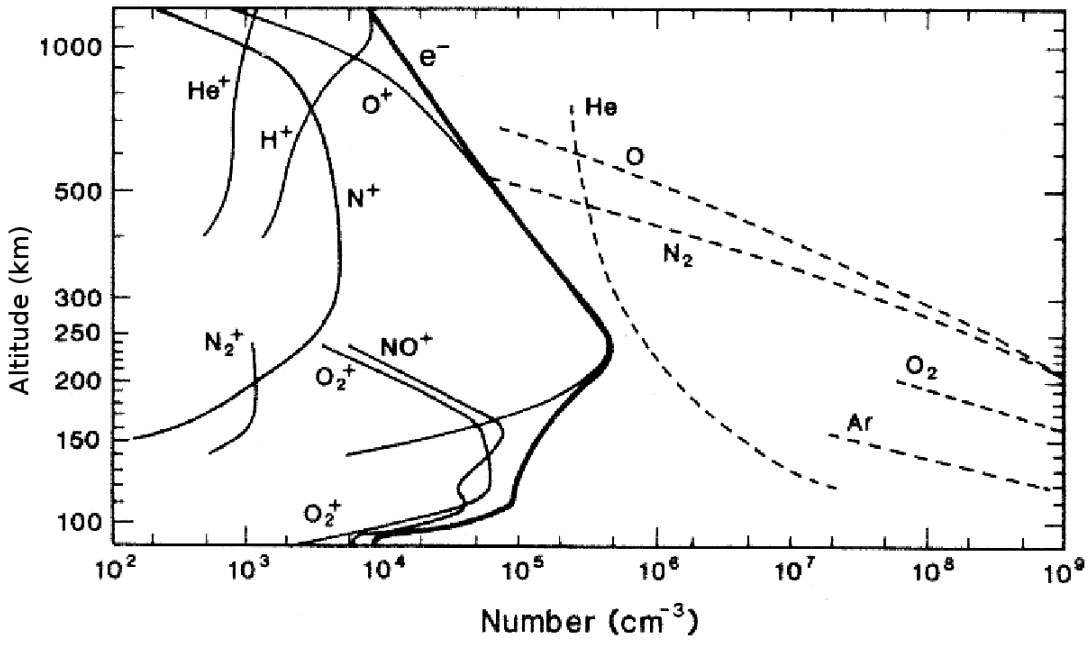

Figure 1.9: The number densities of different species of molecular and atomic ions and non-ions as a function of altitude. Reproduced from Johnson [1969]

1.3.3 The ionosphere

In this section we primarily summarise the properties of the high latitude ionosphere. The ionosphere is the upper region of the Earth's atmosphere. Figures 1.9 and 1.10 show that the plasma does not exhibit a simple relation between height and ionisation. The ionosphere is typically split into a few main layers, the E, D and F layers, where there are local maxima in the conductivity.

Figure 1.10 shows the average conductivity as a function of height. The D layer occurs at an altitude of 60-90km; the main source of ionisation in this region is from solar radiation ionising molecules. Despite the high number of neutral particles, the D region can still be treated as a plasma, albeit one with strong coupling to the neutral winds due to collisions. The E layer

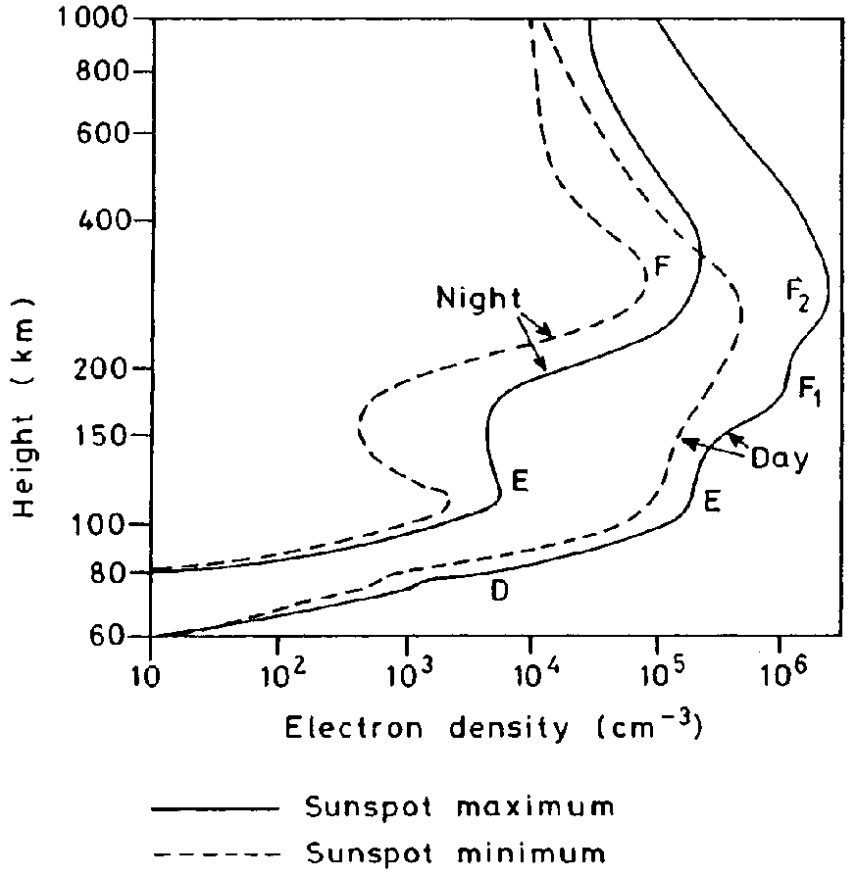

Figure 1.10: The average conductivity of the ionosphere as a function of height. Both dayside and nightside conductivities are shown (labelled) during solar maximum (solid) and solar minimum (dashed). The respective ionosphere layers, E, D, F_1 and F_2 are labelled and correspond to local maximums in the conductivity. Reproduced from Hargreaves [1992]

occurs at an altitude of around 90-150km - the ionisation in this region occurs from precipitating electrons travelling along field lines from the magnetosphere. Recombination rates are high in both of these regions. Because of very quick recombination as any light given of by recombination can be used as a proxy measure for the number of ionised particles in a given spatial region at that particular time. Figure 1.10 shows that above 150km are the F layers. In the dayside the layers can be split into two, the F_1 layer is between 150-220km, it is ionised by extreme ultraviolet (Extreme Ultra Violet (EUV)) radiation from the Sun and is composed of a mixture of molecular ions and atomic oxygen ions. The F_2 region occupies the region above the F_1 layer and consists mostly of ionised atoms. Unlike the E and D regions, above $\sim$ 200km recombination is slow, operating on hour-long timescales [Kivelson and Russel, 1995].

In the magnetosphere the plasma resistivity is assumed to be effectively zero. However, in the ionosphere the plasma is collisional, hence it has finite resistivity. Due to the Earth's background magnetic field the conductivity is not isotropic [Baker and Martyn, 1953]. Because of this there are three currents types: Birkeland currents which flow parallel to magnetic field lines, Pedersen currents which flow in the direction of an applied electric field, $E_\perp$ (which is perpendicular to the magnetic field) and Hall currents which flow in the $E_\perp \times B$ drift direction. Each of the respective directions has a conductivity associated with it, hence a conductivity tensor can be formed and the current can be expressed as,

$$\mathbf{j} = \begin{pmatrix} \sigma_P & \sigma_H & 0 \\ -\sigma_H & \sigma_P & 0 \\ 0 & 0 & \sigma_\parallel \end{pmatrix} \cdot \mathbf{E}, \tag{1.35}$$

where σ_P, σ_H and $\sigma_\parallel$ are the Pedersen, Hall and parallel conductivities re-

spectively. The specific forms of σ_P, σ_H and $\sigma_\parallel$ can be found in Baker and Martyn [1953]. Pedersen currents arise simply from the acceleration of ions and electrons by $E_\perp$. The Hall currents arise from $E \times B$ drifts outlined in equation 1.14, since the drifts do not depend on the charge, it does not inherently produce a current. The different collisional frequencies of the ions and electrons provide the asymmetry that causes current to flow. In the E layer, ions rarely complete a gyro-orbit before a collision and as such they are the primary contributors to the Pedersen currents. Electrons do complete gyro-orbits before collisions, hence they are the main contributors to the Hall currents.

The ionisation and recombination of ions in the ionosphere produces light in the visible and EUV spectrum. These processes are responsible for the Aurora Borealis [Hewson, 1937]. Figure 1.11 show an image taken from the POLAR satellite of the auroral oval in the northern hemisphere. The upper edge of the auroral oval in the nightside signifies the plasma sheet boundary layer, that is, the transition from closed dipole like magnetic field configuration to that of the "open" Harris sheet tail lobes configuration. Similarly, on the dayside at noon, there is typically a red glow which is associated with the polar cusps (see section 1.3.2), where solar wind plasma can stream directly into the ionosphere. The polar cap is the area enclosed by the auroral oval and in this region a polar wind flows upward into the magnetosphere [Ganguli, 1996]. The magnetosphere and ionospheric plasma are coupled via the magnetic field lines that thread both plasmas. The coupling is mediated by field aligned currents. Figure 1.12 shows a statistical distribution of FAC in the ionosphere, determined by Iijima and Potemra [1976] during weakly disturbed periods. The downward field aligned currents are carried by the abundant ionospheric

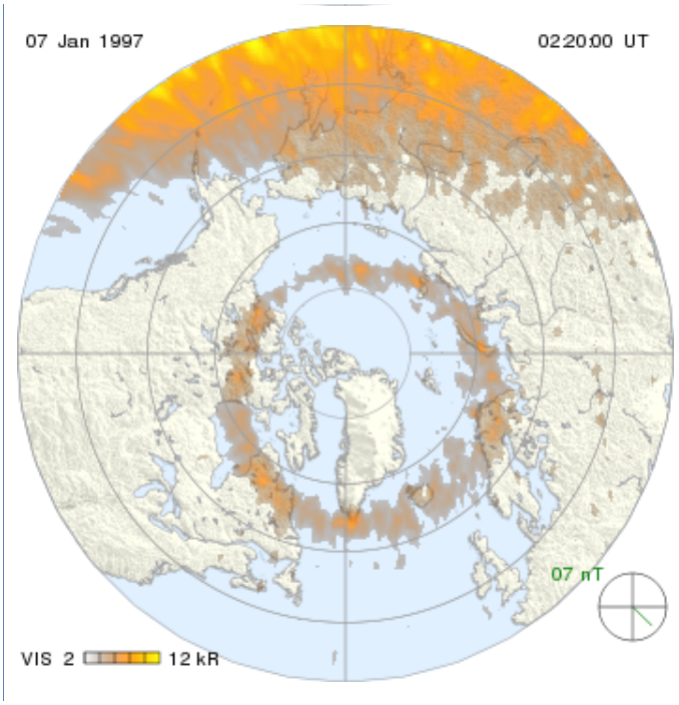

Figure 1.11: The auroral oval in the northern hemisphere as seen from the POLAR satellite in the visible spectrum. Also visible it the visible light due to sunlight. Reproduced from the SuperMAG website (http://supermag.jhuapl.edu/)

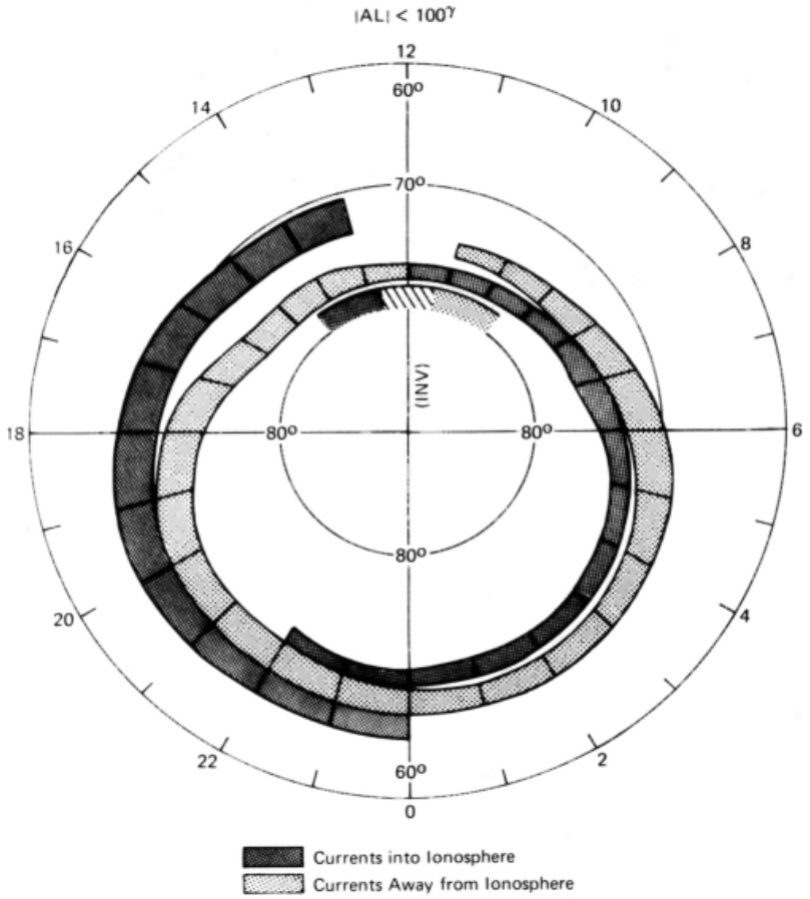

Figure 1.12: The statisitical distrubtion of FAC in the northern hemisphere. Reproduced from Iijima and Potemra [1976]

electrons that react quicker due to their small mass relative to ion. However, upward field aligned currents would require downward flow of electrons from the magnetosphere. Electrons in the plasma sheet are trapped by the Earth's natural magnetic mirror configuration, and as such, there may be insufficient electrons to supply the current. In this situation a temporary and large electric field occurs along field lines. This electric field accelerates the electrons far beyond typical thermal energies in the plasma sheet and is responsible for the brightest of aurora in the nightside [Knight, 1973].

Kivelson and Russel [1995] give an excellent qualitative example of the

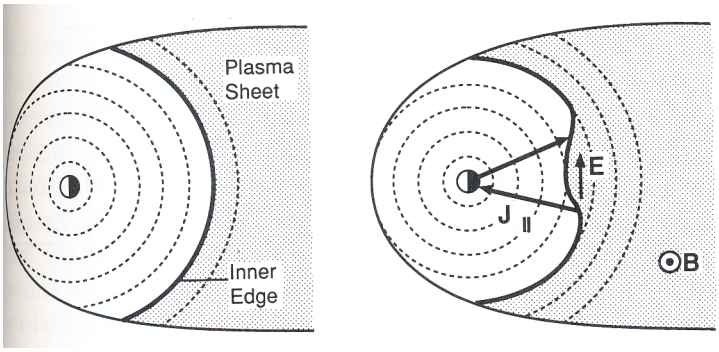

Figure 1.13: Diagram showing how FAC might be generated from a perturbation of the inner edge of the plasma sheet. The view is of equatorial cross-section of the inner magnetosphere as viewed from the north. Reproduced from Kivelson and Russel [1995]

origin of FAC at the plasma sheet boundary layer. Figure 1.13 shows the inner edge of the plasma sheet in equilibrium (left) and in a perturbed configuration on the right. The dashed contours are contours in which the westward ring current flows due to the gradients in the magnetic field. They also denote constant equatorial magnetic field. If the position plasma sheet boundary layer moves additional gradients in the magnetic field are generated. This generates a partial ring current that has to be closed. To close the partial ring current, current is diverted through the ionosphere along field lines completing the circuit. The ionosphere can be considered to act as a resistor in the magnetospheric circuit, dissipating energy [Lyon, 2000]. The reason why the plasma sheet boundary layer deforms revolves around dynamics introduced by the solar wind in the form of magnetospheric convection, which is approached in the following section.

1.4 Magnetospheric Convection

Mangetospheric convection is a central topic in this thesis. It refers to the movement of field lines and plasma within the magnetosphere induced by interaction of the magnetosphere with the solar wind. It is the process that allows the energy of the solar wind to enter the magnetosphere to provide energy for the space weather events observed within the bulk magnetosphere and their resulting effects on Earth.

1.4.1 Basic Convection

Axford [1964] suggested the viscous interaction with the solar wind and an effectively closed magnetosphere was responsible for convection in the magnetosphere. As the solar wind flows past the flanks of the magnetosphere it induces a two cell circulation inside the magnetosphere. Figure 1.14 shows this two cell circulation mapped down to the northern hemisphere ionosphere, as proposed by Axford [1964]. Axford [1964] compared this convection to the convection within a falling rain drop. It is now well known that while the process does occur and does provide some of the required energy it cannot provide it all [Cowley, 1982].

Dungey [1961] suggested that magnetic reconnection at the magnetopause played a key role in the convection within the magnetosphere. Proposed was that during periods of southward IMF (when B_z is negative) the IMF is anti-parallel to the Earth's magnetic field at the magnetopause. In this configuration, a thin current sheet layer exists at the magnetopause, whose length scale is much smaller such that the diffusion term in equation 1.30 become significant. Because of this the frozen in condition (that exists both

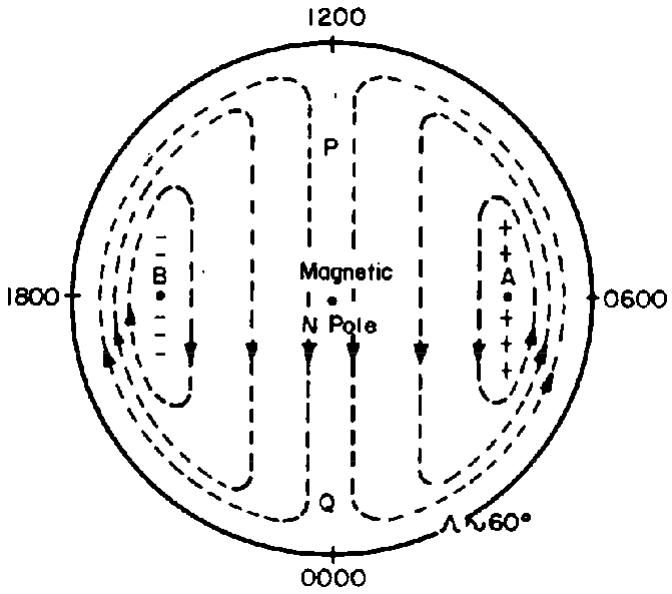

Figure 1.14: A simplified view of the ionospheric flows lines resulting from viscous interaction of the solar wind and the magnetosphere during northward IMF. A similar but stronger convection pattern occurs during periods of southward IMF. Labelled on the figure is the magnetic latitude and the magnetic local time, where 1200 o'clock defines the position of the Sun. Reproduced from Axford [1964]

in the magnetosphere and the solar wind) breaks down. In this thin boundary layer magnetic reconnection occurs. Magnetic reconnection involves the change of magnetic connectivity of plasma fluid elements due to a localised diffusion region in a magnetic null (where there is a field reversal) x-point [Parker, 1957; Petschek, 1964]. Figure 1.15 shows an example of an x-point field configuration in the Sweet-Parker model of reconnection. Figure 1.16 shows a cartoon model of the steps that occur during the reconnection process and convection of the magnetic field. Field lines $1'$ (from solar wind) and 1 form an x-point (a magnetic configuration in which reconnection can occur) at the magnetopause. Reconnection occurs between these two field lines - the previous closed geomagnetic field line is now connected to the IMF whilst still being attached to the Earth. The frozen in condition still applies out in the

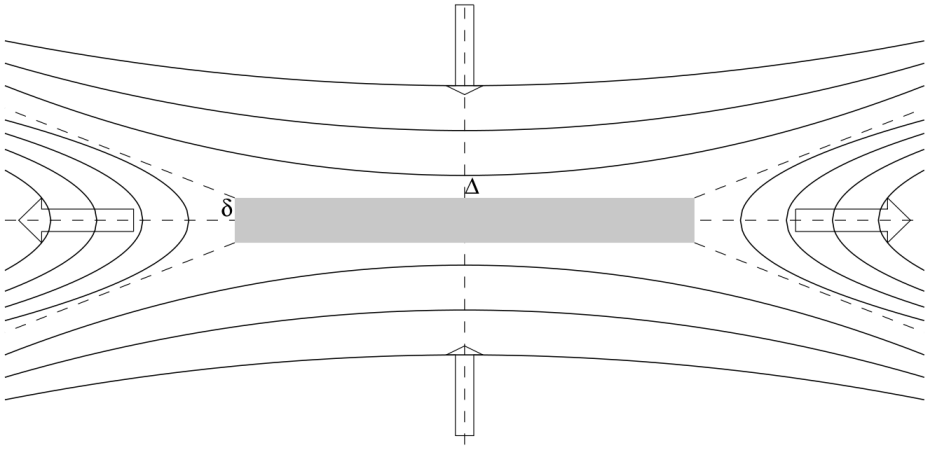

Figure 1.15: The x-point reconnection configuration in the Parker-Sweet model. The diffusion region is shaded grey. Reproduced from Aschwanden [2006]

IMF and so the new field lines, 2' and 2, are dragged anti-sunward with the solar wind. The movement of these field lines induces an effective electric field (equation 1.33) and, in a steady state, the field lines are equipotential. The electric potential is mapped onto the ionosphere and is directed from dawn to dusk. This electric field drives (or results from, depending on your viewpoint) anti-sunward flows from noon to midnight.

Eventually the field lines are stretched out into the tail and added to the existing flux there. This transport of flux, while easy to visualise, is not completely correct. Since the magnetic flux in the tail does not increase indefinitely there must be a process that convects the magnetic flux back to the dayside.

In the magnetotail, in a similar manner to the magnetopause under certain conditions, there can be a magnetic neutral x-point in which reconnection occurs. Figure 1.16 shows that field line 6 and 6' reconnect in the tail. Field line 7' is disconnected from Earth and reconnected purely to the solar wind, whereas field line 7 is now reconnected solely to the Earth. These newly con-

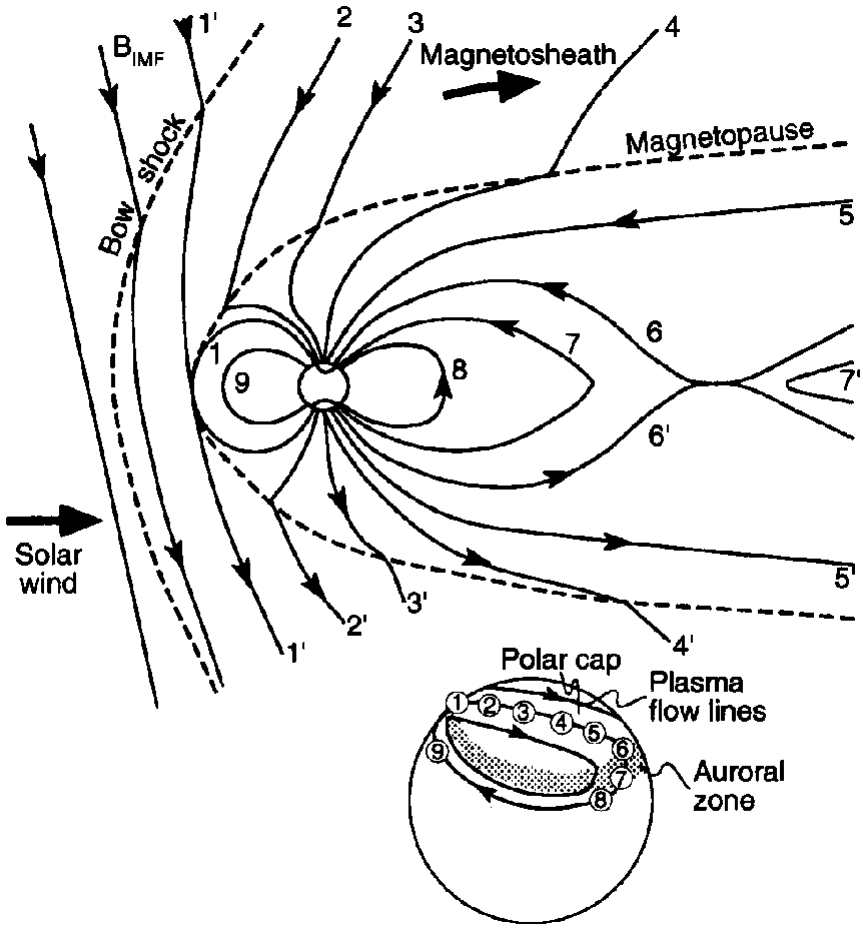

Figure 1.16: A diagram that shows how field lines reconnect and are convected in the magnetosphere by the soar wind. In the bottom of the figure the field lines are mapped down to their foot points in the on Earth. Reproduced from Kivelson and Russel [1995]

nected field lines flow around either the dawn or dusk side of the Earth where they return to the dayside. At the bottom of figure 1.16 the foot-points of the field lines involved in the convection cycle are mapped onto the ionosphere. From the foot-points it is clear that this cycle produces a similar convection pattern to that in figure 1.14.

This picture of convection is greatly simplified. While key components, such as the return of flux from night side to day side must occur, it need not be that the rate of reconnection at the magnetopause is steady and matches that in the magnetotail. Magnetic energy may be stored in the tail for some time before reconnection in the tail occurs [Baker et al., 1997]. The release of this energy in the tail tends to happen rapidly ($\sim$ 30 minutes) and the resulting magnetopheric perturbations are known as magnetospheric substorms, which are discussed in section 1.5.1 [Baker et al., 1997].

Reconnection at the dayside can also occur under northward IMF conditions. Reconnection in this scenario occurs in the cusp regions [Crooker, 1979]. The convection cell topology is usually more complicated than a two-cell system in this scenario. During northward dominated IMF (i.e. the $|B_y|$ component is small compared to B_z) there is typically a 4-cell configuration, an example of which is shown in figure 1.17. The lower latitude potential cells on the nightside are associated with the typical two-cell configuration, with the negative cell on the duskside and the positive cell on the dawnside (i.e. anti-sunward flow of plasma). However, the two high latitude cells indicate a sunward flow of plasma or a dusk to dawn directed electric field. The magnitude of the cross-polar cap potential is different during southward and northward IMF conditions. With potential differences of $\phi_c \sim 10 - 30$kV and flow speeds of $\sim 300ms^{-1}$ during northward conditions and potential differ-

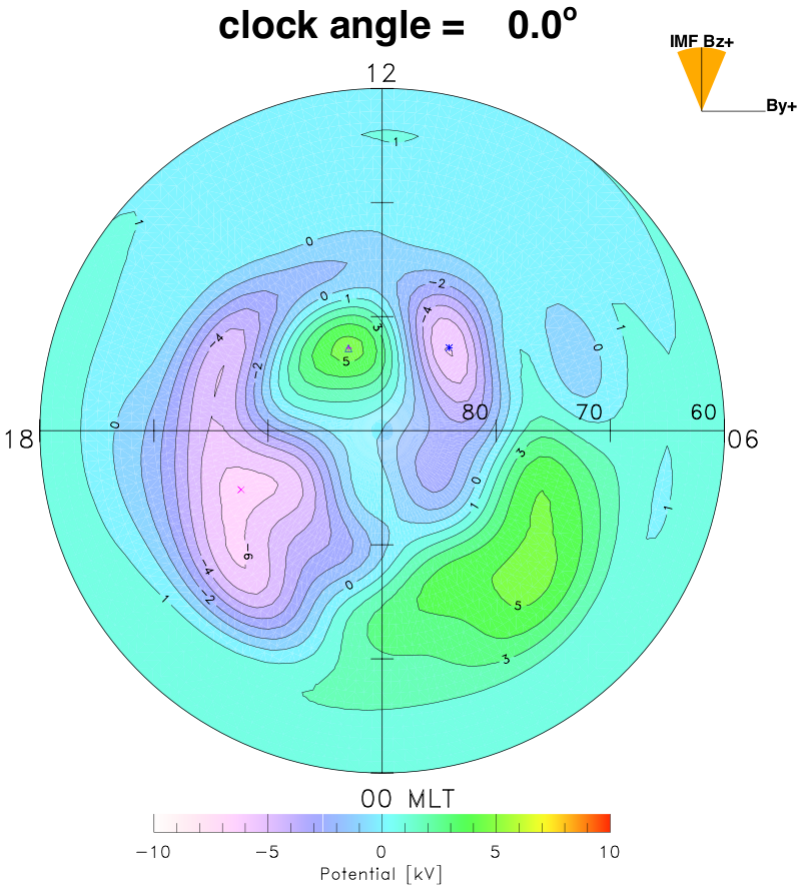

Figure 1.17: Diagram showing how FAC might be generated from a perturbation of the inner edge of the plasma sheet. Reproduced from Forster et al. [2008]

ences of $30 < \phi_c < 120kV$ and flow speeds $1000ms^{-}1$. Where $\phi_c < 120kV$ is the empirically derived cross-polar potential saturation point [Nagatsuma, 2002].

1.4.2 The Influence of IMF B_y

In section 1.4.1 a rudimentary model of convection was given which depended on the state of B_z. It soon became clear the IMF B_y component modifies the location of reconnection at the magnetopause [Crooker, 1979], and hence the shape of the resulting convective cells mapped onto the ionosphere. A useful

parameter for investigating the influence of IMF B_y on convection is the clock angle,

$$\theta_{imf} = \arctan \frac{B_y}{B_z} \tag{1.36}$$

as B_z is still the primary parameter controlling convection. During this section any reference to the distortion of the convection system as mapped onto the ionosphere will refer to observation in the northern hemisphere. Typically the broad stroke picture is reflected in the south pole, i.e. a clockwise rotation becomes an anti-clockwise rotation.

Figure 1.18 shows the statistical averages of the convective potential cells in the northern hemisphere for different clock angle conditions [Haaland et al., 2007]. The electric potential is calculated by determining the velocities of ions in the ionosphere using radar measurements (and then extrapolating the electric field from equation 1.33). The potential cells are determined during "stable" IMF conditions, which are conditions where the clock angle has remained steady for 30 minutes. Steady condition are required as the convection system takes a finite amount of time to reconfigure. For dominant $+B_y$ conditions there is a rotation of the maximums of the positive and negative cells in the clockwise direction and anti-clockwise rotation for $-B_y$.

In addition to the rotation of the symmetry axis of the cells, the shape of the convection cells is distorted. During periods of -B_y the dusk potential cell forms a more crescent shape while the dawn cell becomes more rounded (the opposite is true under $+B_y$). While B_y influences the shape and orientation of the convection cells, the total potential drop across the polar cap is almost exclusively controlled by B_z [Ruohoniemi and Greenwald, 1996]. The length of time in which the solar wind has been in a particular driving state influences

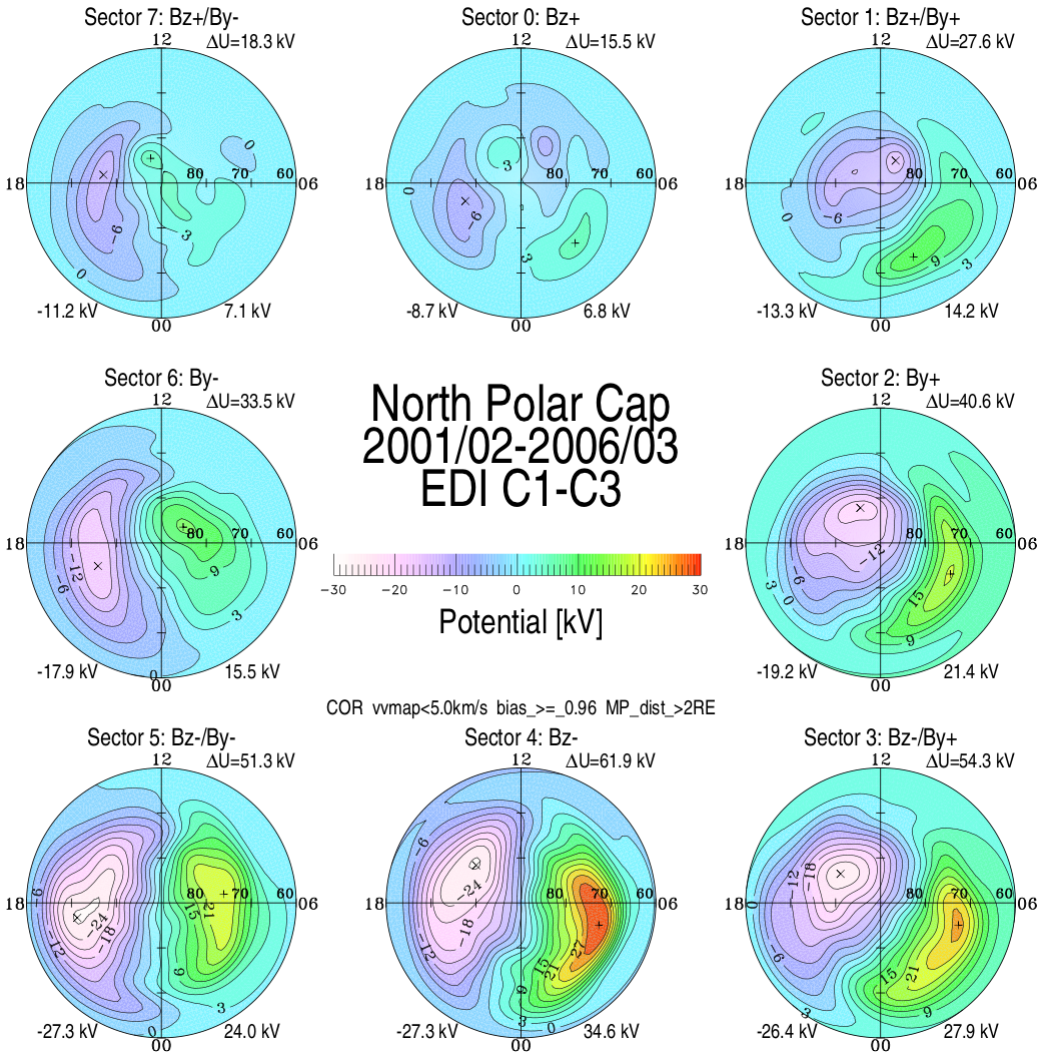

Figure 1.18: Statistical averages of the ionospheric potential under different clock angle conditions. Reproduced from Haaland et al. [2007]

the evolution of the convection within the magnetosphere [Grocott and Milan, 2014].

It has been noted that there tends to be an inherent asymmetry in the dusk and dawn cells even when $|B_y| \ll |B_z|$. Typically the dusk potential cell has a greater latitudinal extent and magnitude [Ruohoniemi and Greenwald, 1996; Grocott and Milan, 2014]. In addition, from figure 1.18, the symmetry axis of the convection cells has an inherent clockwise rotation. Two potential explanations have been proposed. One possibility is that there is additional reconnection occurring on the the duskside flank of the magnetosphere [Watanabe et al., 2007]. However, exactly why this additional reconnection occurs only on the duskside is unclear.

Another possibility is that there is a large gradient in ionospheric Hall conductivity in the transition from sunlit areas to non-sunlit areas [Ridley et al., 2004; Tanaka, 2001] found in the dusk region that is responsible for the asymmetries. Simulations by Zhang et al. [2012], which included realistic ionospheric conductivity, showed the same observed asymmetries. Importantly, these asymmetries disappear under the condition of uniform conductance in the ionosphere. The Hall conductivity gradients cause more of the flux that is opened at the magnetopasue to be diverted towards the duskside, creating a rotation of the symmetry axis in a two-cell convection configuration. This preferential duskside transport has consequences for the reconnection and return convection that occurs in the magnetotail (i.e. substorms) [Walsh et al., 2014].

1.5 Space Weather

In the earlier stages of magnetospheric research it was noted that massive perturbation in the Earth's magnetic field occurs as measured from ground. These events are known as magnetospheric substorms and storms. Despite the nomenclature, a storm is not a made up of several substorms (although substorms do often occur during storms) but they are distinct phenomena [Kamide et al., 1998]. Key to this topic was how the required energy budget for these events was supplied by the solar wind.

1.5.1 Substorms

Section 1.4 considered the convection of the magnetic field from the magnetic pause to the magnetotail where the flux accumulates. Such a situation requires a mechanism that dissipates the energy build up in the tail. Substorms are the primary mechanism through which this occurs. Although the basic morphology of a substorm and its impact on the aurora has been known for some time [Akasofu, 1964], magnetospheric substorms are still an active field of research [Sergeev et al., 2012]. This section explores how substorms manifest in ground based measurements of the magnetic field and aurora, the different competing models that detail the sequence of events and the current outstanding problems in the area.

In the identification of substorms, the auroral indices AL, AU and AE have found indispensable use. These indices are derived from 13 magnetometer stations in the auroral zone. AU is the maximum field perturbation in the north component of the magnetic field (from baseline) out of the group of stations at a given point in time. Likewise, AL is the minimum perturbation of

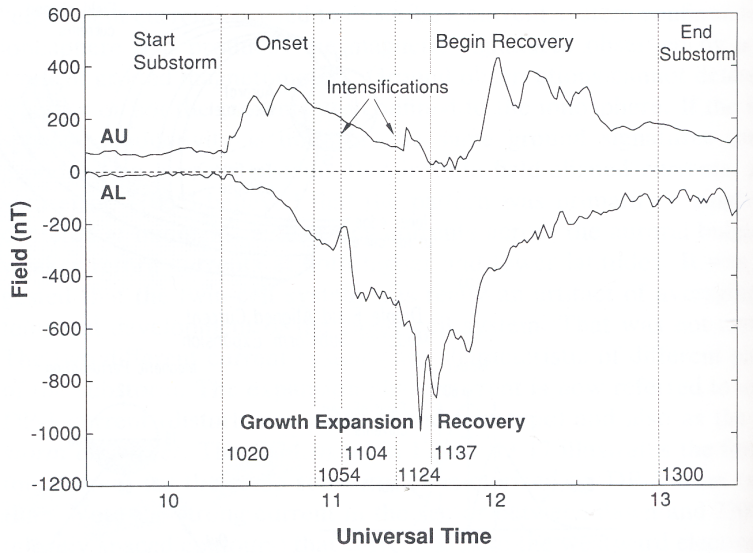

Figure 1.19: Shows AL and AU as a function of time for the 22nd March 1979 substorm. Labelled are the phases of a substorm. Reproduced from Manka [1985]

the same group. AE is simply the difference between the two (AE = AU − AL). As such the location of the max/min field perturbation can hop between stations. The north (or H-horizontal) component of the magnetic field measures perturbations resulting from horizontal currents in the ionosphere. An east to west horizontal current in the ionosphere will cause a decrease in the north component of magnetometers.

Figure 1.19 shows the AL and AU indices as a function of time for a particular substorm. Labelled are the 3 different phases of a substorm - growth, expansion and recovery. The growth phase occurs when the IMF turns southward and flux begins to accumulate in the magnetotail. This convection manifests as gradual increases and decreases in AU and AL respectively. A feature that may accompany is the enlargement of the auroral oval (usually indicative of open flux accumulation in the tail) [Brittnacher et al., 1999]. The onset of the expansion phase signals the release of the stored energy in the magne-

totail During this phase an intense east-west current forms in the ionosphere across magnetic midnight known as the auroral electro-jet[Schindler, 1974]. This causes a rapid decrease in the AL index. The electro-jet forms due to reconnection in the near Earth plasma sheet and is supported by intense Field Aligned Current (FAC) originating from there. An intense brightening of the aurora where upward field aligned currents occur accompanies this phase of a substorm. In addition, periodic pulsations of around 40-120s in the magnetic field (known as PI-2 pulsations) accompany the onset of the expansion phase at mid latitudes [Olson, 1999]. The auroral brightening starts out localised and then expands upward then westward (hence the term expansion phase). AL eventually reaches minimum which signals the beginning of the recovery phase. This phase is typically thought of as a relaxation of the perturbed system back to its ground state and a movement of the reconnection location out to the distant tail (where it is normally located) [McPherron et al., 1973].

Several models exist to explain the sequence of events listed above. The growth and recovery phase are thought to be well understood [Sergeev et al., 2012] whereas the models tend to disagree on the exact mechanisms and sequence of events that cause the onset of the expansion phase. Two main models of the substorm expansion phase exist: the near-Earth neutral line model (NENL) and the current disruption model (Current Disruption (CD)).

The Near Earth Neutral Line (NENL) model is arguably the most developed [Baker et al., 1996]. Figure 1.21 shows a basic view of the sequence of events that occurs in the NENL model. The piling of additional flux in the magnetotail (due to reconnection at the magnetopause) thins the current sheet in the tail drawing the oppositely directed field lines closer together. This

forms an x-point close to the Earth ($\sim 20-30R_E$) where reconnection can take place. Reconnection at the x-point signals the onset of the expansion phase. The reconnection causes a plasmoid (a coherent structure of plasma and magnetic fields) to be launched anti-Sunward [Hones, 1984]. On the Earthward side of the reconnection site there is a dipolarisation (where the magnetic field becomes more dipolar) of the magnetic field, along with earthward directed bursty bulk flows produced at the reconnection site. When these flows reach the inner magnetosphere they produce the FAC and the substorm current wedge. The substorm current wedge is depicted in figure 1.20. Shiokawa et al. [1998] proposed a mechanism for the generation of the substorm current wedge due to the flows. As the bulk flows approach the boundary between the dipolar and the tail-like configurations they are slowed by the increased plasma and magnetic pressure in the region. The piling up of magnetic flux from the reconnection site acts to expand the dipolar part of the field tailward, inducing a localised dusk-dawn current (a current oppositely directed to the existing cross-tail current). To maintain total current continuity the currents are rerouted through the ionosphere via FAC.

The CD model shares many similarities with the NENL model and in a basic view they only differ in the time sequence of events. Figure 1.22 displays the time sequence of events for the current disruption model. This model starts out identical to the NENL model, in that there is a thinning of the current sheet near Earth due to the piling of magnetic flux from reconnection at the magnetopause. The thinning reaches a certain point such that there is a plasma instability in the current sheet that causes a disruption of the cross-tail current. Like the NENL model, the current is rerouted through the ionosphere forming the substorm current wedge. This instability also produces

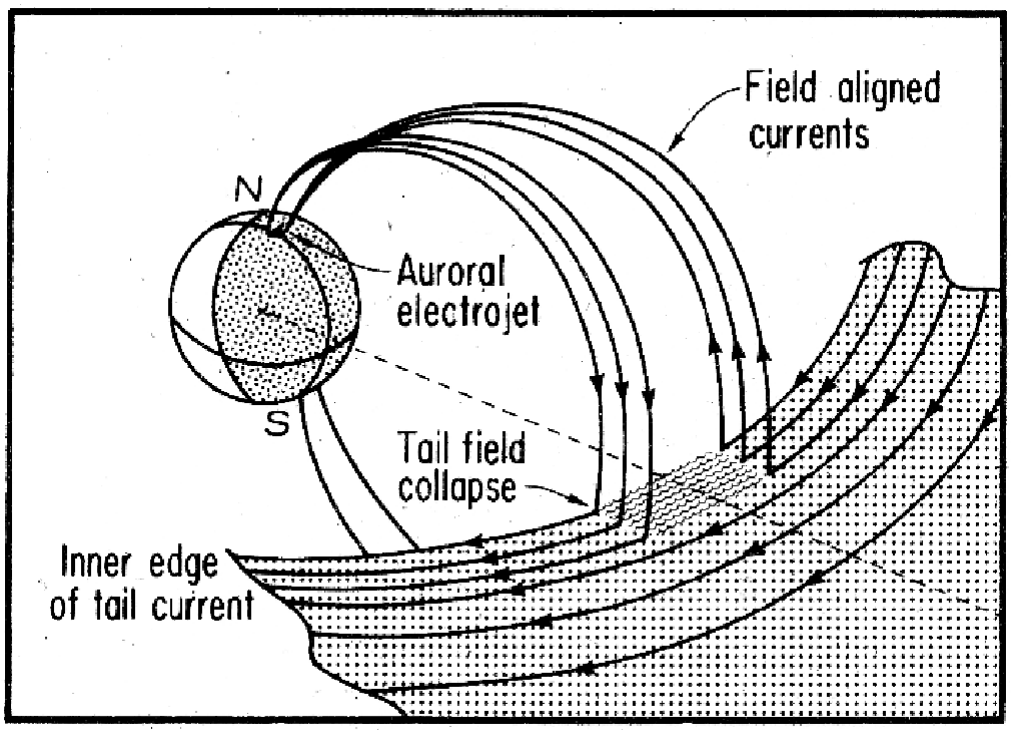

Figure 1.20: How the current wedge is formed as postulated by McPherron et al. [1973]. Changes in the magnetotail causes the the cross-tail currents to be rerouted through the ionosphere via the inward and outwards field aligned currents. The East-West current system formed in the ionosphere is known as the auroral electrojet. Reproduced from Kivelson and Russel [1995]

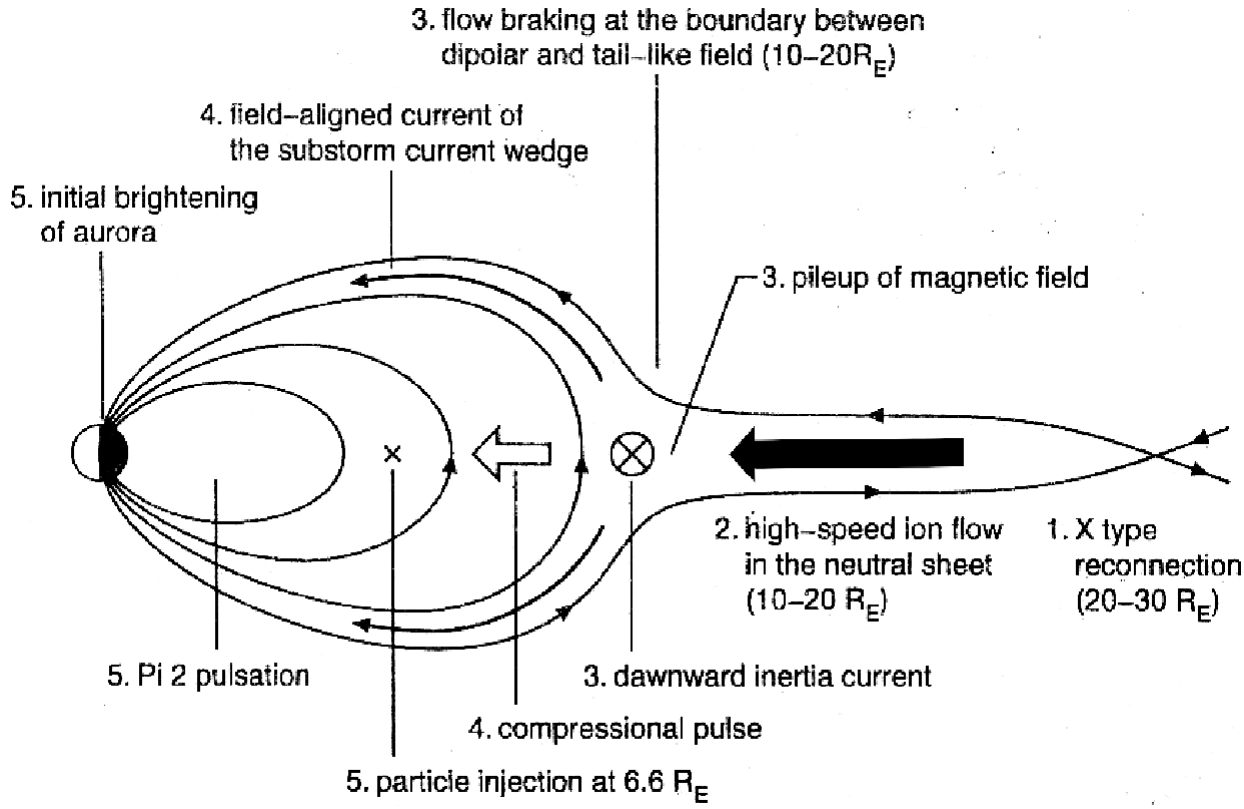

Figure 1.21: Shows the different stages of the NENL model. The numbers indicate the time sequence of events. Reproduced from Shiokawa et al. [1998]

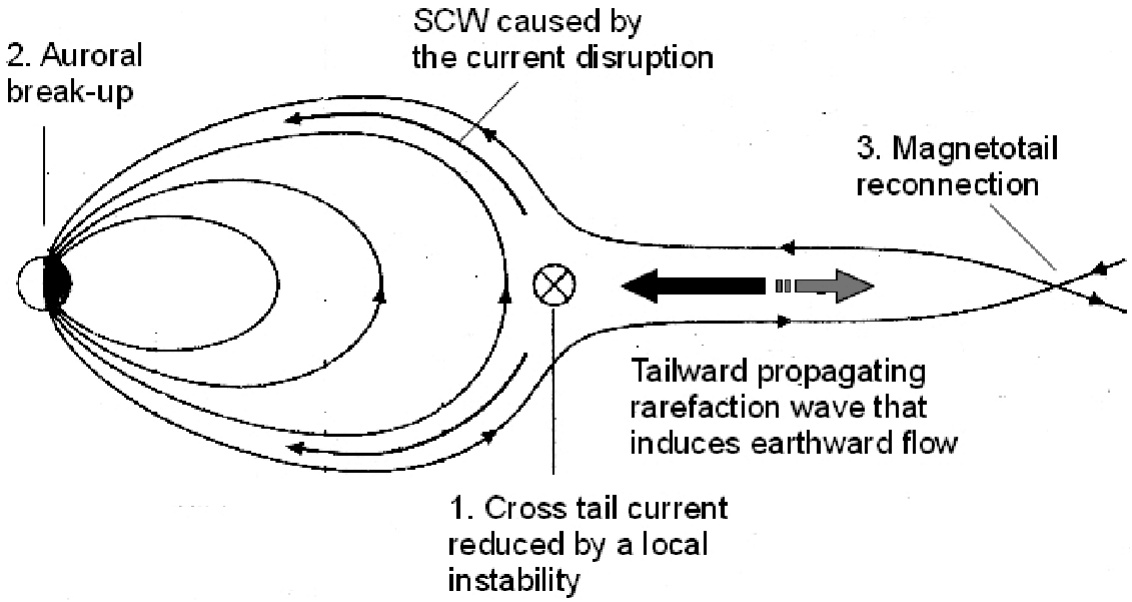

Figure 1.22: Shows a modified version of figure 1.21 labelling the different stages of the CD model. Reproduced from Koskinen [2011]

a refraction wave that initiates reconnection in the tail causing bulk flows to move towards Earth.

Definitive evidence on what the true sequence of events is lacking. Evidence has been found that supports the NENL model [Gabrielse et al., 2009; Angelopoulos et al., 2008] as well as those that do not support either model [Lui et al., 2008; Lin et al., 2009]. Another issue with both models is in the detailed causes of either the reconnection or the instabilities that cause the current disruption. Put another way there is no specific threshold for the amount of either the flux accumulation in the tail that initiates the reconnection or the instability that causes the substorm current wedge. Observations have linked sharp south-north turnings in the IMF (as well as variations in B_y) to the triggering of substorms [Lyons, 1996]. Despite this, a significant percentage of substorms appear to occur with no external triggering [Henderson et al.,

1996].

In section 1.4.2 the asymmetry (a clockwise rotation of the symmetry axis of the convection cells) of the convection system was discussed. This asymmetry is reflected in the current density on the duskside of the magnetotail [Davey et al., 2012] and the auroral brightening onset location of substorms being located on the duskside of magnetic midnight [Gjerloev et al., 2007].

It is possible that there is no single mechanism that causes of the substorm current wedge. This is consistent with the observations of substorms. Statistical studies of substorms reveal that there is a wide range of characteristic timescales over which they occurs and varying amounts of energy deposition [Newell and Gjerloev, 2011a].

This raises an important question, are the substorm events referred to in the literature all the same type of event or are they different phenomena being incorrectly grouped together under the umbrella of substorms?

1.5.2 Steady Magnetic Convection

Substorms convect plasma and magnetic field from the tail back towards the dayside in a storage and release cycle. Theoretical arguments have shown that steady reconnection in the tail leads to an unstable magnetic configuration in the magnetotail [Erickson, 1992]. If the IMF is southward for $\sim$ 1hour then there is a very high probability of a substorm [Kamide et al., 1977], however, there are times of enhanced convection but no substorm signatures [DeJong et al., 2008; Nishida and Nagayama, 1973]. These periods have been termed steady magnetic convection events.

Broadly speaking, Sergeev et al. [1996] defines steady magnetic convec-

tion as periods of enhanced energy input over several hours (minimum of 4-6 hours) during which the large scale stability of the magnetotail is preserved. During this time enhanced convection occurs, where AE increases to $\leq$200nT. In addition, no substorm signatures occur on the ground (PI 2 pulsations) and no current disruption or plasmoid releases occur in the magnetotail. During this time reconnection is balanced much like the idea originally posed by Dungey [1961]. Often it is hard to distinguish substorm events from Steady Magnetic Convection (SMC) events and questions remain on under what conditions these events occur [Sergeev et al., 1996].

1.5.3 Magnetospheric Storms

A magnetospheric storm is a period of time lasting hours to days in which the magnetic field within the magnetosphere is strongly perturbed. Storms occur from strong direct continuous driving of the magnetosphere by the solar wind. The driving usually consists of a strongly continual southward IMF and strong increases in dynamical pressure. Magnetospheric storms are identified in the DST index; this index measures the strength of the ring current by stations at mid latitudes. Weak storms may have DST of around $\sim$-30nT whereas very strong storms have $DST < -200nT$ [Loewe and Prölss, 1997].

Figure 1.23 shows the timeseries of DST for a typical storm. A storm is often broken up into 3 phases [Burton et al., 1975]. The initial phase of the storm consists of an increase in DST which may last several hours. This phase is associated with increased dynamical pressure on the dayside magnetopause pushing the magnetopause current closer to Earth. This phase is not always present [Perreault and Akasofu, 1978]. The main phase of the storm consists

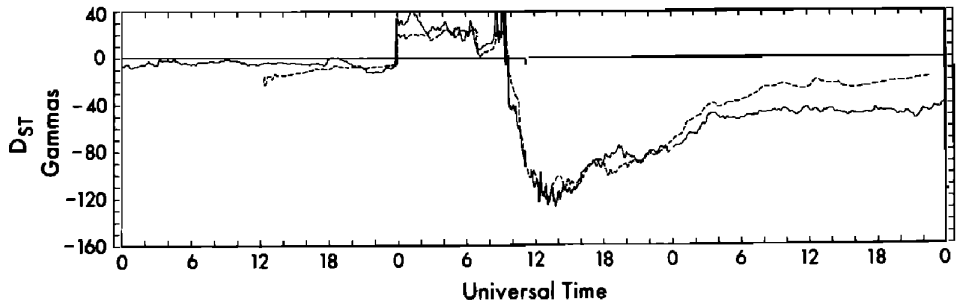

Figure 1.23: Shows DST as a function of universal time during a magnetospheric storm occurring on 15-17 Feb 1967. Reproduced from Burton et al. [1975].

of an almost uniform global perturbation of northward directed magnetic field around the Earth. This is due to the enhancement and movement of the ring current towards Earth. The increased $E \times B$ drift due to enhanced convection under strong southward IMF condition in the plasma sheet pushes the ring current closer to Earth [Burton et al., 1975]. The resulting perturbation in the field threading the ring current causes FAC through which the ring current becomes populated by oxygen ions from the ionosphere. After the main phase is the recovery phase. In this phase the ring current gradually weakens to its ground state. The recovery phase is usually triggered by the return of normal solar wind conditions. The lack of a strong convective electric field allows the ring current to relax and move away from Earth. In addition, charges in the ring current undergo pitch angle scattering which depletes the number of particles in the ring current. The recovery phase can last several days.

Magnetospheric substorms are also one of the main features that occur during storms. Initially storms were made up of many substorms (hence the name). However, substorms alone do not explain the symmetric enhancement of the ring current.

1.5.4 Space Weather Impacts

Processes that cause major disturbances in the magnetosphere have been a topic of in depth study for decades. This is not only to improve our understanding of plasma interactions but because major events can have significant impacts on a technological society. In this section we briefly summarise some of these impacts.

Large perturbations in the magnetic field on Earth and in the magnetosphere can have severe consequences. From equation 1.4, temporal variations in the magnetic field cause an associated electric field. These electric fields can induce currents in conductive materials on Earth. In the most extreme magnetic storms, the electrical power grid is susceptible to large fluctuations in current which can lead to black-outs and permanent damage to the grid [Kappenman, 1996]. Milder impacts include induced currents that flow from oil pipe lines to ground causing an increased corrosion of pipelines [Boteler, 2000].

Energetic electrons accelerated by substorm events can cause the degradation of satellites in orbit around Earth. The energetic electrons can penetrate the spacecraft shielding and lodge themselves in insulating materials. Over time large potential differences can occur and the accumulated electrons can be discharged potentially damaging or interfering with the operation of the satellite [Garrett, 1981].

Satellite-Earth communication relies on frequency bands able to penetrate through the ionosphere. As the waves travel through they can be refracted and slowed in regions of intense auroral currents. This is problematic for GPS systems and can effect the positioning calculations [Pulkkinen, 2007].

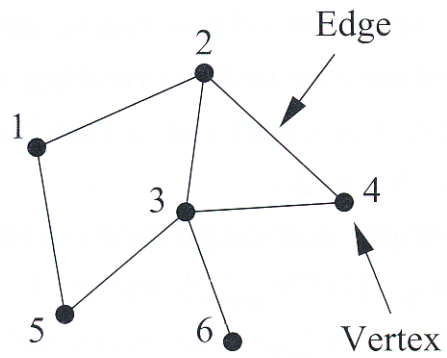

Figure 1.24: Example of a simple undirected network. Reproduced from Newman [2010].

Radio communications that utilise the bounce of the waves off the ionosphere to send long range communications are also affected. The changing charge densities in the ionosphere during space weather events can cause the waves to be absorbed rather than reflected [Pulkkinen, 2007].

1.6 Network Terminology

This short section defines the basic concepts of networks (known as graphs in mathematics) and the associated terminology that is used in this thesis. In simplest terms a network is a collection of connected points (or nodes/vertices). Mathematically the connections (or edges/links) are represented by the adjacency matrix, A_{ij}, where i and j index the nodes in the network. In its simplest form the adjacency matrix is binary such that

$$A_{ij} = 1 \begin{cases} 1, & \text{if i and j are connected,} \\ 0, & \text{otherwise.} \end{cases} \tag{1.37}$$

Figure 1.24 shows a simple network which will have a corresponding adjacency

matrix,

$$A_{ij} = \begin{pmatrix} 0 & 1 & 0 & 0 & 1 & 0 \\ 1 & 0 & 1 & 1 & 0 & 0 \\ 0 & 1 & 0 & 1 & 1 & 1 \\ 0 & 1 & 1 & 0 & 0 & 0 \\ 1 & 0 & 1 & 0 & 0 & 0 \\ 0 & 0 & 1 & 0 & 1 & 0 \end{pmatrix}.$$

This simple network is undirected, hence the adjacency matrix is symmetric. In general A_{ij} need not be binary or undirected. That is, the connection between i and j can be both in a particular direction (i.e. from i to j only) and have a strength. Depending on the circumstances this strength could manifest through some measure of how strong the connection is between two nodes or whether the two nodes have multiple connections between them. General convention dictates that if $A_{ij} = 1$ for a directed network then this means a connection from j to i.

By summing the adjacency matrix over n nodes for one index, the degree, k_i, for a node i can be obtained,

$$k_i = \sum_{j=1}^{n} A_{ij}. \tag{1.38}$$

The degree is the number of connections a particular node has and is a rudimentary measure of a node's importance in the network. If the network is directed then two degrees can be obtained, an in degree and an out degree.

Several measures of the network can be used identify the importance of nodes within it and its general structure, the functional forms of which can be found in any good textbook [Newman, 2010]. Such measures include, the

betweenness centrality, which is a measure of the extent to which a node lines on the paths between other nodes [Freeman, 1977]. The clustering coefficient is the measures the extent of connection between neighbours of a node (e.g. if A is connected to B and C then how likely is it that C is connected to B). How small world the network is, which is the average number of degrees of separation between a particular node and a random node in the network. This concept made famous by Milgram [1967] with the idea that everyone is connected to any other random person in a social network by six degree of separation.

In the next chapter we discus how we form the networks to characterise substorms and the quiet-time convection system. Specifically we consider the choice of nodes for the network, establishing connections between nodes, the choice of thresholds for the connections and how we interpolate the spatially inhomogeneous network onto a regular grid.

1.7 Measures of Similarity Between Timeseries

The goal of this thesis is to quantify and map the extent of spatio-temporal similarity between temporal variations in the magnetic field at different spatial locations on Earth. As such, a quantitative measure of singularity must be chosen. Measures of similarity between two timeseries can be broken down into two categories, linear and non-linear methods. Cross-correlation and spectral coherence are examples of measures of the linear relationship between two

timeseries. Bravais-Pearson cross-correlation, in the discrete case, is given by

$$C_{XY}(\tau)^2 = \frac{\sum_{t=1}^{N}(X(t)-\bar{X})(Y(t+\tau)-\bar{Y})}{\sqrt{\sum_{t=1}^{N}(X(t)-\bar{X})^2}\sqrt{\sum_{t=1}^{N}(Y(t)-\bar{Y})^2}}, \tag{1.39}$$

where τ is the delay, $\bar{X}$ and $\bar{Y}$ are the means for timeseries $X(t)$ and $Y(t)$ both of length N. In equation 1.39 the correlation coefficient, $C_{XY}(\tau)$, is normalised by the total energy of X and Y and can take values $-1 \leq C_{XY} \leq 1$. Where a $C_{XY}(\tau) = 1(-1)$ means the signals are maximally correlated (anti-correlated) and $C_{XY}(\tau) = 0$ means the signals are completely uncorrelated. The spectral coherence can be obtained by taking the magnitude of the Fourier transform of the numerator of equation 1.39, with the denominator remaining the same as a result of Parseval's theorem.

X(t) and Y(t) are either stationary (strong or weak) or non-stationary processes. Strong stationarity means that for given a stochastic process X_t, the cumulative distribution function of the joint distribution at times $t_1....t_n$, $F(t_1....t_n)$ is equal to that at times $t_1 + \tau.....t_n + \tau$ for all times, $F(t_1....t_n) = F(t_1 + \tau.....t_n + \tau)$. Weak stationarity (more commonly used for practical purposes) means that the mean and variance remain constant under shifts in time. If timeseries $X(t)$ and $Y(t)$ are non-stationary then as the number of samples N increases the sample correlation C_{XY} in equation 1.39 does not converge to a particular value.

Mutual information is an example of a non-linear statistical dependence measure. Mutual information is linked to the concept the entropy of a random variable. For discrete bivariate random variables, mutual information is given

by []

$$I_{XY} = \sum_{i,j}^{N,M} p(x_i, y_j) log \left(\frac{p(x_i, y_j)}{p(x_i)p(y_j)} \right). \tag{1.40}$$

Where $p(x_i, y_j)$ is the joint probability of random variables $X = x_i$ and $Y = y_j$, and $p(x_i)$ and $p(y_j)$ are the probabilities of $X = x_i$ and $Y = y_j$ respectively. I_{XY} is the coefficient that describes the level of statistical dependence between X and Y and can take values $I_{XY} \geq 0$. $I_{XY} = 0$ means X and Y are completely unrelated. If the joint probability follows a normal distribution then C_{XY} is directly relateable by

$$I_{XY} = -\frac{1}{2} log \left(1 - C_{XY}\right). \tag{1.41}$$

Since mutual information can detect both non-linear and linear statistical dependence it is in theory a better measure than regular correlation. However, problems arise in assigning correct probability distribution functions for X and Y, which may require infeasible amounts of data depending on the forms of the distributions.

1.8 Motivation - Quantifying Spatio-Temporal Evolution of Large Scale Current Systems

Satellites in various orbits in the magnetosphere make direct measurements of physical quantities. For intermittent physical processes (i.e. substorms) they must be in the right place at the right time. This does not happen frequently since the magnetosphere is quite large. In addition, there is a significant amount of memory in the system, that is, the time history of what

occur before an event is of particular importance. Therefore, while space based measurements are important they are limited by their sparsity in space and their ability to measure continuously in one spatial location over extended periods of time (barring geostationary satellites in the inner magnetosphere).

To supplement space based measurements a continual monitoring of the large scale systm would be invaluable. Ground based measurements are currently the only reasonable way to accomplish this. Magnetometer and radar measurements are the primary ground based measurements. Radar measurements use the Doppler effect to measure the line of sight bulk flow velocity of ions in the E and F regions of the ionosphere. By assuming the flow of ions is from the $E \times B$ drift, the electric potential in the ionosphere can be determined (see figure 1.18). Hence, to fully reconstruct the convection system there needs to be multiple radars looking at the same parcel of plasma from different angles. Alternatively, time separated measurements could be used. The radars move through magnetic local time (Magnetic Local Time (MLT)). MLT is defined by the position of the Earth-Sun line as such geographic positions move through MLT. By considering two time separated radar measurements the same reconstruction can be achieved albeit under the big assumption that the system has not changed significantly during that period of time.

Magnetometers measure perturbations in the magnetic field, usually after being baselined (i.e. removal of Earth's background field and other see chapter 2.1). The magnetic perturbations result from ionospheric current systems. The ionosphere is coupled to the rest of the magnetosphere via magnetic field lines that thread through both systems. Hence, these currents are a proxy for physical processes that are occurring in the magnetosphere.

Magnetometer station coverage at high latitude in the northern hemi-

sphere has increase remarkably over the past $\sim$ 70 years, however, useful ways of quantifying the global response has been lacking. Historically magnetometer time series were individually inspected during major geomagnetic disturbances or large scale scalar indices such as the auroral indices (AE, AU and AL) and DST were used (see section 1.5.1). The former is time consuming considering the large quantities of data now available and the latter is incredibly limiting as it provides no spatial information.

One goal is to completely reconstruct the global ionospheric current system from magnetic measurements. Under the assumption that the magnetic field perturbations result predominantly from Hall currents, equivalent currents can be reconstructed. In this method the ionospheric conductivities are also assumed. This is problematic during highly disturbed periods where strong FAC cause additional ionisation. The method is improved with the introduction of supplementary measurements and models for the conductivity. This falls under the umbrella of the assimilative mapping of ionospheric electrodynamics (Assimilative Mapping of Ionospheric Electrodynamics (AMIE)) technique Richmond [1992]. While an improvement, some assumptions about conductivity and the weighting to the different measurement is still present within the technique.

A difficulty presented all techniques related to the mapping of the spatio-temporal evolution of the ionosphere currents is the large gaps in coverage. One solution to this is to interpolate the data to fill in gaps in the coverage, this has been done with radar measurements [Ruohoniemi and Baker, 1998] and more recently ground station measurements [Waters et al., 2015]. Both methods involve fitting the data to a set of spherical harmonic functions, hence the general shape of the solution is restricted and is not unique. Alternatively,

a statistical approach can be taken in which the gaps in the data coverage are filled in by aggregating over many similar events [Gjerloev and Hoffman, 2014]. This approach has problems since there is likely significant time and spatial smearing due to the different global responses during the individual events.

Dynamical networks may be a potential method for mapping the spatio-temporal evolution of the system. Dynamical networks can be constructed by quantifying the similarity between measurements at different spatial locations as a function of time. This would give a measure of how coherent the system (or components of the system) responds to external (direct driving of magnetosphere by solar wind) and internal (substorms) forcing of the system. In a simplified view, the spatial pattern of connections would be indicative of the locations of the large scale ionospheric currents. This framework has obvious benefits over current established measures of geomagnetic activity such as AE and DST, which do not contain any spatial information. In addition, other methods for quantifying the current systems have to make assumptions about the system such as the conductivity. Ultimately dynamical network provide a unique unexplored interpretation of the ionospheric/magnetospheric system. Only ground measurements are required for the analysis, as such, large quantities of historic data can be leveraged to achieve a wide breadth of scientific aims.

The structure of the thesis is as follows. In chapter 2 we describe our methods for determining the networks, what we use as nodes, what methods we use to determine connections between nodes, how we use the similarity thresholds to account for inherent difference between nodes and how we map the network information onto a regular grid. In chapter 3 we construct net-

works for 4 test case substorms and define network parameters that describe the spatial distribution of similarity. In chapter 4 we construct the statistical response of the gridded network to north-south and south north IMF turnings. In chapter 5 we give our conclusions and potential future work.

Chapter 2

Constructing Correlation Networks for SuperMAG

2.1 Introduction

Networks are a versatile tool that can be used to characterise systems as a collection of components that are non-uniformly connected or interacting. Networks are currently used as a tool to analyse the internet, human social networks [Milgram, 1967], biological systems, engineering systems [Sivrikaya and Yener, 2004], the brain[Nicol et al., 2012], the climate [Radebach et al., 2013; Malik et al., 2012; Donges et al., 2009] and more. How network formalisation is used depends on the goals of the analysis of the flow of information dynamics; individual components (nodes) could be studied, the connections between them, the underlying global structure of the network or substructures within the network. Examples of networks include social networks, which may consist of people as nodes and connections as friendships between people. This formalisation could yield insights into how humans interact in societies. Internet

networks where internet domains are the nodes of the network and hyper-links to other domains form the connections. In both examples the identification of nodes and edges is unambiguous.

There has been interest in using network formalisations to analyse real world physical systems. A well explored example of this would be brain networks. In a fundamental network model of the brain the nodes would ideally be individual neurons. However, due to observational constraints (and the sheer number of neurons) nodes typically take the form of a spatial regions of the brain. The connections between brain regions can be determined in a number of ways, for example by looking at the extent of structural connectivity via physical connections between regions (fibre bundles)[Mori et al., 2002]. An alternative method would be to look at functional connectivity by considering the similarity of brain activity between different spatial regions (with brain activity being measured using proxies such as magnetoencephalography (MEG) [Nicol et al., 2012], electroencephalograms (EEGs) [Smit et al., 2008] or functional nuclear magnetic resonance imaging (NMRI) [Wang et al., 2009]). More recently climate networks have become a topic of interest. Like brain networks, the nodes typically take the form of spatial regions with connections between regions based on the similarity in the temporal variations of the local properties of a region (such as temperature, pressure, and rainfall).

Both of these networks approaches challenges that do not arise in networks where the node and connection choices are unambiguous. Difficulties include, choosing the optimal parcelling of the spatial regions - should regions all have the same physical size or be based on the characteristics of specific regions? Network nodes in physical systems will vary in terms of the sensitivity and accuracy of their measurements and different background responses.

The extent of the fundamental differences between either nodes or the measurement of nodal properties needs to be considered to determine whether the nodes should be given equal weight in the network. This is central to the choice of the method to compare nodal properties to establish whether there is a connection. There needs to be a method to identify an optimal quantitative similarity threshold that determines whether a node pair is connected.

In the following sections we address some of these problems in the context of networks representing ionospheric/magnetospheric observations. We first describe the methods used to form the networks in a generic manner; the specific optimisations for the type of events under study, such as correlation window length, are presented in later chapters. In section 2.2 we discuss the choice of magnetometer stations for the nodes of the network. In section 2.3 we summarise canonical correlation and how it is used to establish connections in the network. In section 2.4 we establish methods for calculating correlation thresholds used to form the network. Finally in section 2.5 we discuss our method of mapping the network information on to a regular grid.

2.2 Magnetometer Stations as Nodes in the Network

We model the ionospheric/magnetospheric system as seen in the ground based magnetometer response as a dynamic network of connected spatial locations so as to improve our understanding of the physical processes occurring therein. Initially we choose to use individual magnetometer stations as the nodes of our network and in this section we discuss the aspects of the stations that could

Figure 2.1: View from magnetic north of magnetometer stations (green dots) in northern hemisphere. (http://www.supermag.jhuapl.edu)

affect the network properties.

The geographical position of the magnetometer stations in the northern hemisphere is shown in figure 2.1. The stations are not evenly distributed spatially throughout MLT-MLat (magnetic local time and magnetic latitude); this spatial inhomogeneity may affect the network construction and resulting descriptive parameters due to missing information [Bullock et al., 2010].

Since the system of interest here is the magnetosphere/ionosphere, a natural choice for the coordinate system is MLT-MLat, which is imposed by the position of magnetic north and the sun-earth line. The magnetometer stations are not stationary in this coordinate system therefore the magnetic field recorded in a finite window of time constitute measurements for a sequence

of spatial locations. Stations at lower latitudes have a greater physical sample spacing than those at higher latitudes. We will take this into account when constructing a regular grid to which we map the network information in section 2.5.

The magnetic field measurement at a particular station is a summation of contributions of all current elements. We are only interested in the dynamics of the ionosphere/magnetosphere system. Therefore, ideally each vector magnetic field time-series would only include contributions from currents of a magnetospheric or ionospheric origin. A non-exhaustive list of contributions to the raw magnetic time-series measurements would be,

$$\mathbf{B} = \mathbf{B_E} + \mathbf{B_{Sq}} + \mathbf{B_{FAC}} + \mathbf{B_{RC}} + \mathbf{B_{EJ}} + \mathbf{B_{MP}} + \mathbf{B_{OC}} + \mathbf{B_{GI}} + \mathbf{B_{MM}}..., \quad (2.1)$$

where B the measured field which is made up of contributions from the Earth's field ($\mathbf{B_E}$), the Sq currents ($\mathbf{B_{Sq}}$), daily variations in the magnetic field), the field aligned currents ($\mathbf{B_{FAC}}$),the ring currents ($\mathbf{B_{RC}}$), the electrojet ($\mathbf{B_{EJ}}$), the magnetopause currents ($\mathbf{B_{MP}}$) 1, oceanic currents($\mathbf{B_{OC}}$), ground induction currents ($\mathbf{B_{GI}}$) and man made sources ($\mathbf{B_{MM}}$). There is no fundamental approach to removing the superfluous current sources, however, by considering the time-scales the sources vary on some of the contribution from some of the unwanted sources can be removed. There is no first principle approach to determining baselines and there are many different methods available [Janzhura and Troshichev, 2008; Joselyn, 1989]. We use magnetic time-series data from the SuperMAG database of ground station magnetometers. The aim of the SuperMAG baseline is to remove non-magnetospheric contributions to $\mathbf{B}$. The

time-series from all the magnetometers in the SuperMAG database have the benefit of being pre-processed in an identical way to remove the long term trends [Gjerloev, 2012] (≥ 1 day). The vector time-series are in local magnetic coordinates [Gjerloev, 2012],

$$B(t) = [B_N(t), B_E(t), B_Z(t)], \tag{2.2}$$

which differ from the more traditional "compass" HDZ coordinate system. The choice of coordinate system is of little relevance in the context of this thesis due to the method used to establish similarity between magnetometer station measurements in section 2.3.

In addition the instrumentation used by different magnetometer groups varies, as such they may have different response profiles, dynamical ranges and precisions. These variations across different instrumentation needs to be taken into account when identifying similarities in time-series measurements.

In summary, using magnetometer stations for the nodes in the network has several problems that could affect the network construction that we will need to address. Some of these problems are listed below:

1. The differing instrument response functions for each station.
2. The geographical variability between stations such as ground conductivity and ocean proximity etc.
3. The spatial inhomogeneity of the nodes.
4. The movement of stations through MLT as the Earth rotates.
5. The differing levels of sunlight in dayside region of the northern hemi-

sphere during different seasons affects the ionospheric conductivity.

In section 2.3 we address items 1 and 2 with the methods used to construct the network. We attempt to mitigate item 3 in two ways. First, we investigate substorm (see chapter 1) events where the stations are in a similar configuration at the start of each event (we do this for a carefully selected number of substorm events in chapter 3). This solution is limited by the number of available events for comparison for any given configuration. Alternatively, we address the spatial inhomogeneity by aggregating network information over number of similar events and mapping this information onto a regular grid (we do this both to construct the average substorm in chapter 3 and to find the aggregate network responses to IMF turnings in chapter 4). We outline the methodology for mapping network information to a regular grid in section 2.5. The missing network information, due to a lack of station coverage, is "filled in" over several events to give a average network response. The movement of stations through MLT is factored into the choice of the regular grid in section 2.5.

2.3 Identifying Links in the Network

We wish to establish the extent of similarity between temporal variations of the vector time-series of magnetometer stations. The magnetometer time-series are inherently non-stationary as there are many long term trends present as well as bursty activity (e.g. substorms) and as such they bear resemblance to the geophysical time-series used to establish networks in a climate context. Radebach et al. [2013] lists a number of methods that have been used in the construction of climate networks. Examples include linear (Bravais-Pearson)

correlation [Tsonis and Roebber, 2004], (cross-)mutual information [Donges et al., 2009], a phase synchronization index based on the normalized Shannon entropy of the associated phase difference time-series [Yamasaki et al., 2009], the (cross-)mutual information of order patterns [Barreiro et al., 2011], event synchronization [Malik et al., 2012] or transfer entropy [Hlinka et al., 2013]. Details of their use in a climate context can be found in the above references and we briefly outlined mutual information in chapter 1. Parameters used to establish connections in climate networks are typically scalars such as temperature, pressure and rainfall. Here we have the vector time-series measurements of the magnetic field. While a single component of the magnetic field could in principle be used there are significant drawbacks to this; the magnetic components, which vary in response to ionospheric currents, depend on the relative spatial position of the magnetometer station with respect to the currents. Using a single component means we may miss correlated pairs of signals that are in orthogonal components.

Canonical correlation [Brillinger, 1975] offers a potential solution to this. Jackel et al. [2001] has already investigated its use with respect to magnetometer station pairs. Canonical correlation defines a new coordinate system $\mathbf{X}' = [X_1'(t), X_2'(t), X_3'(t)]$, $\mathbf{Y}' = [Y_1'(t), Y_2'(t), Y_3'(t)]$ for a given vector time-series pair $\mathbf{X}(t)$, $\mathbf{Y}(t)$ in which the cross-correlation coefficient $r_{X_1',Y_1'}$ between first canonical components $X_1'(t)$ and $Y_1'(t)$ is maximised. Here $\mathbf{X}'(\mathbf{t}) = \mathbf{R_X}\mathbf{X}(\mathbf{t})$, $\mathbf{Y}'(\mathbf{t}) = \mathbf{R_Y}\mathbf{Y}(\mathbf{t})$ and $\mathbf{R_X}$ and $\mathbf{R_Y}$ are the respective rotation matrices. These matrices are conceptually thought of as a rotation matrix but it includes stretching and shearing, hence, $Det(R) \neq 1$. In addition the cross-correlation between the orthogonal canonical components r_{X_1,Y_2}, r_{X_1,X_2}, r_{Y_1,Y_2}... is zero, which is to say the covariance and cross-covariances matrices

for the rotated datasets are all diagonal. Determining the canonical cross-correlation coefficients and the rotation matrices involves finding the eigenvalues and eigenvectors for the following matrices: $\mathbf{C_X} = \mathbf{\sum_{XX}^{-1} \sum_{XY} \sum_{YY}^{-1} \sum_{YX}}$ and $\mathbf{C_Y} = \mathbf{\sum_{YY}^{-1} \sum_{YX} \sum_{XX}^{-1} \sum_{XY}}$ by solving the equations below

$$(\mathbf{C_X} - \lambda_{X_i}\mathbf{I})\,\mathbf{a_{X_i}} = 0 \tag{2.3}$$

and

$$(\mathbf{C_Y} - \lambda_{Y_i}\mathbf{I})\,\mathbf{a_{Y_i}} = 0 \tag{2.4}$$

where covariance matrices $\sum_{XX}$, $\sum_{YY}$ and cross-covariance matrices $\sum_{XY}$ and $\sum_{YX}$ are defined as $\sum_{XY} =$,

$$\begin{pmatrix} E[(X_1(t)-\mu_{X_1})(Y_1(t)-\mu_{Y_1})] & E[(X_1(t)-\mu_{X_1})(Y_2(t)-\mu_{Y_2})] & E[(X_1(t)-\mu_{X_1})(Y_3(t)-\mu_{Y_3})] \\ E[(X_2(t)-\mu_{X_2})(Y_1(t)-\mu_{Y_1})] & E[(X_2(t)-\mu_{X_2})(Y_2(t)-\mu_{Y_2})] & E[(X_2(t)-\mu_{X_2})(Y_3(t)-\mu_{Y_3})] \\ E[(X_3(t)-\mu_{X_3})(Y_1(t)-\mu_{Y_1})] & E[(X_3(t)-\mu_{X_3})(Y_2(t)-\mu_{Y_2})] & E[(X_3(t)-\mu_{X_3})(Y_3(t)-\mu_{Y_3})] \end{pmatrix},$$

with similar definitions for $\sum_{XX}$, $\sum_{YY}$ and $\sum_{YX}$. Above μ_X is the expectation value of X, $E[X] = \mu_X$. The eigenvalues relate to the cross-correlation coefficients for the canonical components, $\lambda_{X_i'} = r^2_{X_i'Y_i'}$, $\lambda_{Y_i'} = r^2_{Y_i'X_i'}$ and $\mathbf{a_{X_i'}}$ and $\mathbf{a_{Y_i'}}$, are the eigenvectors that form the rows of the rotation matrices $\mathbf{R_{X'}}$ and $\mathbf{R_{Y'}}$ respectively. The canonical correlation coefficients obey the relation $r_{Y_1'X_1'} \geq r_{Y_2'X_2'} \geq r_{Y_3'X_3'}$.

To identify connections in the network we only use the first canonical component of our rotated dataset. Other information such as the relative contribution of each of the original components to the respective canonical components may hold useful information, however, using this goes beyond the scope of what we wish to accomplish. Unlike Pearson correlation, which allows

for anti-correlation, canonical coefficients can only take values $0 \leq r_{Y_i' X_i'} \leq 1$. In effect, any anti-correlated variations are rotated into positive correlations.

We use canonical correlation between the windowed (the length of which depends on the aims of the analysis) segments of pairs of vector magnetometer time series to quantify similarity between pairs of stations as a function of time. The time-series are de-trended with a linear fit within each correlation window. We calculate the canonical correlation between the i^{th} and j^{th} station for all possible station pairs to form a cross-correlation matrix (or weighted network), $C_{ij}(t)$. $C_{ij}(t)$ contains the correlation coefficient for the first canonical component for each station pair and each windowed segment.

The C_{ij} matrix could be used as a weighted adjacency matrix for the network instead of a binary adjacency matrix. However, many of the C_{ij} values are a result of "random correlation" and do not constitute physically related measurements, that is, it is dominated by noise. A "random correlation" here means obtaining a correlation coefficient from a pair of time series that is likely to of occurred by chance (based on a presupposed statistical significance). We outline how we determine the false positive rate in section 2.4.3. By using a threshold C_T we can obtain a binary adjacency matrix A_{ij} which, given an appropriate choice for C_T, will contain less noise.

2.4 Determining Correlation Thresholds

When choosing a correlation threshold for the weighted adjacency matrix there is a balance between minimising the number of false positives and false negatives in the resulting A_{ij} matrix while maximising the number of true positives. The likelihood of obtaining a false positive or negative under a threshold

C_T depends on the probability distribution of correlation coefficients obtained from noise surrogates. The resulting distribution strongly depends on the statistical characteristics of a given vector times series pair. Figure 2.2 shows the probability distribution of correlation coefficients for generated $1/f^{\alpha}$ noise of differing exponents $\alpha = 0, 1, 2$. Also shown is the $\alpha = 2$ noise signal with a linear de-trend within each window segment. The larger the exponent α the more the probability distribution is shifted towards higher correlation values; additionally the de-trended signal has a lower average correlation compared to its non-detrended counterpart. If the magnetometer time-series were to be modelled as noise they would typically have an α between 1 and 2 [Jackel et al., 2001]; since the magnetic field time-series is highly non-stationary the exponent associated with a particular station varies throughout the day, season, year, and solar cycle. Additionally the local properties of stations differ (see section 2.2).

2.4.1 Approaches in Climate Network Construction

A single threshold C_T is likely to be inadequate due to the differing characteristics of the magnetometer stations and the statistical properties of each pair ij. Instead a pair specific threshold $C_{T_{ij}}$ is required. To obtain this rigorously, a statistical significance level would be chosen. A large number of noise surrogates would then be generated for each respective signal segment pair to obtain a distribution of random correlations. The distribution of correlation coefficients could then be used to inform on the statistical significance of each $C_{ij}(t)$ therefore, the choice of threshold $C_{T_{ij}}$ specific to that pair. This is not feasible here due to the typical number of station pairs ~ 10000, the number

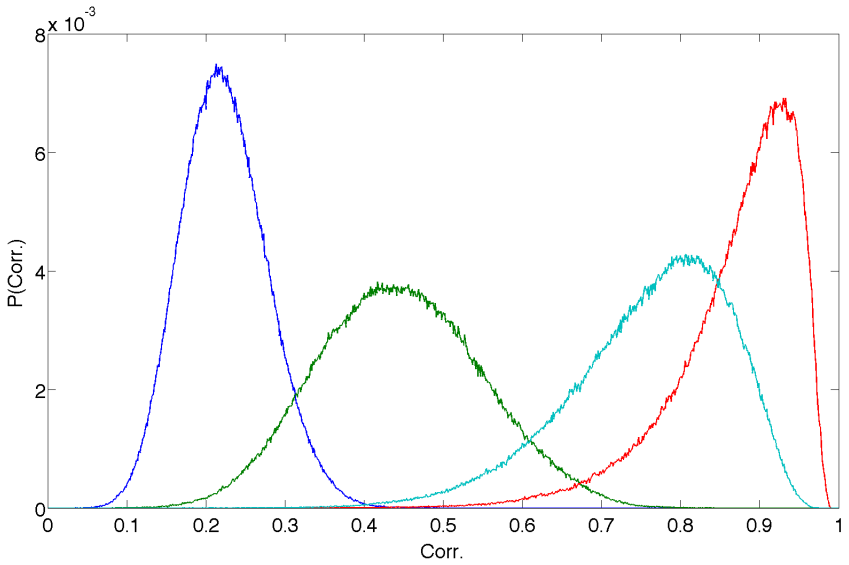

Figure 2.2: The correlation coefficient distributions for different generated $1/f^{\alpha}$ noise. Plotted are the distribution for $\alpha = 0$ (white noise) in blue, $\alpha = 1$ (pink noise) in green and $\alpha = 2$ (red noise) in red. Also plotted in is the generated $\alpha = 2$ noise that has had a linear de-trend applied before cross-correlation in light blue.

of windowed segments typically used $\sim$ 1000000s (for large aggregate studies) and the number of noise surrogates required to obtain a good distribution $\sim$ 1000 giving 10^{13} canonical correlation calculations.

Another approach taken in climate network construction is to require a fixed number of connections in the network at all times [Radebach et al., 2013]. This means that threshold C_T varies such that the strongest $x\%$ of the network is connected. This approach is unsuitable for this study; in substorms and ionospheric convection we wish to observe the growth and decay of spatial-temporal correlation times where through the globally coherent evolution of the system. A fixed number of connections tends to lead to short range clustering. Figure 2.3 shows the average correlation coefficient for station pairs is inversely related to distance; it is clear from the figure that short range pairs would likely dominate the network.

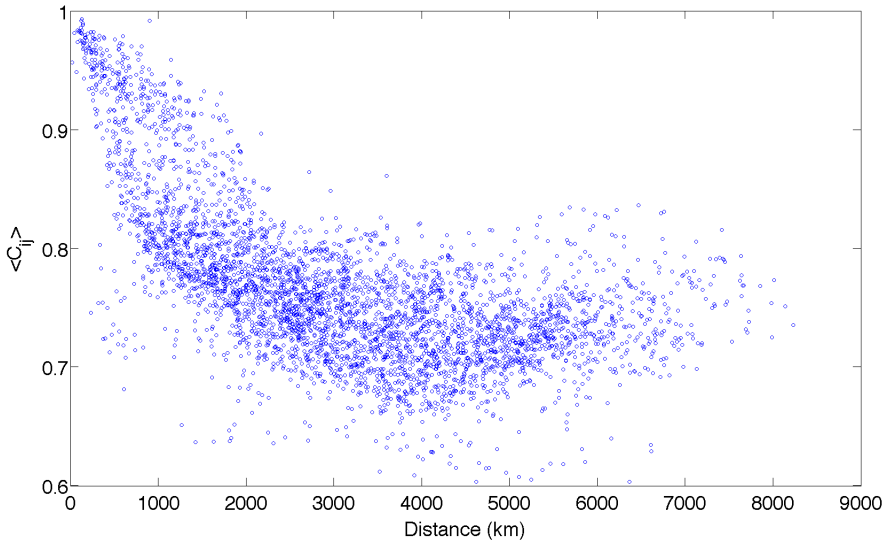

Figure 2.3: The average correlation as a function of separation distance for all station pairs in the northern hemisphere.

2.4.2 Our Approach

Given the above we take a more heuristic approach to determining an appropriate $C_{T_{ij}}(t)$ threshold matrix. First we apply a range of single global threshold C_T to $C_{ij}(t)$ to obtain set of single threshold networks

$$G_{ij}\left(t, C_T\right) = \Theta\left(C_{ij}(t) - C_T\right), \tag{2.5}$$

where Θ is the Heaviside step function ($\Theta(x) = 0$ if $x < 0$ and $\Theta(x) = 1$ otherwise). G_{ij} is not the final form of the network. We then determine the average normalised degree for the month centred on on the time t,

$$n_i(t, C_T) = \frac{1}{m} \sum_{t'=t-m/2}^{t+m/2} \sum_{i \neq j}^{N} \frac{G_{ij}(t', C_T)}{N-1}, \tag{2.6}$$

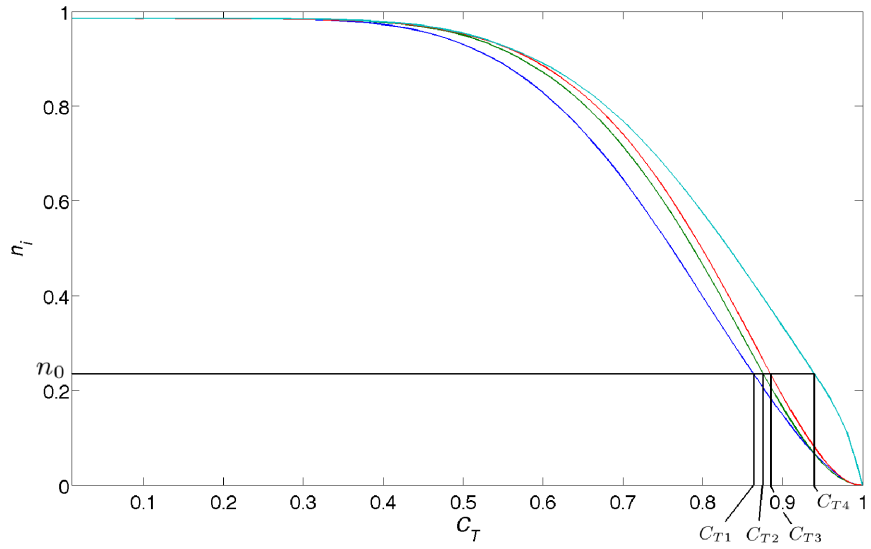

Figure 2.4: The monthly averaged normalised degree for representative stations is plotted as a function of the global threshold, C_T. A given normalised degree for the network, n_0, gives a a corresponding threshold for each station, C_{Ti}. Reproduced from Dods et al. [2015]

where N is the number of stations, and m is the number of minutes in a 30 day block of time. At any time t the normalised degree can be expressed as a function of global threshold C_T. To illustrate this, we plot the normalised degree as a function of C_T for a select few stations in figure 2.4. We can then chose a fixed average monthly normalised degree n_0. Associated with this normalised degree are thresholds C_{T_i} for each station that gives the same fixed degree n_0 (when averaged over one month). For each station pair ij there are two associated thresholds, C_{Ti} and C_{Tj}. The stations are considered connected if the lower threshold of the two is satisfied, $C_{T_{ij}} = min[C_{T_i}, C_{T_j}]$. Importantly, there is no fixed number of connection at particular points in time

Our justification for this approach is that if there were no differences between geographic locations and equipment of stations then each should have

the same monthly averaged degree. This is reasonable as the stations rotate through MLT, so while there is definite physical significance to certain MLT regions that will affect the correlation there should be no uniqueness for the station itself and its geographical location. Given this, if we average over a long enough period of time (but not too long as to be affected by some of the long time-scale non-stationary aspects of the magnetospheric/ionospheric system) any differences between the normalised degree is a result of the specifics of that station/geographical region that affect the average correlation. Therefore by selecting for station thresholds we seek to limits the influence on station/geographical effects.

In figure 2.5 we show two examples of the average degree for one month shown as deviations from the global average degree,

$$\Delta n_i = |n_i - \frac{1}{N}\sum_{i}^{N} n_i|. \tag{2.7}$$

This is shown for a network derived from a single threshold $C_T = 0.97$ (a) and from a fixed monthly degree network $n_0 = 0.075$ (b). We chose a $C_T = 0.97$ for the single threshold network such that the global average degree for the network is the same in both examples for comparison. As expected, the deviations from the monthly average normalised degree are larger for the network formed from a single threshold (figure 2.5(a)) compared to the fixed normalised degree networks (figure 2.5(b)).

2.4.3 Statistical Significance

We now quantify the average likelihood that a connection between a station pair could occur by chance (a "false positive"). To quantify the likelihood

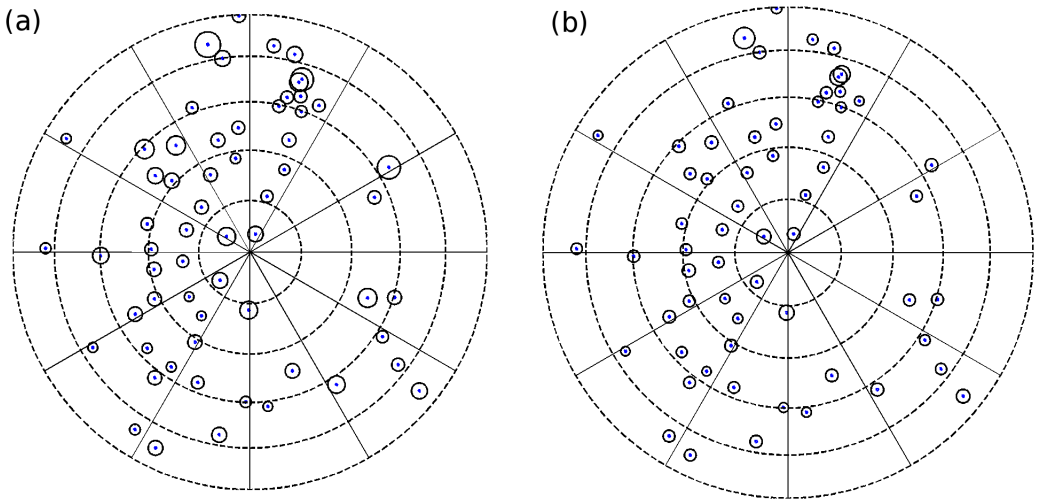

Figure 2.5: Displays the deviations from the monthly averaged normalised degree maps for a network derived using a single threshold $C_T = 0.97$ (a) and using a fixed normalised degree $n_0 = 0.075$ (b); the radius of the black circles denotes the magnitude of the deviations from the normalised normalised degree for each given station.

of false positives, we construct ten noise surrogate datasets as follows. For each noise surrogate dataset, each time windowed segment of the signal for all stations is Fourier transformed. The phases are then randomised leaving the power spectrum amplitude unchanged and the resulting signal is then inverse transformed. The same process for forming the network that we apply to the observations is then applied to the surrogate data to obtain an estimate for the number of false positives:

$$F(t) = \frac{\sum_{i}^{N}\sum_{j}^{N} f_{ij}}{N^2 - N}, \tag{2.8}$$

where N is the number of stations, f_{ij} is the surrogate network and F is the normalised total number of connections in the network (i.e. false connections). Ten of these surrogate networks, f_{ij}, are formed and the normalised total num-

ber of connections (summed over the surrogate network), F, for each surrogate network are calculated. These ten surrogate values of the (normalised) total number of false connections can then be averaged to give an estimate of the network false positive number. With this we have no information on the likelihood of individual pairs being falsely connected but only the average across the $N(N-1)$ station pairs.

2.4.4 Summary

Our approach to constructing the network from the raw time-series data to the intermediate station network is summarised in a few key steps which are visually represented in figure 2.6.

Step 1. A running window is applied to the raw vector time series and the data is de-trended in each window with a linear fit. Linear trends on the window timescale are removed so that their effect on the resultant cross-correlation is small.

Step 2. Canonical correlation [Brillinger, 1975] between the windowed segments of pairs of vector magnetometer time series is used to quantify similarity between pairs of stations as a function of time. The first canonical coefficients between the i^{th} and j^{th} station for all possible station pairs is used to form a cross-correlation matrix (or weighted network), $C_{ij}(t)$.

Step 3. Next we threshold $C_{ij}(t)$ to obtain the adjacency matrix $A_{ij}(t)$, which is zero (no connection) or one (connection) for a given pair of stations ij. The threshold C_{Tij} in principle has a different value for each pair of stations in the network. To determine C_{Tij} we construct a standardised adjacency matrix such that all stations, on a long timescale (here, 1 month) have close

to the same average degree (or likelihood to be connected to the network). We standardise our adjacency matrix by finding the threshold C_{Ti} for each station that gives the same fixed degree n_0 (when averaged over one month). The station dependent thresholds, used to obtain the time dependent adjacency matrix, are then $C_{Tij} = min[C_{Ti}, C_{Tj}]$.

Step 4. Once the network is constructed we calculate time dependent dimensionless parameters that describe the spatial distribution and extent of the correlated behaviour. These are then used to characterise the system.

2.5 Regular Grid Mapping Scheme

In sections 2.2 - 2.4 the method for forming a network based directly on the magnetometer stations was described. There are several problems with using such a network. Firstly, the spatially inhomogeneous distribution of magnetometer stations can distort the resultant network properties [Bullock et al., 2010]. Secondly, there are large gaps in the station coverage of MLT-MLat, as a consequence it is difficult to estimate the impact of this lack of information on the analysis and to aggregate network information over many events. The latter is a problem common to all investigations of the global ionospheric/magnetospheric response using only magnetometer stations.

The problems can be approached in two ways. When looking at a series of events we can only compare those that have similar station configurations. All distortions caused by inhomogeneity and missing information will affect the network in similar ways. This is the approach we take in chapter 3 where we analyse a small number of carefully selected substorm events. Alternatively, we can map the network information on to a regular grid, removing the

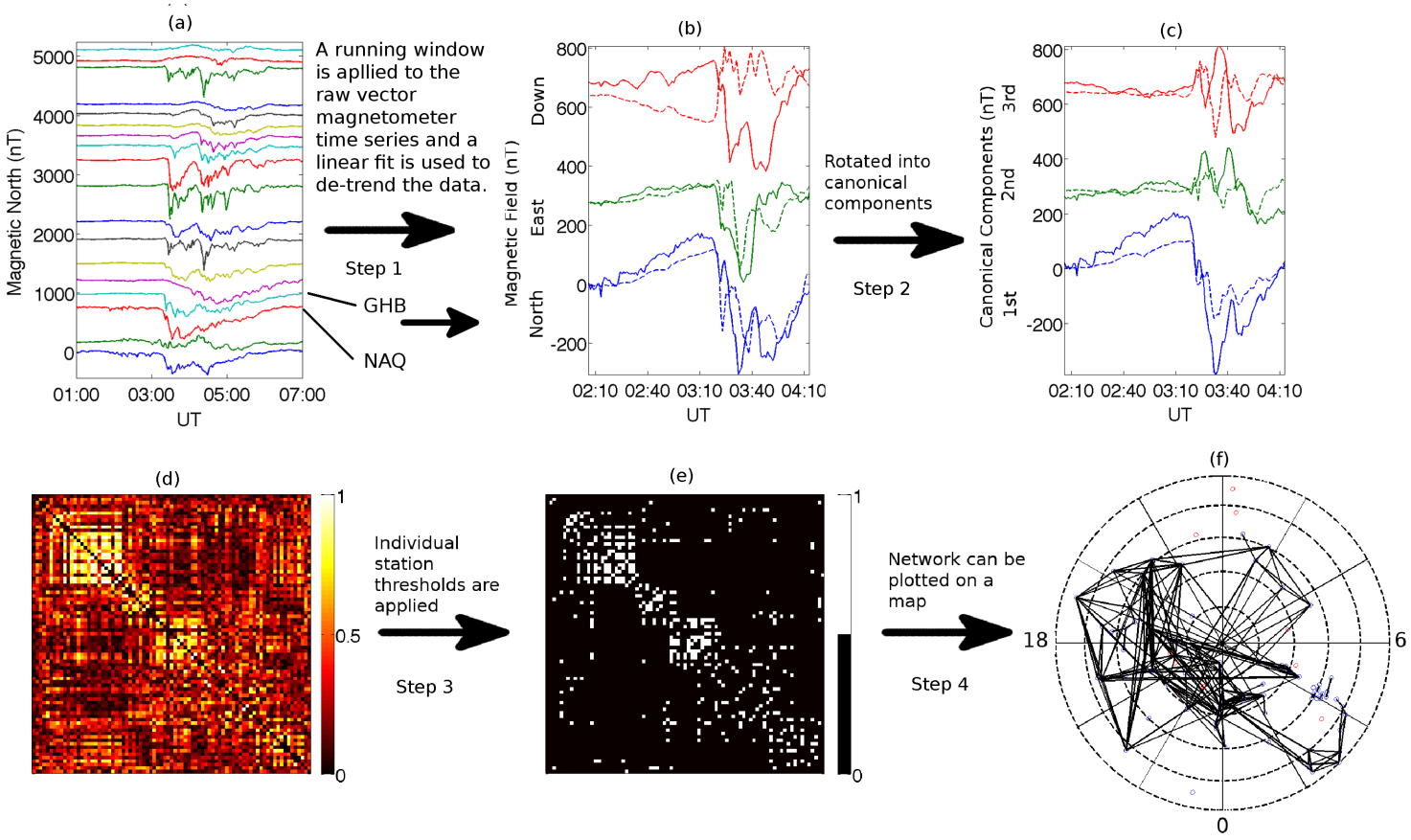

Figure 2.6: An illustration of the process of identifying connections in the network, these steps are outlined in sections 2.3 to 2.4.2. (a) Stack plot of magnetic north time series for stations centred around magnetic midnight during the substorm. The time series are ordered by magnetic latitude. (b) A comparison of a 128 minute segment of the north (blue), east (green) and down(z)(red) component of the magnetic field for two stations, GHB (dashed) and NAQ (solid). A linear fit has been used to detrend the data within the window. (c) Canonical correlation is used to form new rotated components that maximises the correlation in the 1st canonical component for this time window. The rotation is unique for each station pair and time window. Correlation between different canonical components is zero as both the cross and auto-covariance for the canonical components matrices are diagonal. (d) The canonical-correlation process is repeated for all station pairs and a correlation matrix, C_{ij}, can be formed. The matrix contains the correlation coefficients for the 1st canonical component. (e) Station dependent thresholds are applied to C_{ij} to form the adjacency matrix A_{ij}. The white squares indicate a connected station pair. Connections can be visualised on a MLat-MLT map. (f) The magnetic north down view of the northern hemisphere, the blue circles indicate active stations and the red circles are stations for which there is no data at this time. The dashed lines are contours in MLat, at 50°, 58°, 66°, 74° and 82°. Reproduced from Dods et al. [2015]

inhomogeneity issue. The grid cells would then be the nodes of the network. In addition, the regular grid network allows us to aggregate network information over many events in a consistent way. This allows for an aggregate network to describe the average global response of the system. This is the approach we take when investigating the aggregate network response to quiet time substorms and the aggregate network response to step-like changes in the the solar wind.

2.5.1 Choosing an Optimal Grid

When optimising a grid to map the network there are two main choices to make; first, the type of grid to use and second, the grid spacing or number of grid cells to use. Figure 2.7 shows two possible grid types, (a) is a regular grid in MLT-MLat where the cells are equally spaced in degrees and (b) is pseudo-geodesic grid made from a tessellating a sphere with triangles. The pseudo-geodesic grid has close to equal physical spacing between the cells, and does not suffer from oversampling at the poles as does the regular grid. In addition the areas are of almost equal size. These properties are important in a traditional network context as non-uniformly sized grids that have different physical areas are known to produced distortions in local network properties of the grid nodes [Heitzig et al., 2012]. However, the geodesic grid is unsuitable for our purposes. The magnetometer stations themselves also move through MLT within a finite window of time and as such their measurements are already spatially smeared by different degrees. It therefore makes sense in this context to have cells that are large at lower latitude, hence, we choose to use the regular grid.

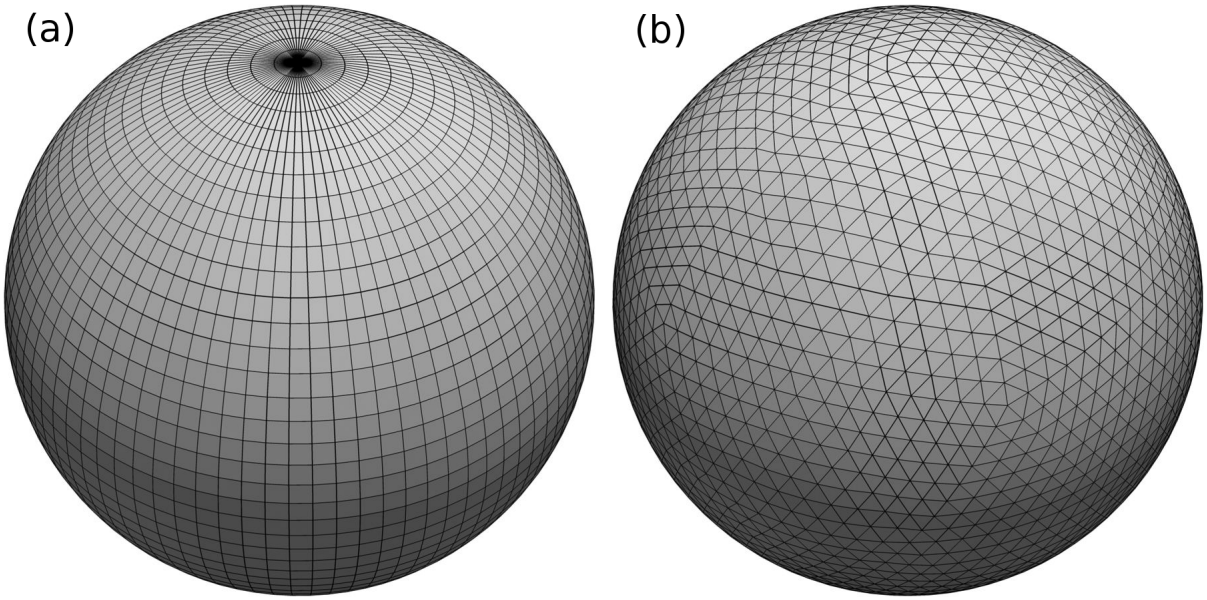

Figure 2.7: (a) Shows a regular grid in latitude and longitude and (b) a pseudo-geodesic grid made from tessellating a sphere with triangles. Reproduced from Ballard et al. [2016]

Ideally the grid spacing should be chosen based on the spatial resolution of the data. Alternatively posed, at what point are observations at positions x and $x + \Delta x$ distinct. In the context of the ionosphere/magnetosphere system, there is no time stationary spatial scale. In addition, magnetic field measurement are a response to the sum of currents for the entire system, as such, they are integrations over space. The time window used for the correlation inherently provides a natural spatial scale in MLT, that is, the grid spacing should not be less than the size of the correlation window. The choice of grid is also restricted by the distribution of magnetometer stations throughout MLT-MLat. If the grid cells are too small there may be grid node pairs that are never observed at any point in time leading to "holes" in the grid network.

Given the above we choose to use a regular grid in MLT and MLat. The grid sizes we use are 2 hours in MLT and 8° in MLat. Our grid extends from

50° to 82° and covers the entirety of MLT. We do not extend the grid to 90° as there are not enough stations at very high latitudes and the cell sizes are too small. We found the chosen spacing gives close to the smallest grid size that has no unobserved grid cell pairs. The 2 hour MLT is the largest correlation window size we use in this thesis.

2.5.2 Mapping the Network on to a Regular Grid

Here we describe the scheme for mapping the station correlation networks T_{ij} (note the change in notation from $A_{ij} \rightarrow T_{ij}$) onto a fixed regular grid in MLT-MLat. Our mapping method follows a modified form of the cloud-in-cell (CIC) algorithm [Hockney and Eastwood, 1988]. We outlined the steps below and illustrate them in figure 2.8.

- Each station, i, is assigned an area of influence (the blue bordered box in figure 2.8). The area is the same size, in degrees, as the grid cells and is centred on the station's location. The grid cells that overlap with the station's area of influence constitute the cells for which the network information will be interpolated to.

- The weights for each cell node, resulting from their nearby stations, are based on the percentage area overlap of the cell with each station. They are calculated as follows:

$$w_{ki}(t) = (1-\frac{\delta\phi_{ki}(t)}{\Delta\phi})(1-\frac{\delta\theta_{ki}(t)}{\Delta\theta})\Theta(\Delta\phi-\delta\phi_{ki}(t))\Theta(\Delta\theta-\delta\theta_{ki}(t)), \quad (2.9)$$

  where w_{ki} represents the weight for grid node k resulting from station i, $\delta\phi_{ki}$ and $\delta\theta_{ki}$ the longitudinal and latitudinal separation between i and k

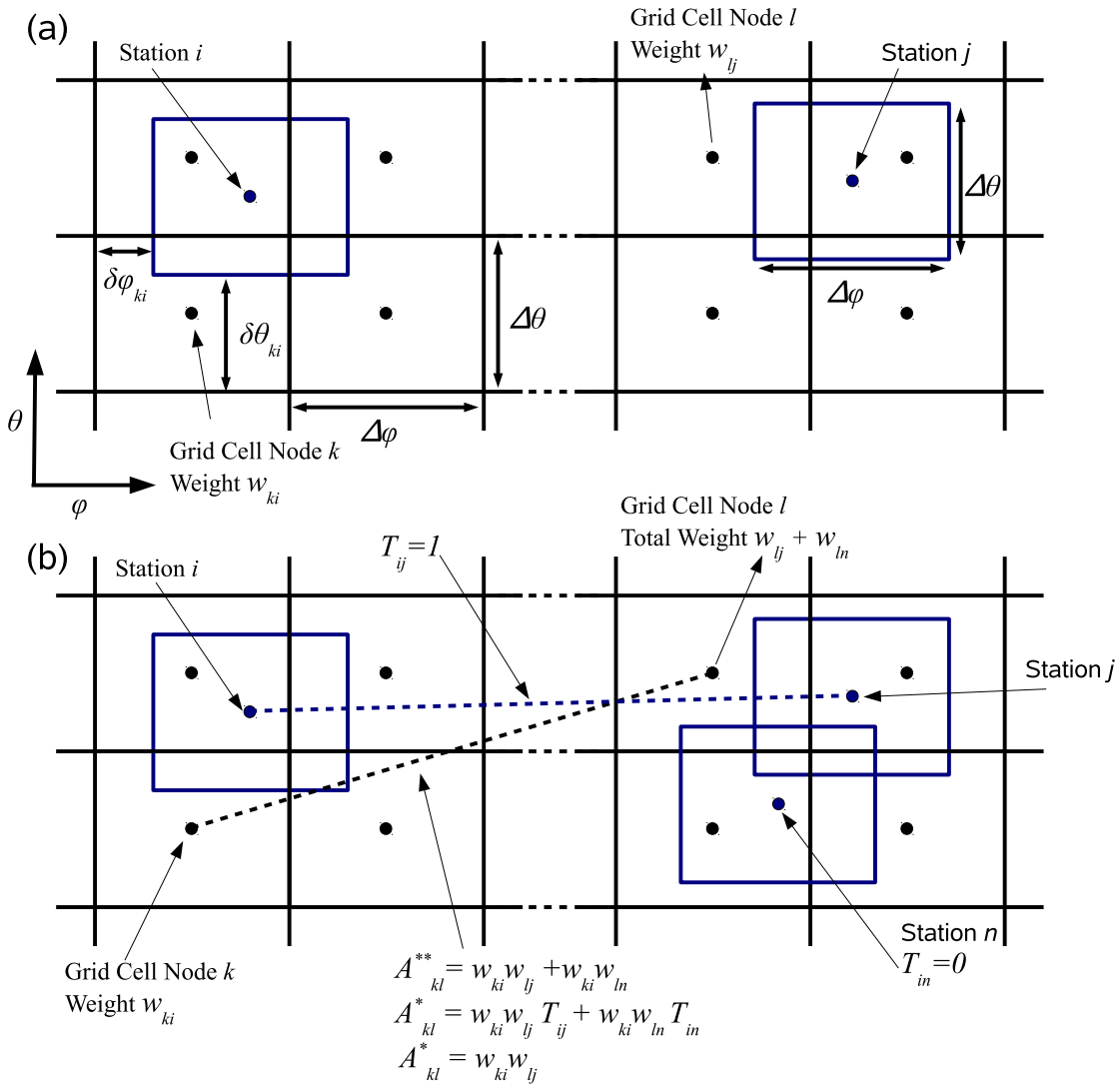

Figure 2.8: (a) shows a regular grid where the sizes of the grid cells, station areas of influence and the separation between station i and k in MLT and MLat, $\delta\phi$ and $\delta\theta$, are defined. (b) shows an example for calculating A^{**}_{kl} and A^{*}_{kl} given that there are only three neighbouring stations i, j and n. In this example stations i and j are connected and stations i and n are not connected, and as such A^{*}_{kl} receives no contributions from station pair i, n.

respectively. Θ is the heaviside step function (equal to 1 if greater than 0 and 0 otherwise). This ensures only the four closest nodes to station i are included in the sum. By construction $\sum_{k}^{N} w_{ki} = 1$ except at the edges of the grid domain, i.e. if $\Theta_i < 50 + \Delta\Theta$, where Θ_i is the latitudinal position of station i.

- We then form two matrices A^{**}_{kl} and A^{*}_{kl}. A^{**}_{kl} is the maximum connectivity that could occur between grid cell pair k and l (conceptually this is the case when $A_{ij} = 1$ for all ij). A^{*}_{kl} is the level of correlation between two grid cell pairs k and l resulting from correlation between stations k and l. They are constructed as follows:

$$A^{*}_{kl}(t) = \sum_{i \neq j}^{N_s} \sum_{j \neq i}^{N_s} w_{ki}(t) w_{lj}(t) T_{ij}(t) \tag{2.10}$$

and

$$A^{**}_{kl}(t) = \sum_{i \neq j}^{N_s} \sum_{j \neq i}^{N_s} w_{ki}(t) w_{lj}(t), \tag{2.11}$$

where N_s is the number of stations. Both $A^{*}_{kl}(t)$ and $A^{**}_{kl}(t)$ are functions of time. Figure 2.8(b) shows an example for one grid node pair kl and three contributing stations. The station pair connection $A_{ij} = 1$ is shown with a blue dashed line and the calculated weights for grid node cell pair connection A^{*}_{kl} and A^{**}_{kl} are shown in black.

A^{*}_{kl} and A^{**}_{kl} are then used to create descriptive parameters of the spatial topology of the connected network. The adjacency matrix is then

$$A_{kl}(t) = \frac{A^{*}_{kl}(t)}{A^{**}_{kl}(t)}. \tag{2.12}$$

A_{kl} can then take values between 0 and 1, if $A_{kl} = 0$ then there are no network connections between grid cell pair k, l for any of the observing stations, and if $A_{kl} = 1$ there is always a connection between grid cell pair k, l.

Chapter 3

Dynamical Network Analysis Applied to Test Case Substorms

The majority of the work in this chapter is formed from a paper submitted and accepted to the journal of geophysical research [Dods et al., 2015].

Substorms are an extensively studied phenomena in geophysics and whilst there is an overall established substorm cycle [McPherron et al., 1973], there is considerable variation in the specific detailed sequence of events Akasofu [2004]; Meng and Liou [2004] (see chapter 1.5.1). The ability to quantify substorm dynamics in an automated manner would be a valuable tool to determine what initial conditions, in terms of the internal state of the magnetosphere-ionosphere system and energy loading by the solar wind, produce a given detailed response. Attempts have been made at a classification of substorms based on images of the aurora Syrjasuo et al. [2007]; where training algorithms were used to identify a wide range of arc shapes that can be present during a substorm. AE indices have also been used to identify substorm behaviour [Gjerloev et al., 2004], although such descriptions are limited by the

scalar and spatially aggregating nature of the AE indices.

Ground based magnetometer stations detect the variation in the local magnetic field resulting from time dependent current systems in the ionosphere and serve as a proxy for dynamics occurring in the magnetosphere. There are typically $\sim$ 100 magnetometer stations available to observe any given substorm. The question is whether an algorithmic methodology can be developed to quantitatively characterise a substorm signature from these $\sim$ 100 time series in an automated manner. SuperMAG is a database that collates and processes all available ground based magnetometer vector time series into a standardised baselined format at 1min cadence [Gjerloev, 2012]. This provides an excellent starting point for studies attempting to characterise collective information from these stations. Here we investigate whether canonical correlation between the vector time series of pairs of magnetometer stations can be used to construct a network that can characterise substorms. Correlation between stations has been examined previously, although only using a few contra-posed station pairs Jackel et al. [2001]. If the correlation between all $\sim$ 100 stations can be quantified in a robust and readily accessible manner then this would provide a tool for substorm identification and classification.

In this chapter we identify several dimensionless network parameters that capture key aspects of the dynamics of the substorm. A brief overview of the chapter is as follows: In section 3.1 we introduce the dataset used here, and how the dimensionless network parameters that are used to describe the substorms are formed. In section 3.2 we apply this methodology to the four test case substorms as well as a SMC event and a day in which no substorms occur. We also explore the effect of different window sizes and cross-correlation lags on the network response to substorms. In section 3.3 we provide a cursory

look the the aggregate network response to 116 substorm events.

3.1 The Datasets Used in This Study

Four substorms are investigated and they were selected according to the criteria outlined in Gjerloev and Hoffman [2014]: temporal isolation, the substorms do not occur during a magnetic storm (|DST|<30nT), and they are of the classic bulge-type. They occur in the years 1997 and 1998 November-February. Winter months were chosen to limit sunlight on the dayside. The events are also selected such that there is a good distribution of stations in the night side at the onset of the substorm. Onset times for the substorms were determined to 1 min precision using the Polar satellite's Visible Imaging System (VIS) and Earth Camera Gjerloev and Hoffman [2014]. Care was taken such that the onset brightening developed continuously into a substorm to eliminate pseudo-onsets Gjerloev and Hoffman [2014]. The substorm peak is also identified using Polar VIS images. The peak is a qualitative estimate of the combined intensity of the event and the westward and poleward expansion of the poleward auroral boundary Gjerloev and Hoffman [2014]. A quiet day and a steady magnetic convection event were also investigated. The quiet day is defined as a day in which no substorms have occurred. The SMC event chosen occurs on 10th Feburary 2008. This event was chosen due to a good distribution of magnetometer stations in the nightside at the start of the event.

3.1.1 Network Parameters

Once the threshold for each station pair, C_{Tij}, is determined as above, we can obtain the adjacency matrix:

$$A_{ij}(t) = \Phi[|C_{ij}(t)| - C_{Tij}] \tag{3.1}$$

so that $A_{ij} = 1$ if station i is connected to station j and is zero otherwise and Φ is the Heaviside step function. All diagonal elements (self connections) of A_{ij} are set to zero and in an undirected network the matrix is symmetric, as in the case for correlation calculated at zero lag. Once the dynamical network has been formed, network parameters can be used to quantify its evolution. Given $A_{ij}(t)$, time dependent global network parameters can be determined as follows:

1. **The normalised total number of connections**,

$$\alpha(t) = \frac{\sum_{i \neq j}^{N(t)} \sum_{j \neq i}^{N(t)} A_{ij}}{N(t)^2 - N(t)}, \tag{3.2}$$

   where $N(t)^2 - N(t)$ is the total number of possible connections in the network. $N(t)$ is the number of active stations taking data, which varies with time.

2. δ**, the average geodesic connection distance** (physical distance) in the network. Note that the average geodesic connection distance here is not the shortest path (or graph geodesic) between two stations [Newman, 2010]. A distance separation matrix, d_{ij}, is formed that is the geodesic distance separations between all stations. The average connection dis-

tance is then

$$\delta(t) = \frac{\sum_{i\neq j}^{N(t)} \sum_{j\neq i}^{N(t)} A_{ij} d_{ij} / (N(t)^2 - N(t))}{\sum_{i\neq j}^{N(t)} \sum_{j\neq i}^{N(t)} d_{ij}}, \tag{3.3}$$

which is normalised to the average connection distance if all stations were connected. Note, δ can be > 1.

3. **Θ_{kp} is the number of connections within, and between, two fixed latitudinal bands.** The lower latitude band extends from a lower bound, $L_l = 50°$ MLat (no station data below this latitude was used), to an upper bound U_l. U_l is defined as the upper edge of the auroral oval before onset of the substorm of interest at magnetic midnight. The position of the auroral oval is obtained via visual inspection of Polar VIS images and U_l is different for each event. The upper latitude band extends from the upper edge of the auroral oval, $L_u = U_l$, to $U_u = 90°$ MLat. If the latitudinal position of station i is θ_i then,

$$\Theta_{kp}(t) = \frac{\sum_{i\neq j}^{N(t)} \sum_{j\neq i}^{N(t)} A_{ij} \Phi[\theta_i - L_k] \Phi[U_k - \theta_i] \Phi[\theta_j - L_p] \Phi[U_p - \theta_j]}{\sum_{i\neq j}^{N(t)} \sum_{j\neq i}^{N(t)} \Phi[\theta_i - L_k] \Phi[U_k - \theta_i] \Phi[\theta_j - L_p] \Phi[U_p - \theta_j]}. \tag{3.4}$$

Where the subscripts k and p take all values of the indices for the lower and upper bands u and l. Θ_{uu} is then the normalised number of connections between stations in the upper band, Θ_{ul} the normalised number of connections between the stations in the upper band and stations in the lower band and Θ_{ll} the normalised number of connections between

stations in the lower band.

3.2 Results

We present results for dynamical networks calculated for four substorms over a 10-12 hour interval centred on the substorm onset. We also obtain the networks for a steady magnetic convection event and a "quiet" day (defined by a lack of substorms occurring). We obtain the networks according to the methods outlined in chapter 2. The dynamical networks and their parameters are obtained for a 128 minute running window with a 126 minute overlap; i.e. a new network is calculated every two minutes [1]. The main body of results here focus on canonical correlation networks at zero lag, therefore, the network parameters represent the near simultaneous response to correlated magnetic activity. A normalised degree for the network $n_0 = 0.05$ is chosen in order to reduce the number of false positives (spurious connections) in favour of allowing more false negatives (unidentified real connections). As a consequence the networks are formed from only the strongest connections in the system.

3.2.1 Network Response to Substorms

Figure 3.1 plots the time evolution of the network during four substorms. The network parameters are plotted as functions of the time of the leading edge of the correlation window for each realisation of the network. Therefore, when comparing with AE and $-v_x b_z$, a range of values equal to the window length must be considered. Both v_x and b_z are propagated solar wind parameters in

[1] The networks were calculated every 2 mins (instead of 1 mins) due to computational constraints

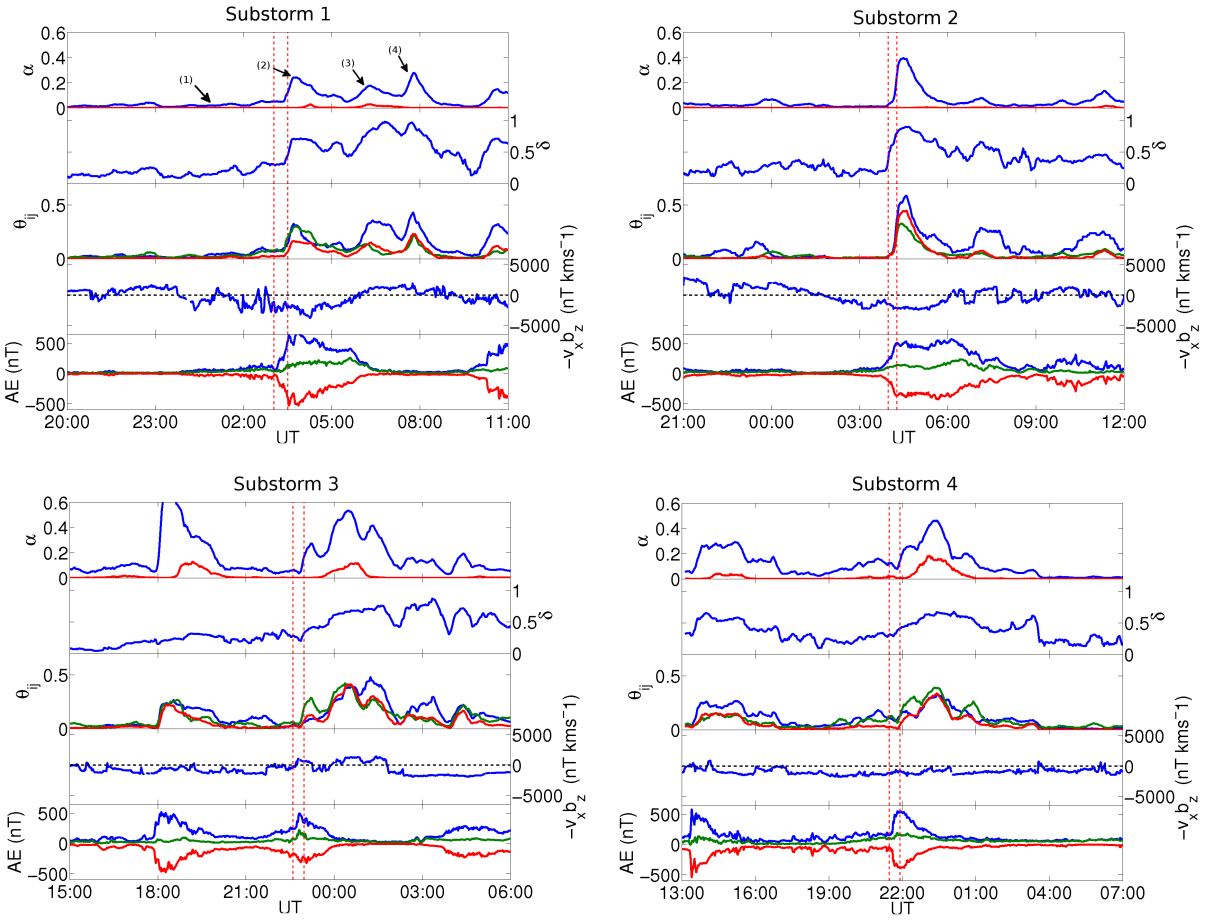

Figure 3.1: The time series of network parameters for four substorms: substorm 1 03:03 7th January 1997 (top left), substorm 2 04:01 6th November 1997 (top right), substorm 3 22:38 3rd November 1997 (bottom left) and substorm 4 21:29 16th December 1997 (bottom right). Each sub-figure is organised as follows, from top to bottom: (a) α (blue line), the normalised total number of connections, where the averaged total number of false connections is the red line. (b) δ, the normalised average connection distance in the network. (c) Θ_{ij}, the normalised number of connections between MLat band i and j. There are two MLat bands, the lower latitude band contains stations between MLat 50° (no data was used for stations below this point) and the upper edge of the auroral oval (at midnight just before onset) and the upper band between the upper edge and 86° MLat. The normalised number of connections within the lower band is the blue line, the normalised number of connections within the upper band is the green line and the normalised number of connections between the lower band and the upper band is the red line. (d) $-v_x b_z$, where v_x is the solar wind velocity along the earth sun line and b_z is the north-south component of the IMF. (e) Also plotted is AE (blue), AL(red), AU(green). The first vertical dashed red line indicates the onset time and the second indicates the peak of the substorm. The time of the peak of the substorm is a qualitative estimate based on POLAR satellite images (see section 3.1). The times (1) - (4) are highlighted in the top left panel (substorm 1). The network at these times are plotted in figure 3.2. Note, since the occurrence of false positives is independent of geodesic separation length and position, δ, on average will be 1 and the false connections are evenly distributed in the latitudinal bands.

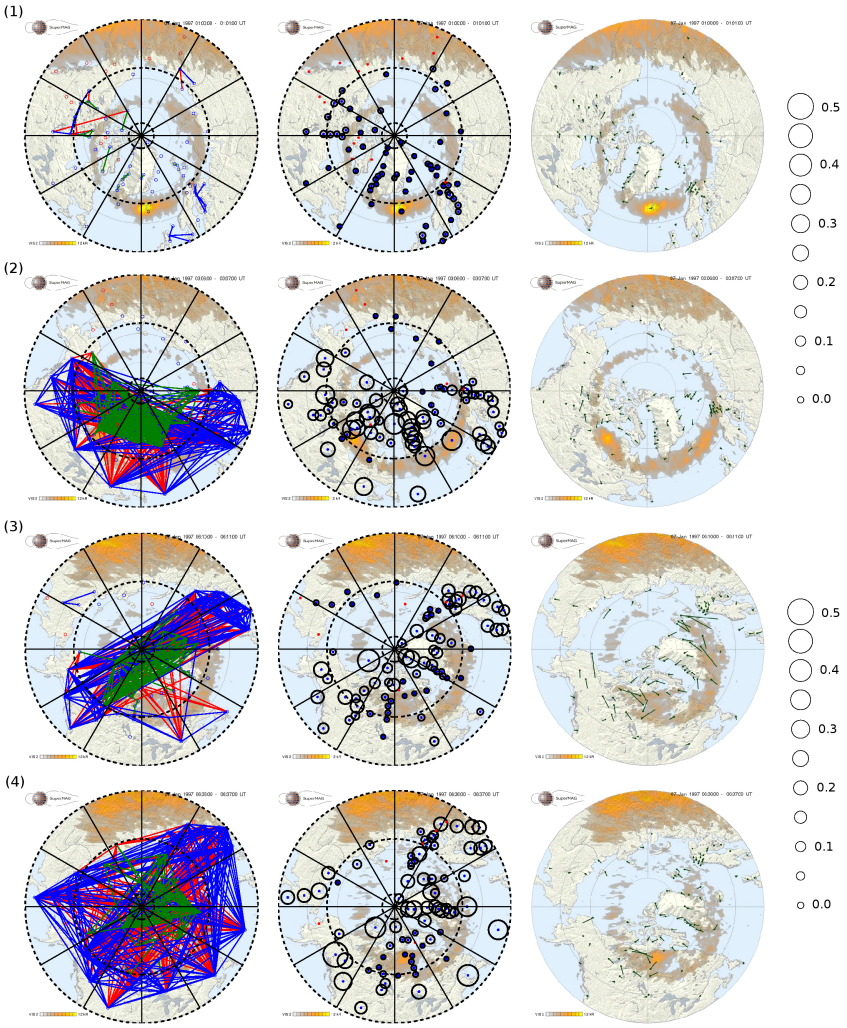

Figure 3.2: Left Column: Connection maps for several times during substorm 1, these times are labelled (1-4) in figure 3.1. The connections are colour coded as follows: connections between high latitude stations only (green) connections between low latitude stations only (blue) and connections between high and low latitude stations (red). The red circles are stations that are not active at that time. Centre column: displays normalised degree maps for the same times; the radius of the black circles denotes the normalised degree for each given station. Right column: Polar VIS data are also plotted for the same times. The station locations and VIS data, like the network parameters, correspond to the time at the leading edge of the correlation window. The exception to this is at time (4) where no VIS existed for the leading edge time so data from the central window time was used. The black dashed lines correspond to contours in MLat. The outer most contour corresponds to 50° MLat and the next highest corresponds to the boundary between low and high latitude stations, 68°. Magnetic midnight is at the bottom of each plot

Geocentric Solar Magnetospheric (GSM) coordinates and the data is obtained from the WIND satellite.

Substorms 1 and 2 are isolated events with IMF b_z turning southward 1-2 hours before onset. Both substorms have low connectivity in the network before the substorm onset, with any existing connections being short range (i.e. δ is small). There is a rapid increase in connectivity around onset, accompanied by an increase in δ above pre-onset levels for both substorms. Both substorms show an increase in high latitude connections, low and cross-latitudinal connections at onset. There is then a gradual decrease in the overall connectivity as the substorms enters the recovery phase. This phase is defined by the slow return of AL to pre-substorm levels. For substorm 1, δ does not decrease during this phase to pre-substorm levels and at the end of the substorm there is a resurgence of network activity dominated by low latitude connections. δ also reaches its maximum here. We associate this resurgence of activity with the later stages of the recovery phase of the substorm as the correlation window still encompasses a large portion of the recovery phase (the leading edge window time is plotted). Substorm 2 only shows a minor resurgence of activity at the end of the recovery phase consisting almost entirely of low latitude connections. δ does only returns to pre-substorm conditions after several hours.

Substorm 3, unlike the previous two substorms, has a substorm occurring 5 hours before the substorm of interest at 18:00 UT. Both substorm can be seen on the plot. IMF b_z remains negative following the end of the previous substorm. There is a strong network response to onset of the substorm, with α reaching 0.28 during the onset peak. At onset there is again a large number of high latitude connections indicated by Θ_{uu}. There is a second peak

in connectivity at the end of the recovery phase where alpha reaches 0.55, i.e. half of all available connections are present. These low latitude connections dominate here. δ also reaches maximum here after a slow ramp up during the substorm.

For substorm 4, b_z is southward well before the onset and AE is also in a perturbed state. There is a gradual increase in connectivity before the substorm onset with α reaching 0.22 here. The first peak around onset is dominated by high latitude connections. α continues to increase reaching a maximum of 0.4 during the recovery phase. This phase shows an increase in low latitude connections. δ also reaches maximum during the recovery phase after a slow ramp up during the substorm. The likelihood of false connections during this substorms is much higher than the other three substorms (for consistency the same normalised degree, n_0, for the network was chosen for all events). The onset peak, however, is largely free of false connections. Substorm 4 shows some activity in the network well before the substorm onset, although it is difficult to identify whether it is associated with this specific substorm or is indicative of unrelated activity.

The magnitude of the response in network parameters, for the test case substorms appears to be largely independent of the magnitude of peak AE during the substorms. This seems to indicate that the network is not simply tracking the magnitude of ongoing activity. Sustained AE $>$ 300nT is not necessarily associated with near simultaneous magnetic activity. This can be seen in substorms 1 and 2 where there is a clear drop-off in connectivity in the network post peak whilst AE remains high. This drop off in α cannot be seen as clearly in substorms 3 and 4 possibly due to the short recovery phase in comparison to substorm 1 and 2.

The networks can be visually represented; we show this for substorm 1 in figure 3.2. Figure 3.2 shows snapshots of the connection maps (left column), maps of the spatial normalised degree distribution (centre column), and Polar VIS data (right column) for times that are indicated in figure 3.1 (top left). The connection maps show that the 2 hours before onset (1) there is little connectivity in the network, and any existing connections are local. At the onset phase (2) the connection structure is comprised of highly concentrated connections at high latitude (the green connections) as well as significant cross-latitudinal connections (the red connections). The connections at this stage are situated around the onset brightening seen in the Polar VIS images. This is seen clearly in the degree maps, stations in the evening sector at high latitudes having large normalised degree. During the recovery phase (3) the correlated behaviour shifts to cross-connectivity between regions centred around 20 MLT and 8 MLT. At the end of the recovery phase (4) the network is at its most globally distributed, with significant connectivity between the day-side and the night-side. In general, stations with the highest normalised degree are found outside of the expanded auroral bulge region during the recovery phase substorm. However, one cannot directly compare a single snapshot of the auroral visible light emission to the network connection structure, which aggregates information from a two hour time window.

3.2.2 Network Response to Other Phenomena

To test the robustness of this approach we now apply the same methodology to both a "quiet day", defined here by a lack of substorms occurring and a steady magnetic convection event. The results are plotted in figure 3.3 where

the axes have the same scales and format as figure 3.1. The "quiet day" was selected at random and there were no constraints on the solar wind conditions. We can see that for the quiet day 3.3 (left) α does not exceed 0.04, which is significantly lower than that occurring during substorms and similarly δ does not exceed 0.35. There is little discernible network response to the brief step-like southward turnings of the IMF and the subsequent responses in AE.

For the SMC event, figure 3.3 (right), there is a gradual increase in α at the onset of the event. The increase in connectivity coincides with the increase in AE from ambient levels. α continues to increase and reaches a maximum of 0.11 at the end of the event, which is a factor of 3 less than seen during substorms. Throughout the event connections are dominated by cross-latitude and high latitude connections. δ is raised from typical background levels from the onset of the perturbations in AE and reaches a maximum of 0.55. During this event the night side sector was well represented by the station configuration, from figure 3.4 we can see that there is a comparable station configuration, and thus spatial sampling, to substorms 1 and 2.

To summarise, the typical signatures of isolated substorm activity are then:

- Few connections in the network before onset of substorm.
- The network exhibits a clear rapid response at onset indicated by an increase in connectivity, $\alpha > 0.22$. High latitude connections are a key feature of the onset peak, however, low and cross-latitudinal connections are also present.
- There is a switch from a high latitude dominated connection structure to a low latitude dominated connection structures during the later stages

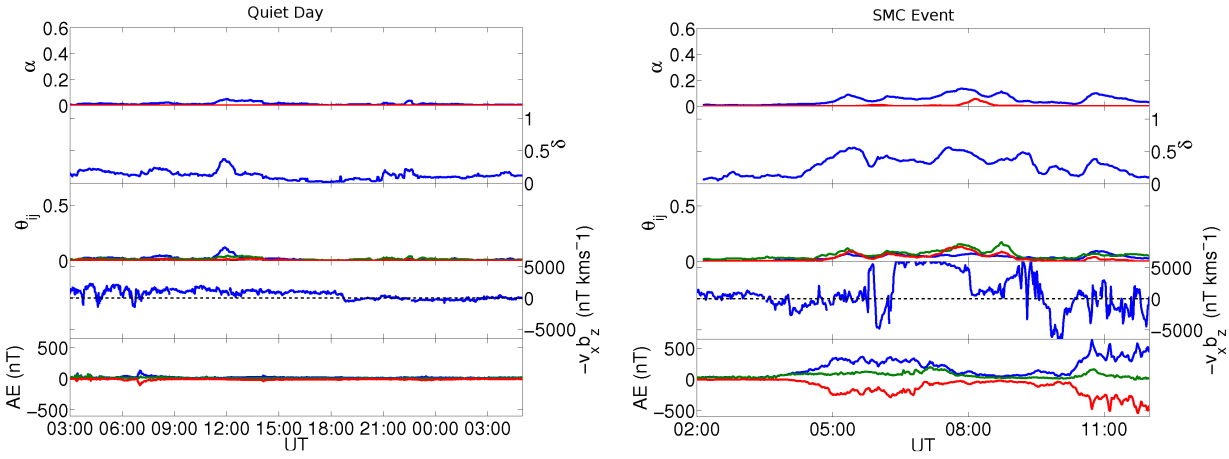

Figure 3.3: The time series of network parameters plotted in the same format as figure 3.1 for a quiet day (2nd February 1998 - 3rd February 1998) (left) and a SMC event (05:00 - 07:00 10th February 2008)(right). The axes scales are the same as in figure 3.1.

of the recovery phase. δ usually reaches maximum during the recovery phase.

- The maximum α and δ reached during the substorms is ≥ 0.32 and ≥ 0.7 respectively. In comparison, the maximum α and δ during the SMC event was 0.11 and 0.55 respectively. Similarly, for the quiet day, the maximum $\alpha = 0.04$ and $\delta = 0.35$.

- Post-substorm the network parameters return to their pre-substorm state, given there is no subsequent event shortly after the substorm.

Note that that the network parameter values depend on the choice of normalised degree, here $n_0 = 0.05$ (on average 5% of stations are connected). A consistent feature seen in all substorms is the progression from high latitude connection structures to a low latitude dominated connection structure as the substorm enters the recovery phase. From plots of the connection maps for substorm 1 (figure 3.2), the high latitude connections are co-located with

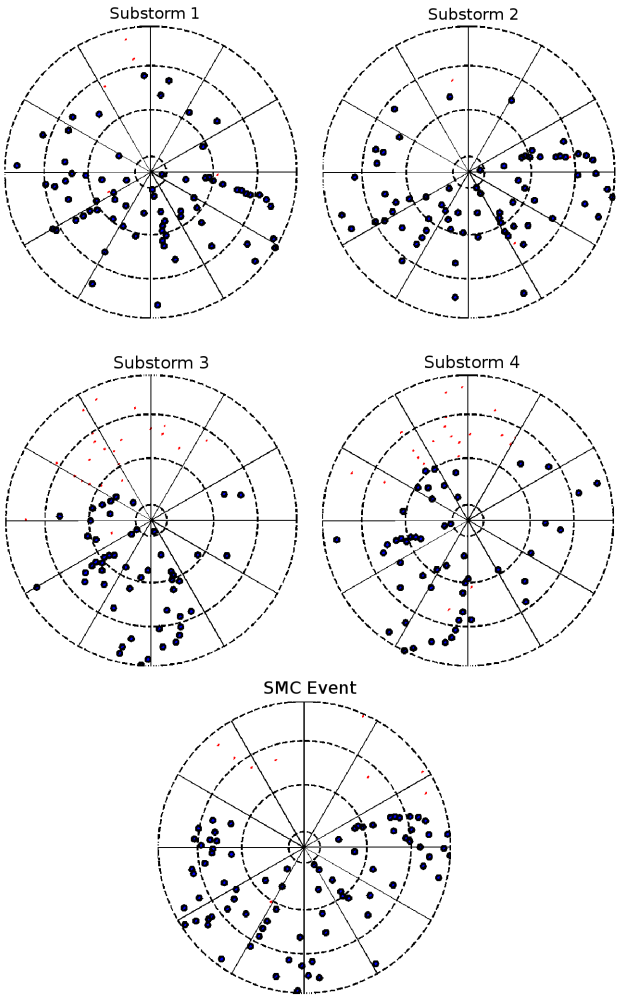

Figure 3.4: Station positions in MLT-MLat coordinates at the onset of substorms 1, 2, 3, 4 and the SMC event. Magnetic midnight is at the bottom of each plot.

the onset brightening. Therefore the first peak can be associated with the poleward leap and intensification of the auroral electrojet. The recovery phase of the substorm is traditionally associated with the relaxation the perturbed system back to it's ground state McPherron et al. [1973]. The movement of the closed field line structures in the magnetosphere (associated with latitudes below the auroral oval) during the relaxation to ground-state will produce associated currents in the magnetosphere. There are also a significant number of connections to stations in day-side sector during the end of the recovery phase. We interpret the large number of connections during the recovery phase as a clear indication that the substorm electrojet system is coherent on a global scale. If we apply the two-component electrojet concept (e.g. Kamide and Kokubun [1996]) this could be interpreted as the convection electrojet system is dominant and the substorm current wedge has ceased to play any significant role.

3.2.3 The Network Response to Substorms at 4 mins lag

Whilst quantifying near simultaneous magnetic activity was the main aim of the study, networks at lags up to 4 minutes were also investigated. The results from this, figure 3.5, show no new features in terms of α; the variations in α are, for the most part, the same, except that the magnitude is smaller. However, there is an increase in δ, the average connection length, when using longer lags. This indicates that the drop in the number of connections (smaller α) originates from a reduction in short ranged connections and a minor increase in the number of long range connections.

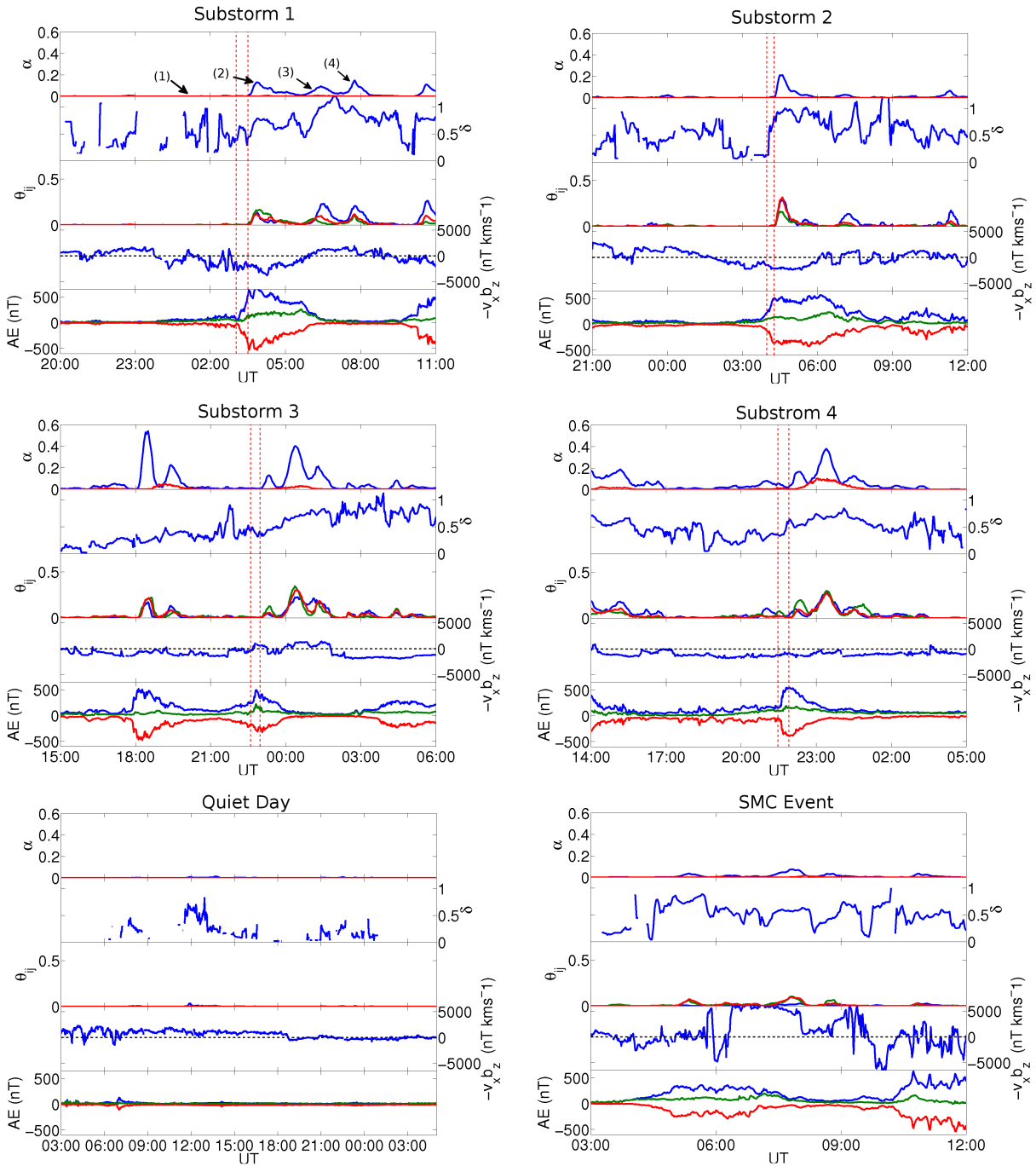

Figure 3.5: The time series of network parameters for all substorms, the SMC event and the quiet day. The networks were calculated using a 128 minute correlation window at a 4 minute lag. The figure has the same format and axis scaling as figure 3.1.

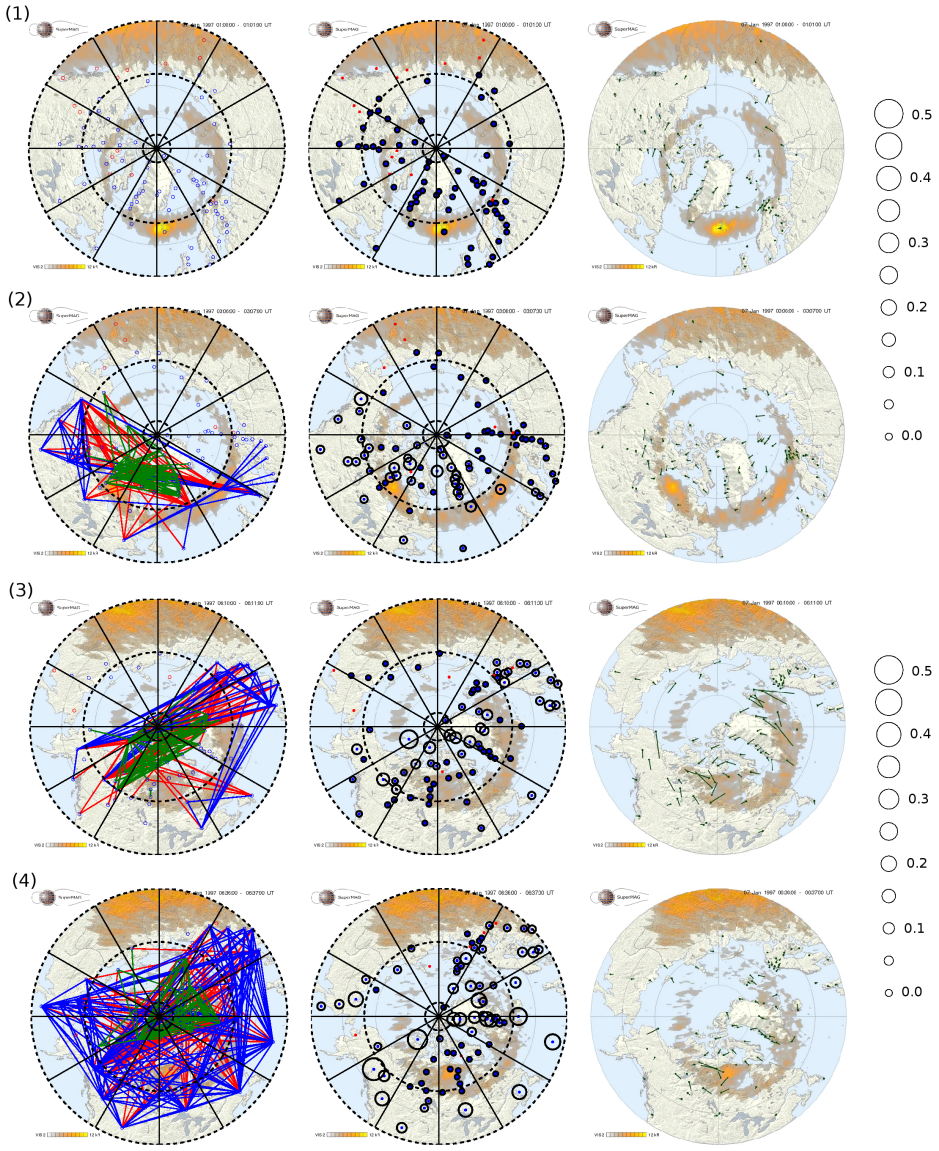

Figure 3.6: Connection maps, degree maps and VIS data in the same format as figure 3.2 for a 128 minute network at a 4 minute lag.

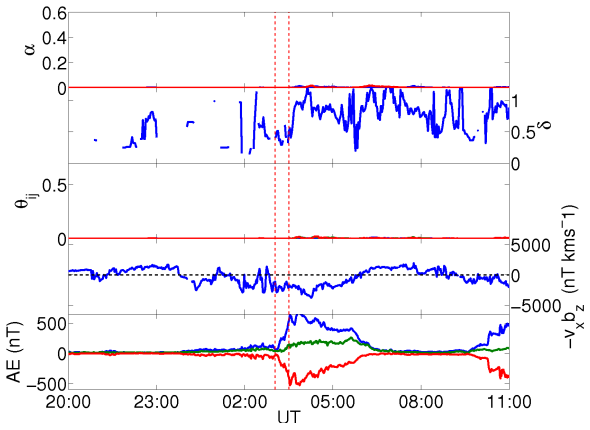

Figure 3.7: Network parameters describing the unique connections for the 4 minute lag network, $\mathbf{A}_4^*$, for substorm 1 03:03 7th January 1997. The figure has the same format and axis scaling as figure 3.1.

The differences can be explored by constructing a difference network that contains only the unique connections from the 4 minute lag network,

$$\mathbf{A}_4^* = \Phi(\mathbf{A_4} - \mathbf{A_0}), \tag{3.5}$$

where $\mathbf{A_0}$ and $\mathbf{A_4}$ are the networks at lag 0 and 4 minutes respectively. We do this for substorm 1, as shown in figure 3.7. The maximum $\alpha = 0.012$ for the difference network, that is <10% of connections that exist in the 4 minute lag network are unique to it.

3.2.4 The Network Response to Substorms using a 64 mins Correlation Window

The window length over which correlation is calculated needs to be optimised against (1) number of samples (longer windows are preferable) and (2) resolving the substorm dynamics (shorter windows are preferable). For the main body of results we use a 2 hour window; here we also repeat the analysis for

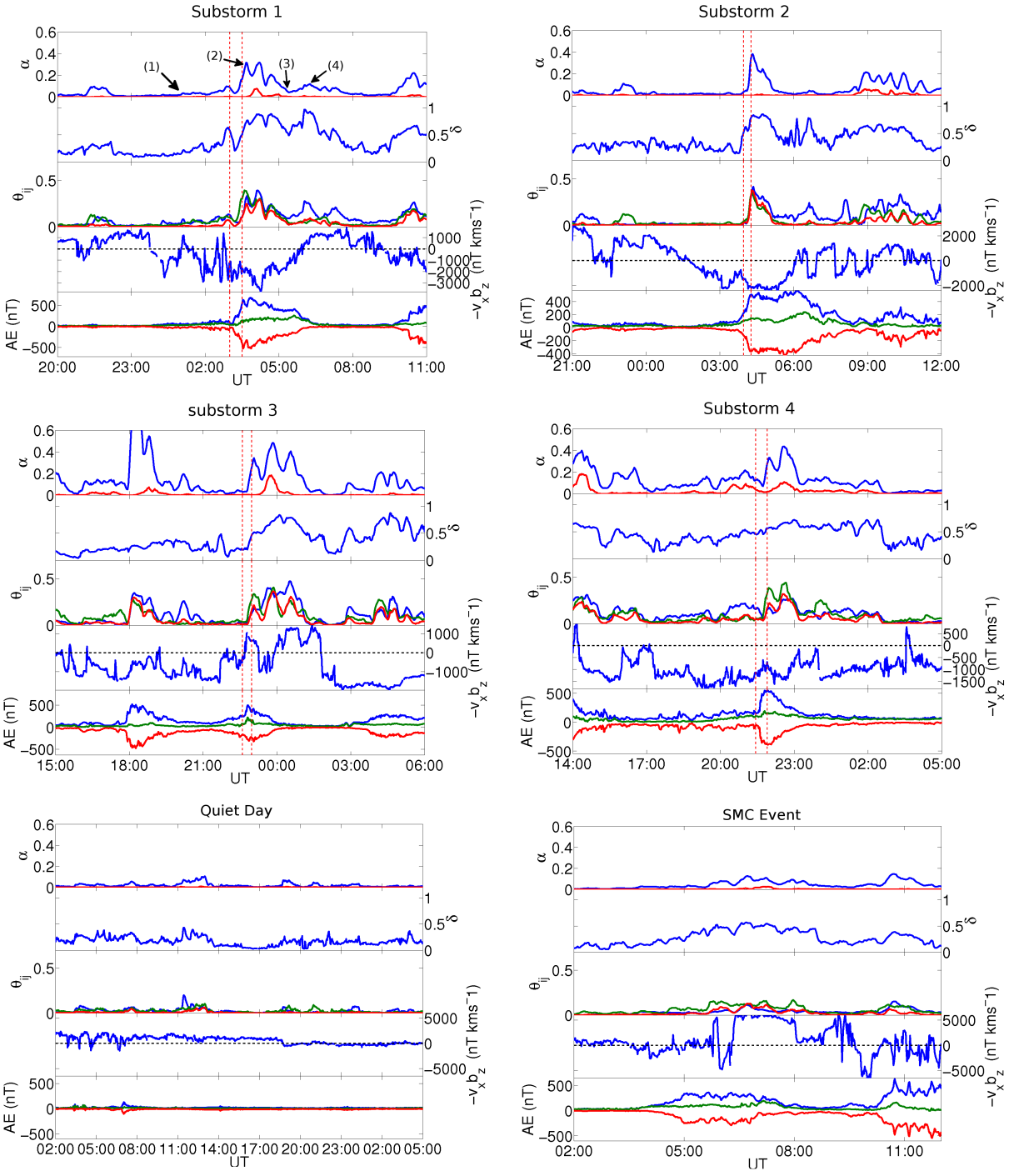

Figure 3.8: The time series of network parameters for all substorms, the SMC event and the quiet day using a 64 minute correlation window. The figure has the same format and axis scaling as figure 3.1

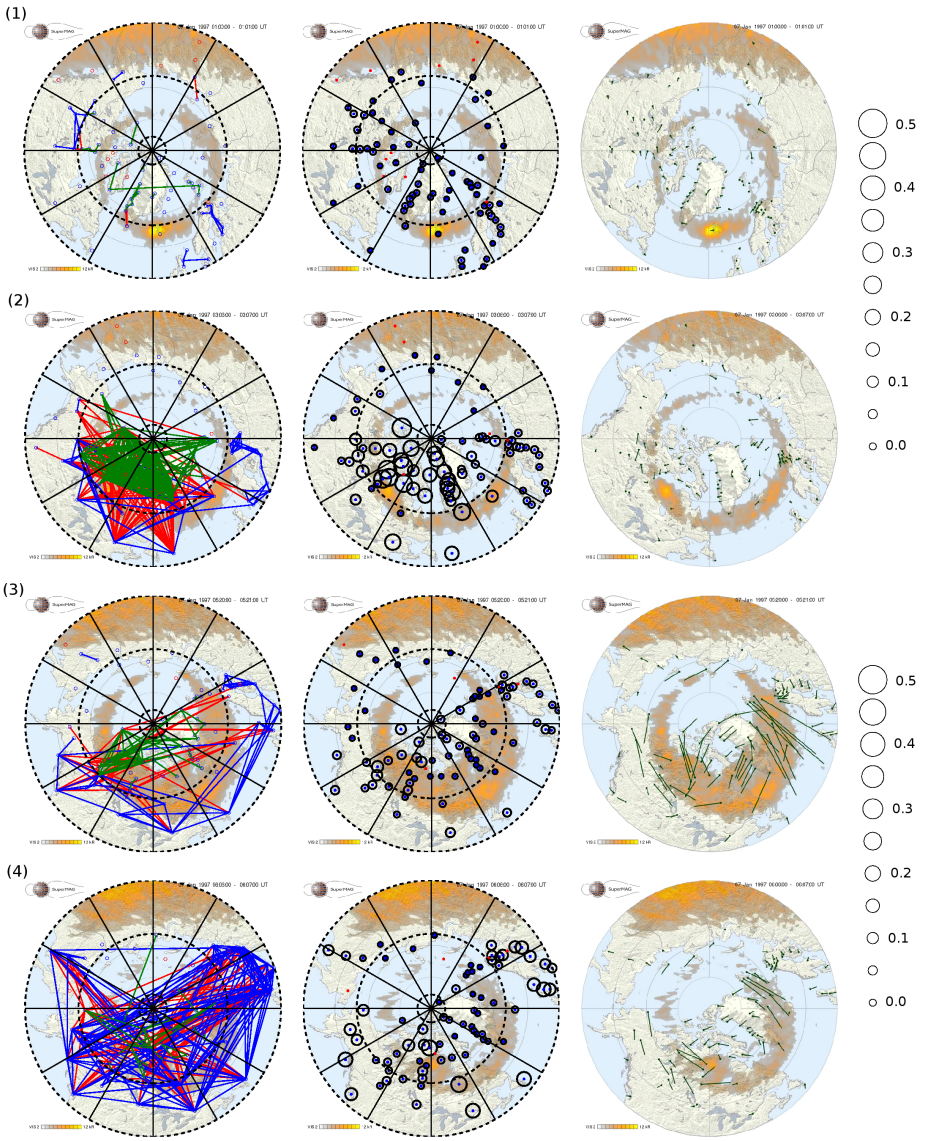

Figure 3.9: Connection maps, degree maps and VIS data in the same format as figure 3.2 for a 64 minute correlation window network. The times refer to those highlighted in figure 3.8

all events with a 64 minute window, this is shown in figure 3.8. The similarities to the 128 minute window are outlined as follows:

- There is the same clear response at onset of the substorm in terms of α and δ.
- A significant number of high latitude connections, as well as low and cross-latitudinal connections a represent at onset.
- Low latitude connections dominate the structure during the majority of substorms as they enter the recovery phase.

The differences are:

- The probability of false connections in the network is higher for all substorms compared to the 128 minute network except substorm 4. This is a consequence of (1) the number of points in the correlation analysis being reduced and (2) the fact that the individual thresholds for each station will not be the same as those used in the 128 minute network.
- The magnitude of the peaks in the network parameters are generally smaller for the 64 minute network; during the substorms maximum $\alpha \geq 0.32$ and $\delta \geq 0.72$. During the quiet day maximum $\alpha = 0.12$ and $\delta = 0.42$. For the SMC event maximum $\alpha = 0.13$ and $\delta = 0.58$.
- The position of the peaks in α seen during the substorm changes, as well as new peaks emerging.

The 64 minute correlation window network was found to be not as robust at differentiating substorm events from non-substorm events.

3.3 The "Average" Substorm

In this section we provide a cursory look at the aggregate network response to substorms. In chapter 1.5.1 we describe a few features that are usually present during a substorm, the localised onset brightening of the aurora oval, a rapid intensification of the westward electrojet (a rapid decrease in AL), dipolarisation of magnetic field in the near tail region and bulk Earthward flows. Several of these features are usually only visible from space, where measurements are not continuous, hence, there is sometimes uncertainty on whether a substorm is occurring. A way of identifying substorms from ground measurements only would be invaluable. The first step in doing so is to construct an aggregate network response for substorms.

In the same manner as outlined in section 3.1 we identify 116 isolated substorms and their onset times. We obtain networks for these events in an identical manner to the test case substorms following the methods outlined in chapter 2. In order to obtain the average response network to isolated substorms we first map the individual networks onto a regular grid by the methods outlined in chapter 2.5. $A^{*}_{kl(q)}(\tau)$ and $A^{**}_{kl(q)}(\tau)$ now represent the gridded network response matrix for an individual substorm event q centred on the time of the substorm onset. τ is the time elapsed since the substorm onset. The aggregate response matrix for the set of substorms is then,

$$A_{kl}(\tau) = \frac{\sum_{q=1}^{116} A^{*}_{kl(q)}(\tau)}{\sum_{q=1}^{M} A^{**}_{kl(q)}(\tau)}. \tag{3.6}$$

A_{kl} can take values between 0 and 1 and represents the average connection

likelihood for pair k,l during a substorm event.

In figure 3.10 we plot the aggregate network parameters for the average substorm. The parameters have the same meaning, broadly speaking, as those in section 3.1.1 but differ in their normalisation. The average connection distance δ is now,

$$\delta(\tau) = \frac{\sum_{k=1,k\neq l}^{N_g} \sum_{l=1,l\neq k}^{N_g} \sum_{q=1}^{M} A^{*}_{kl(q)}(\tau)\delta_{kl}}{\sum_{k=1,k\neq l}^{N_g} \sum_{l=1,l\neq k}^{N_g} \sum_{q=1}^{M} A^{**}_{kl(q)}(\tau)\delta_{kl}}, \tag{3.7}$$

where N_g is the number of grid cells. It is important to note that the value of δ for the aggregate response can not be directly equated to that used for the test case substorms.

The explicit forms of other parameters are given in 4. In figure 3.11 we show the network maps for two selected times, $\tau = 44$ mins and $\tau = 110$ mins. For these maps we split the the degree into short ($\delta_{kl} < 4000$km) and long range ($\delta_{kl} > 4000$km) (see chapter 4 for explicit definitions). The connection maps are constructed by considering only connections that are connected in at least 35% of the 116 substorm events. The connections plotted are split into long and short range connections. The aggregate network response shares some similar features to the results for the test case substorms. There is a significant increase in the connection likelihood shortly after the onset of the substorms. Unlike the test case substorms there is not a dominant high latitude network response at the onset, on the contrary the low latitude connections appear to dominate the network. The α, δ, $\theta_{h,l,c}$ responses all exhibit a two peak structure, with the peak closer to onset being smaller in magnitude. The increased average degree at the second peak indicates an increasingly global

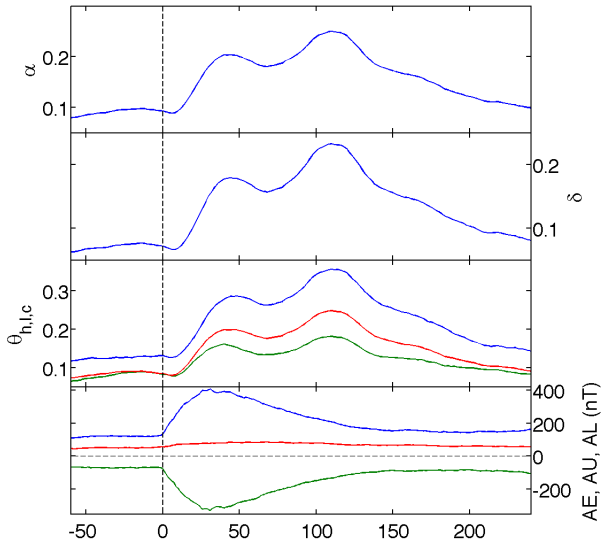

Figure 3.10: The network parameters for the aggregate network response to a set of 116 isolated substorms. Plotted from top to bottom is α, the average connection likelihood for the entire network, δ the average connection distance, $\theta_{h,l,c}$ the average connection likelihood for connections between high latitude grid cells (green), low latitude grid cells (blue), and connections between high and low latitude grid cells. AE (blue), AU (green) and AL (red) are averaged over the 116 substorm events. Highlighted are two times ($\tau = 44$ and $\tau = 110$) in which we show the network maps in figure 3.11.

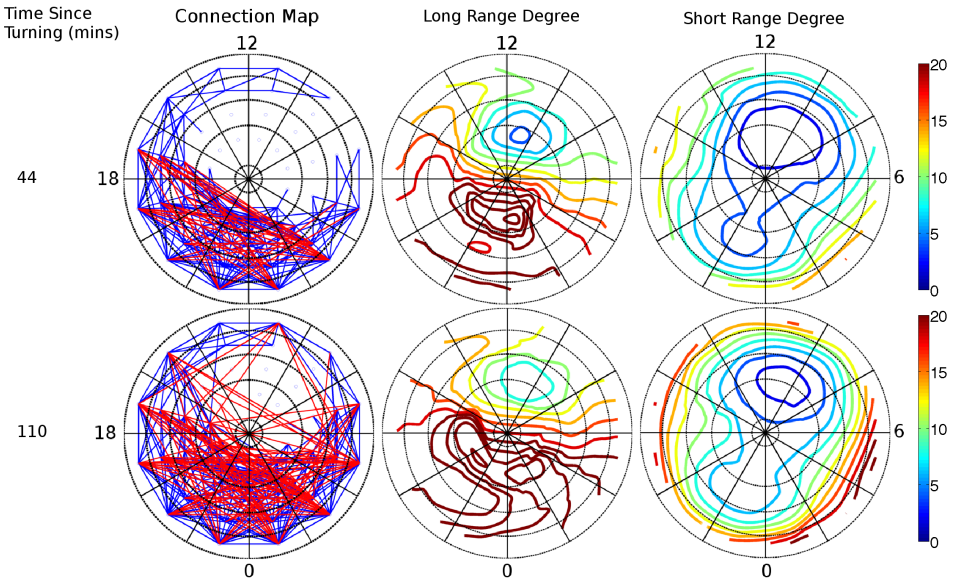

Figure 3.11: Snapshots of the correlation network maps for the aggregate network response to substorms at times $\tau = 44$ and $\tau = 110$, highlighted in figure 3.10. The figure is organised as follows: Left - the connection maps. Only connections where $A_{kl} > 0.35$ are plotted. Centre - the short range degree which quantifies the extent of connection between a particular region and all of its close neighbours (regions within 4000 km of each other). Right - the long range degree which quantifies the extent of connection between a given region and all other distant regions (regions greater than 4000 km away from each other). The contour values represent the % likelihood that a given region is connected to any other region in its network domain. The redder the contour the greater the increase in degree. The black dotted concentric circles represent the MLat contours. They are from outer to inner 50°, 58°, 66°, 74° and 82° MLat contours.

connection structure during the recovery phase.

Importantly, a visual inspection of the connection map at $\tau = 44$ shows that there is a very similar connection pattern to that found at time (2) in figure 3.2. The largest increase in short range degree is also found at high latitudes around 23 hours MLT, this is where the average location in which a substorm onset occurs [Gjerloev et al., 2007]. At $\tau = 110$ the region of enhanced short range correlation at high latitude has expanded. In addition there is now a significant number of long range connections at low latitudes

between dayside and nightside sectors. This bears resemblance to time (4) in figure 3.2 for the test case substorms. AE, AU, and AL at this point indicate that we are in the recovery phase for the majority of the substorm events. This gives further evidence to the idea that the system relaxes coherently on a global scale during the recovery phase.

3.4 Conclusions

3.4.1 Test Case Substorms

In this chapter we have outlined we applied dynamical network analysis to quantify substorm dynamics. Our results show that substorms can be characterised in terms of the spatial extent and level of cross-correlation seen between ground magnetometer stations. Our identification of a consistent network response at onset, that is distinct from events that can appear similar in AE (such as SMC events), opens possibilities of using dynamical network analysis to as a tool to assist in the identification of substorms using only ground station magnetometers. Information about the spatial distribution of correlation could also be useful in characterising the dynamics of a substorm, albeit with restricted time resolution due to the correlation window. We have found that there can be a large network response even when the amplitude of the station responses are small but above the noise. Thus network parameters and geomagnetic indices are complementary not directly comparable. This chapter is a 'proof of principle' in that it only explored four test cases for the technique, a more extensive statistical study is needed to fully establish the possibility for network analysis to as a method to routinely categorise substorms based

on a statistical network. The main results of this study are summarised here:

- The network exhibits a clear rapid response at onset indicated by an increase in connectivity and average connection distance.
- There is a strong increase in the number of high latitude connections at onset. These usually, but not always, dominate the network.
- Visual inspection of the connection structure at onset shows that they spatially coincide with the location of the onset brightening.
- The network response to the quiet day and SMC events give quantitatively distinct behaviour in the network parameters as compared to the substorm events.

In this chapter the dynamical network analysis was applied to substorm phenomena. However, with the appropriate window size and lags the technique, in principle, be applied to characterise other phenomena that occur in the magnetosphere. Due to the sparseness of the stations in some regions, however, the type of phenomena that can be reliably characterised must be large in its spatial extent.

3.4.2 The Average Substorm

In addition to applying dynamical network analysis to test case substorms, we also provided a cursory look at the aggregate network response to substorms. We found that the aggregate network response at onset featured a significant increase in short range high latitude connections around the expected average onset location for substorms. This is similar to the response found in test case

substorms. During the recovery phase the network exhibited a more global connection structure, indicative of the system relax to ground state coherently.

While we provided a first look at the aggregate network response there are problems with the way it is constructed. Substorms have different durations and onset locations, without accounting for this the response we obtain will be spatially and temporally smeared. Shifting the grid to account for the onset location may go some way to correcting this.

Chapter 4

Characterising the Ionospheric Convection Response to Southward and Northward IMF Turnings using dynamical Networks

The majority of the work in this chapter forms a paper submitted to GRL and is currently under review.

During periods of southward directed IMF a two cell ionospheric convection system is typically established [Dungey, 1961; Lu et al., 2002a] (see chapter 1.4.1). The convection system has a more complex structure during extended periods of northward IMF but normally involves a distorted two-cell or a multi-cell configuration [Greenwald et al., 1995]. A topical question is the nature of the dynamic ionospheric convection response to an IMF turning

that leads to a transition between these two states. The state of the convection system and its transition can be estimated by a variety of methods based on inferring or directly measuring ion flows [Brekke et al., 1973; Feldstein and Levitin, 1986] (see chapter 1.8). These methods require assumptions including the conductivity distribution in the ionosphere. The assimilative mapping of ionospheric electrodynamics (AMIE) method combines a variety of direct and indirect observations to constrain some, but not all, of these assumptions [Richmond, 1992] (see chapter 1.8).

Here, we will utilise the full set of ground based magnetometers in the northern hemisphere to characterise the time-dependent magnetospheric/ionospheric convection system. We utilise the network analysis methods described in chapter 2 that utilises the spatio-temporal correlation between all available pairs of magnetometer stations to characterise the system response. We then aggregate the cross-correlation network responses over 300-400 similar events to obtain an averaged response as a function of magnetic local time - magnetic latitude (MLT-MLat) and of the time delay since the occurrence of the IMF north-south and south-north turnings. Our aggregate dataset is restricted to turnings that occur during quiet-time conditions, that is, $|DST| < 30$nT and when there are no identifiable substorms. We propose network parameters that capture the spatial distribution of regions of enhanced cross-correlation in MLT-MLat and use them to characterise the convection system.

How fast the response to an IMF turning propagates from the dayside to the nightside of the ionosphere has been the topic of considerable discussion [Lockwood and Cowley, 1999]. Some studies suggest a propagation time in the convective response of $\sim$2 mins per hour of MLT [Lockwood et al., 1986; Todd et al., 1988; Khan and Cowley, 1999; Fiori et al., 2012]. They posit

that the change occurs slowly due the the fly wheel effect. Large convective bulk flows of charged particles occur during southward periods (these are $E \times B$ flows, see chapter 1.4), the charged particles collide with neutrals in the atmosphere causing neutral flows in the same direction over time. When the IMF turns northward, the $E \times B$ flows should stop but the momentum of the neutral flows prevents this from occurring immediately. Others indicate a near simultaneous (< 2 mins) global response to the turnings [Ridley et al., 1997, 1998; Ruohoniemi and Greenwald, 1998; Yu and Ridley, 2009]. Lu et al. [2002b] suggest the situation may be a combination of the two, i.e. there is an initial magnetoacoustic wave launched as a result of the turning that rapidly initiates the convective response globally. This is followed by a slower evolution of the convection system that reaches its peak in the dayside before the nightside, accounting for the delay in convection seen in Lockwood et al. [1986]; Todd et al. [1988]; Khan and Cowley [1999].

4.1 Data Used in this Study

We use vector magnetometer time series data at 1 minute cadence from years 1998-2004 from the SuperMAG database of ground station magnetometers. Magnetometer time series have been preprocessed as in Gjerloev [2012]. All magnetometer stations between 50° and 82° magnetic latitude (MLat) were included. Station pairs that are within a 300km geodesic separation of each other were excluded as they are likely to be correlated with each other at all times, i.e. they do not constitute spatially distinct observations. We use solar wind data from the ACE spacecraft (1998-2004) at 1 minute cadence from the SuperMAG database. The data is in a preprocessed format having

been propagated forward to the front of the magnetosphere using the pseudo-minimum variance technique of Weimer et al. [2003]; Weimer [2004]. We aim to characterise transitions in the quiet time convection system using ground station magnetometers. Quiet time here refers to times in which no geomagnetic substorms or storms ($|DST| < 30$nT) are occurring. We used the onset times from the substorm event list provided by SuperMAG to identify substorm intervals (see Newell and Gjerloev [2011b,a]). Data intervals from 30 mins before substorm onset to 3 hours after substorm onset were excluded from the analysis.

North-south and south-north IMF turnings are identified as periods in which IMF B_z is continually positive or negative for at least 30 mins preceding the turning. We select events for which B_z is continuously negative (or positive) for at least 40 mins and no longer than 80 mins post-turning (we also provide results for other intervals of continuously negative or positive B_z post-turning: 10-20, 20-40 and 80-150 mins in section 4.4). Continually negative (or positive) means here that B_z is of the same sign for 90% of the minimum of the time interval, we exclude events that do not satisfy this criterion. We further divide the north-south and south-north sets of turning events into those for which B_y is also continually positive (or negative) during the same post-turning interval. We do not have any requirement on IMF B_y before the north-south and south-north turnings. These sets of events are then aggregated to give an averaged response.

4.2 Forming the Fixed MLT-MLat Grid Networks

For studies of individual events such as substorms we can use the stations as locations of the network directly (see chapter 3. The nodes rotate with the earth and are not stationary in magnetic local time (MLT). Here, we will determine the aggregate response over many IMF turnings. The first step, for each event, is then to interpolate the network correlation properties of nodes in the station network, T_{ij}, onto a common grid that is static in MLT-MLat. The outline of the procedure is:

1. We construct the intermediate station network T_{ij} via the methods outlined in chapter 2. We use a 48 min running window to quantify the cross-correlation between the magnetic vector time series between each pair of stations i and j. The cross-correlation is calculated at 2 minute intervals for the years 1998-2004 at zero lag. We use a normalised average degree of $n_0 = 0.075$ to obtain the correlation threshold matrix. This normalised degree is greater than that used in 3, therefore, on average, there will be more false positives. The increased number of false positives is offset by the aggregation over many events.

2. We define a regular grid in MLT and MLat extending from 50° to 82° MLat with each grid cell spanning $\Delta\phi = 2$ hours in MLT and $\Delta\theta = 8°$ in MLat. We chose an optimal grid that gives the highest spatial resolution without missing connections. Missing connections occur when pairs of MLT-MLat grid cells are never populated by observing stations.

3. Network connections are mapped onto the grid using the methods outlined in chapter 2.

4.2.1 Aggregate Networks and Parameters

In this section we define the aggregate networks and the parameters we use to characterise them.

We aggregate M north-south (and south-north) turning events to form a normalised network response matrix $A_{kl}(\tau)$. The number of events in the 40-80 mins interval range north-south turning $+B_y$ set is 384, the $-B_y$ set 364 and the south-north turning $+B_y$ and $-B_y$ sets is 360 and 357 respectively. We define the event specific network response matrices $A^{*}_{kl(q)}(\tau)$ and $A^{**}_{kl(q)}(\tau)$ which are time centred on the turning event q. τ is the time that has elapsed following the turning. The normalised aggregate network response matrix A_{kl} is formed as follows:

$$A_{kl}(\tau) = \frac{\sum_{q=1}^{M} A^{*}_{kl(q)}(\tau)}{\sum_{q=1}^{M} A^{**}_{kl(q)}(\tau)}. \tag{4.1}$$

The $\sum_{q=1}^{M} A^{**}_{kl(q)}(\tau)$ is the maximum possible connectivity that can occur, summed over all turning events M; it acts as a normalisation since $\sum_{q=1}^{M} A^{*}_{kl(q)}(\tau) \leq \sum_{q=1}^{M} A^{**}_{kl(q)}(\tau)$. A_{kl} can then take values between 0 and 1, if $A_{kl} = 0$ then there were no network connections between grid cell pair k, l for any of the events, and if $A_{kl} = 1$ there is always a connection between grid cell pair k, l in every event.

We use time varying network parameters to quantify the aggregated network spatial pattern of correlation; these are similar to those defined in chapter 3 except that they differ in their normalisation. Here we normalise to the maximum possible connectivity in our network A^{**}_{kl} to obtain parameters as follows.

The average global connection likelihood α is

$$\alpha(\tau) = \frac{\sum_{k=1,k\neq l}^{N_g} \sum_{l=1,l\neq k}^{N_g} \sum_{q=1}^{M} A^{*}_{kl(q)}(\tau)}{\sum_{k=1,k\neq l}^{N_g} \sum_{l=1,l\neq k}^{N_g} \sum_{q=1}^{M} A^{**}_{kl(q)}(\tau)}, \tag{4.2}$$

where N_g is the number of grid cells in the network. We can define parameters for connectivity between different regions by choosing to sum over a subset of k and l in equation (4.2). We do this to define parameters for the average connection likelihood between grid cells within the dayside sector (ϕ_d) ($6 < MLT < 18$); within the nightside sector (ϕ_n) ($MLT > 18$ or $MLT < 6$); the average connection likelihood between dayside and nightside (ϕ_c).

The dayside, nightside and cross-connection likelihoods ϕ_d, ϕ_n, and ϕ_c are:

$$\phi_{d,n,c}(\tau) = \frac{\sum_{k=1,k\neq l}^{N_g} \sum_{l=1,l\neq k}^{N_g} \sum_{q=1}^{M} A^{*}_{kl(q)}(\tau) S_{kl,d,n,c}}{\sum_{k=1,k\neq l}^{N_g} \sum_{l\neq k}^{N_g} \sum_{q=1}^{M} A^{**}_{kl(q)}(\tau) S_{kl,d,n,c}}, \tag{4.3}$$

where $S_{kl,d,n,c}$ allows for the selection of a subset of the network; for example for dayside connections $S_{kl,d} = 1$ if both grid cell k and l lie on the dayside and $S_{kl,d} = 0$ otherwise.

The low, high and cross latitudinal connection likelihoods θ_h, θ_l and θ_c are:

$$\theta_{h,l,c}(\tau) = \frac{\sum_{k=1,k\neq l}^{N_g} \sum_{l=1,l\neq k}^{N_g} \sum_{q=1}^{M} A^{*}_{kl(q)}(\tau) S_{kl,h,l,c}}{\sum_{k=1,k\neq l}^{N_g} \sum_{l=1,l\neq k}^{N_g} \sum_{q=1}^{M} A^{**}_{kl(q)}(\tau) S_{kl,h,l,c}}, \tag{4.4}$$

where $S_{kl,h,l,c}$ is analogous to the above but selects for high, low and cross latitude connections.

We can also define short range (connections with geodesic separation $< 4000km$) and long range ($> 4000km$) normalised degree k $n_{k,S}$ and $n_{k,L}$ respectively for each grid cell. Network parameters $n_{k,S}$ and $n_{k,L}$ quantify how likely grid node k is to be connected to spatial regions within 4000km and beyond 4000km.

$$n_{k,S,L}(\tau) = \frac{\sum_{l=1,l\neq k}^{N_g} \sum_{q=1}^{M} A^{*}_{kl(q)}(t_q + \tau) S_{kl,S,L}}{\sum_{l=1,l\neq k}^{N_g} \sum_{q=1}^{M} A^{**}_{kl(q)}(t_q + \tau) S_{kl,S,L}}, \tag{4.5}$$

where $S_{kl,S,L}$ selects for allows for short range and long range grid cell pairs. The normalised grid cell degree n_k is formed by removing the S_{kl} matrix from equation 4.5.

All parameters representing the aggregated networks are calculated as deviations from a baseline network B_{kl}. The baseline network captures the typical cross-correlation between regions of MLT-MLat averaged over all possible unconstrained IMF conditions. B_{kl} is formed from the average of A_{kl} at $5 \times 10^3 \leq |\tau| \leq 10^4$ mins:

$$B_{kl} = \frac{\sum_{i=2500}^{5000} A^{*}_{kl}(2i)}{\sum_{i=2500}^{5000} A^{**}_{kl}(2i)}, \tag{4.6}$$

where $\tau = 2i$ (as the time step is 2 mins).

Unique baseline networks are formed for each of the aggregated north-south and south-north turning event sets. In figure 1(a) we show the probability densities for IMF B_y and B_z, $P(B_y)$ and $P(B_z)$ respectively, during quiescent (no storms and substorms occurring) and regular conditions. We

can see that the negative tail of the $P(B_z)$ is reduced during quiescent conditions, with the positive tail largely unchanged. The $P(B_y)$ distribution shows that the probability of $|B_y| > 5$ nT is reduced during quiescent conditions. By selecting for times in which no storms or substorms occur we are selecting periods of milder solar wind driving.

In figure 1(b)(c) we show a visual representation of the baseline network, 1(b) shows the short range degree and 1(c) the long range degree. The short range degree shows that there is more short range correlation between regions at 12-20 MLT and between regions at 00-04 MLT. The location of the increased correlation coincide with the expected locations of a twin convection cell, albeit under strongly $+B_y$ conditions. However, for the baseline networks the average $B_y \sim 0$ and $B_z \sim 0$, indicating that there is some inherent asymmetry (see chapter 1.4.2).

4.3 Correlation Network Response to IMF turnings for the 40-80 min Interval Range

Figure 4.2 shows aggregate network parameters plotted as a function of the time that has elapsed (delay) τ following the north-south and south-north turnings of the IMF propagated to the magnetopause. We eliminate any turning events from our aggregation that occur during substorms (any event that falls between 30 minutes before the substorm onset and 3 hours after substorm onset) and that occur during storms ($|DST| < 30$). The bottom panel in each of the sub-figures plots the IMF B_y and B_z components averaged over all events used to form each aggregate response. The network parameters are always

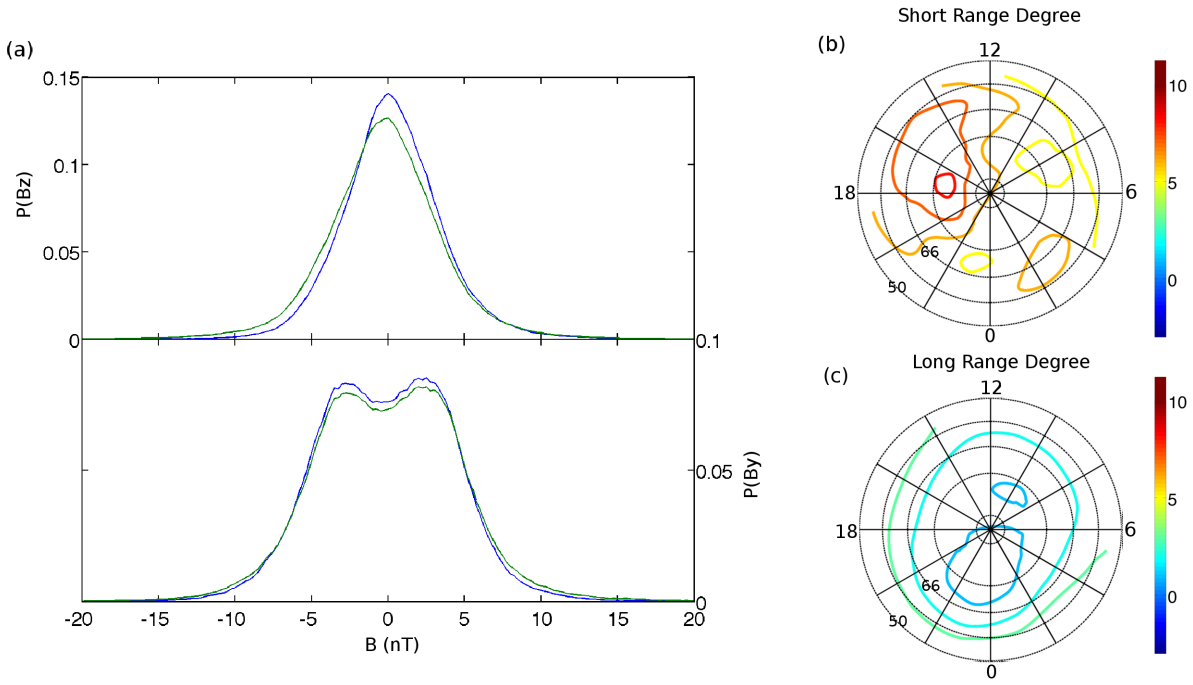

Figure 4.1: (a) The probability densities for IMF B_z (top panel) and B_y (bottom panel). The blue curves represents the probability densities during "quiet times" and the green curves represents the probability density at all times. (b) The contour plot shows the short range degree and (c) the long range degree for an example baseline network. The contour values represent the % likelihood that a given region is connected to any other region in its network domain (i.e., for short range degree, a region's domain contains the all other regions $< 4000km$ away). The redder the contour the greater the degree.

plotted at the time of the leading edge of the correlation window, i.e. at $\tau = 0$ data from τ =-48 to 0 mins is used to calculate the correlation network. We present the key results in the in this section; results for the network responses to north-south and south-north turnings at different time intervals for which IMF B_z remains the same sign following the turning, turnings that occur during the half year centred on winter solstice (winter events) or not (summer events) and, the influence of magnitude of B_z are reported in sections 4.4, 4.5 and 4.6 respectively.

4.3.1 North-South Turnings

Regardless of the duration of the southward IMF post turning, all event sets share a similar overall aggregate network response to the north-south turnings. At $\tau = 0$ mins, figure 4.2(a)(b) shows that the network response dips slightly below baseline, with reduced correlation primarily at low latitudes regions. Figure 4.3(a) provides a visual representation of the correlation network relative to baseline at several times that are indicated by the red vertical dashed lines in figure 4.2. The contour values represent the % likelihood, relative to baseline, that a given region is connected to any other region in its network domain (i.e., for short range degree, a region's domain contains all the other regions $< 4000km$ away). At $\tau = 0$ following the IMF turning, the dark blue regions of degree maps shows where the correlation is reduced which is predominantly at low latitudes for both the $+B_y$ and -B_y north-south event sets, for long and short range correlation. Below baseline correlation could be indicative of either weak ambient current system and/or a fast changing system that varies over small spatial scales that are not be resolved by the grid.

Figure 4.2(a)(b) shows that after $\tau = 10 \pm 2$ mins correlation in the network begins to increase, indicating that the magnetometer response to the turnings begins to fall within the leading edge of the correlation window. This suggests that 10 mins is the average communication delay between the time at which the southward turning reaches the magnetopause and the onset of the spatio-temporally correlated magnetometer response. This estimate is at most as precise as the technique used to propagate solar wind values to the magnetopause [Weimer et al., 2003]. Correlation in ϕ_d (the extent of correlation between regions within the dayside) begins to increase ∼2-8 mins before that of ϕ_n (the extent of correlation between regions within the nightside). Results for events with shorter post-turning interval ranges (10-20 and 20-40 mins) discussed in section 4.4 show shorter delays between increases in ϕ_d and ϕ_n of ~ 2 mins. The response in ϕ_c (extent of correlation between dayside and nightside regions) is typically seen after ϕ_d but before $\phi_n \sim 2$.

There is a multiple peak structure in α with the first and second peak occurring at $\tau = 34 \pm 2$ and $\tau = 60 \pm 2$ mins. The correlation window is 48 mins and multiple sub-peaks may simply indicate this is a result of the windowing (see section 4.9 for a simple model that clarifies this [Jackel et al., 2001]). Figure 4.3(a) show the degree maps at τ =34 mins for the $+B_y$ and -B_y event sets. The duskside has larger increases in short range correlation at τ =34 mins for both the $+B_y$ and -B_y event sets when compared to the increases on the dawnside. The long range degree does not show the same asymmetry. Additionally, regions of increases in short and long range correlation in the dawn hemisphere are shifted more towards dayside and spread over a wider area, 03-10 MLT, for the -B_y set compared to 01-05 MLT in the $+B_y$ set.

Figure 4.3(a) shows that regions that experience large increases in long

and short range correlation roughly coincide with the expected locations of negative and positive convection cells during southward IMF. The orientation the dawn-dusk convection cells is known to be influenced by the sign of B_y, with rotation of the system clockwise for $+B_y$ and vice versa [Walsh et al., 2014]. A similar rotation can be seen in our results, with the dawn region of increased long range correlation being shifted towards the dayside for the -B_y set compared to the $+B_y$ set. This again suggests that the correlation network is highlighting aspects of the convection system response.

At τ =60 mins, for the $+B_y$ event set, figure 4.3(a) shows that the regions of elevated short and long range correlation have expanded to lower latitudes as well as covering a larger area in MLT. There is no clear expansion of the regions of strong correlation to lower latitudes for the -B_y event set in the eastern hemisphere. After $\tau \simeq 60$ mins the IMF B_z averages to zero for both event sets. Correlation in the network remains raised above the significance level until $\tau \simeq$124 mins for both event sets. Also in the $+B_y$ set ϕ_d drops below significance before ϕ_n and the opposite is true for the -B_y case. The raised response in the network after the average B_z has fallen to zero may be indicative of energy stored during the period southward IMF slowly dissipating over a timescale ~ 60 mins. Our events only include quiet-time non-substorm times, hence our proposed dissipation time-scale applies to these times only.

4.3.2 South-North Turnings

Figure 4.2(c)(d) show the average network response to the south-north turnings events for $+B_y$ and -B_y respectively. We only aggregate over events that occur during times in which no substorms or storms are occurring. As in the

case of the north-south turnings, correlation begins to increase at $\tau \sim 8$ mins, suggesting a delay of ~ 8 mins between the time that the turning reaches the magnetosphere and the network response for the south-north turnings. This could suggest a magnetopause-ionosphere information transit time for both the north-south and south-north turnings that are similar to that found by Ridley et al. [1998] and references therein.

In contrast to the north-south turnings, from τ =0 to τ =8 mins, correlation in the network is enhanced above baseline for both $+B_y$ and -B_y event sets. Figure 4.3(b) provides snapshots of the network in an identical format to figure 4.3(a). The above baseline network response at the turning, $\tau = 0$, is mostly due to short range correlation at low latitudes. The picture is largely the same at τ=8 mins for both $+B_y$ and -B_y event sets.

As we found for the north-south turnings, figure 4.2 shows the same multiple peak structure in α but this occurs sooner than in the north-south turnings, with peaks at τ =30 and 56 mins in comparison to the $\tau = 34$ and $\tau = 60$ mins for the north-south turnings. The short range correlation at these times is strongest at low latitudes and long range at high latitudes. For the south-north turnings, responses in ϕ_n are already raised above significance before the turning in the $+B_y$ event set (likely due to southward IMF exciting the system before the turning). As such, we cannot obtain an estimate of the delay between responses in ϕ_d and ϕ_n in this case and others found in the section 4.4. In the $-B_y$ event set there does seem to be a delay between the initial responses of ϕ_d and ϕ_n of $\sim$ 6mins. Again ϕ_c responds ~ 2 mins after ϕ_d.

Our results for both the north-south and south-north turnings show delays in response times in ϕ_d (correlation within the dayside region) and

ϕ_n (correlation within the nightside region) of 2-8 mins for the post-turning intervals of 40-80 and 80-150 mins (section 4.4). ϕ_c (correlation between day and night regions) typically responds $\sim$ 2 mins after ϕ_d for the same event sets. However, the event sets with shorter post turning intervals (10-20 and 20-40 mins) typically show shorter delays, $\sim$ 2mins, between ϕ_d and ϕ_n. As such, the correlation network may be measuring two distinct and related contemporary processes. One possibility is that there is an initial impulsive response captured by the magnetometer timeseries due to a magneto-acoustic wave launched at the magnetopause as well as a slower gradual reconfiguration of the convection system [Lu et al., 2002b]. The magneto-acoustic wave would then account for the long range correlation between day-night, i.e. the response in ϕ_c. The slower reconfiguration of the convection system (which is known to reconfigure faster on the dayside than the nightside) is consistent with our findings that ϕ_d (correlation between regions on the dayside) responds 2-8 min before ϕ_n (correlation between regions on the nighside). This would also explain why the shorter interval ranges do not show delays >2 mins, since the IMF has not been southward or northward long enough for a reconfiguration response to be seen in the magnetometers.

At τ =30 mins, in figure 4.3(b), we can see that in the $+B_y$ event set the short range correlation shows the strongest increase at low latitudes regions at 12-19 MLT and 2-5 MLT. Increases in long range correlation are more local, with the strongest increases across at high latitudes at 16-19 MLT and 03-06 MLT. In the -B_y set, increases in short range correlation are largely confined to the dayside. The strongest increases in long range correlation occur at high latitude on the dawn hemisphere at 04-10 MLT with smaller increases occurring at 14-18 MLT. In both events sets the 22-02 MLT region shows almost no

significant response in long and short range correlation (blue regions). These blue regions indicate either no response or unresolved fine spatial structure and/or fast timescales. As in the north-south turnings, increases in correlation appear to spatially coincide with regions where the two cell convection pattern would be present given $+B_y$ or $-B_y$.

Figure 4.2 shows that the second peak in correlation at τ =56 mins is dominated by increases in ϕ_d, with only a slight increases in cross and nightside correlation for the $+B_y$ case. In figure 4.3(b) we see that the response seen at τ =30 mins has started to die away, with some remaining correlation at low latitudes and some small islands at high latitudes in long range degree. The blue regions indicating no enhanced correlation has expanded.

4.4 Correlation Network Response to Turnings Events for Different Post Turning Intervals Ranges

We aggregate turning events with different time intervals over which the IMF remains steadily northward or southward following the turnings. Figures 4.4 and 4.5 show the results for the 10-20 and 20-40 min interval ranges using the same methods as those found for the 40-80 mins interval range. Many of the same features highlighted in section 4.3 are apparent in at all interval ranges.

The delay between the maximal response in dayside and nightside correlation for events which have southward/northward post turnings IMF durations of 10-20 and 20-40 mins is 0-2 mins compared with the 2-8 mins found for the longer interval ranges 40-80 and 80-150 mins. This is consistent with

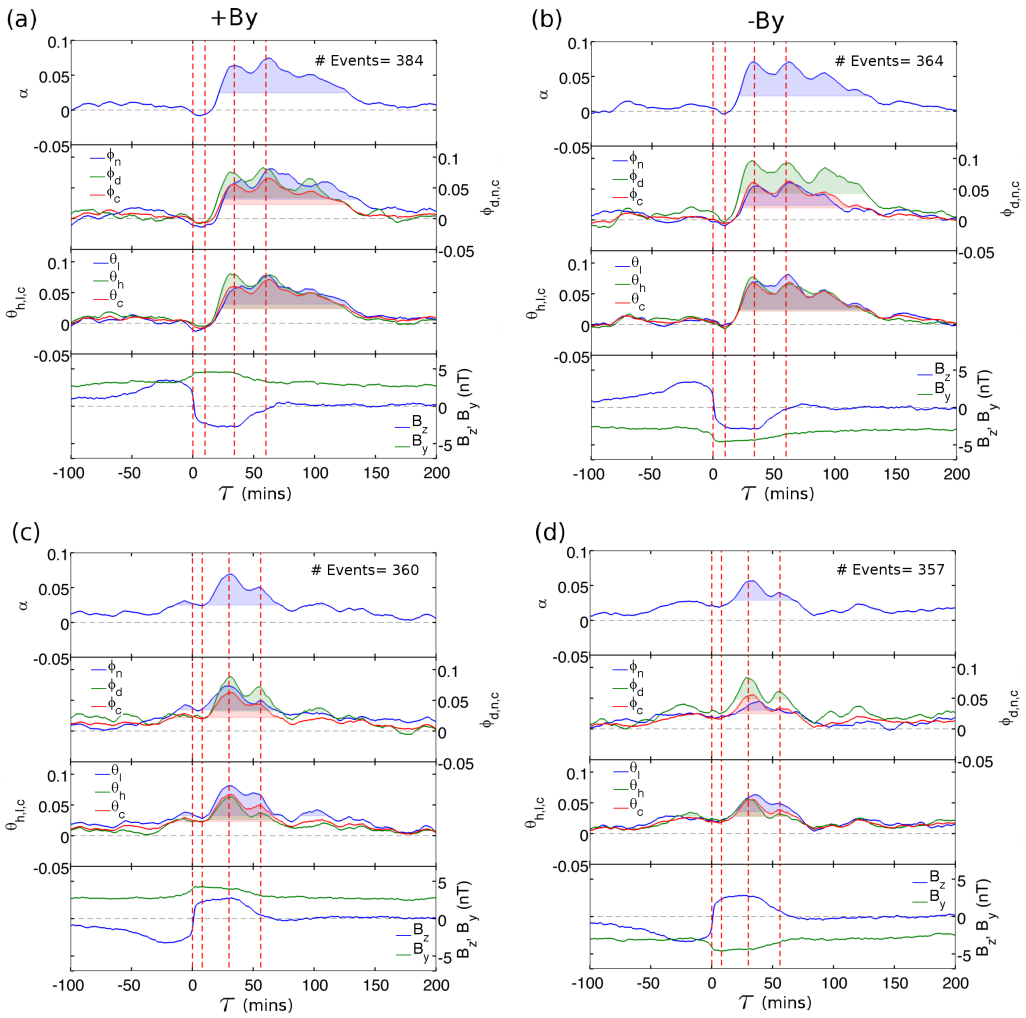

Figure 4.2: The aggregated network parameters for north-south (upper panels) and south-north (lower panels) IMF turnings for $+B_y$ (left panels) and -B_y (right panels) conditions as a function of delay τ elapsed since the turnings. These results aggregate events where B_y and B_z do not change sign over a 40-80 min time interval post turning. All parameters represent differences between the aggregate response for each subset of turning events and the baseline network. Each sub-figure plots, from top to bottom, as follows: α, the average connectivity between all turning events and all grid cells in the network; the average connectivity between the dayside regions ϕ_d (green), the nightside regions ϕ_n (blue) and connections between the dayside and nightside regions ϕ_c (red); the average connectivity between high latitude regions θ_h (green), low latitude regions θ_l (blue) and between high and low latitude regions θ_c (red); the average IMF B_z(blue) and B_y(green) for the turning events. The shading under the curves indicates statistical significance; values above significance have a probability < 0.0001 of belonging to the random distribution. This random distribution was formed by considering a model for the distribution of the values of each of the parameters at $|\tau| > 5000$ mins. Marked on all plots (vertical dashed red line) are several delays for which the network maps are displayed in figure 4.3. The delays are $\tau = 0$, 10, 34 and 60 mins for the north-south turnings (a)(b) and 0, 8, 30 and 56 for the south-north turning (c)(d).

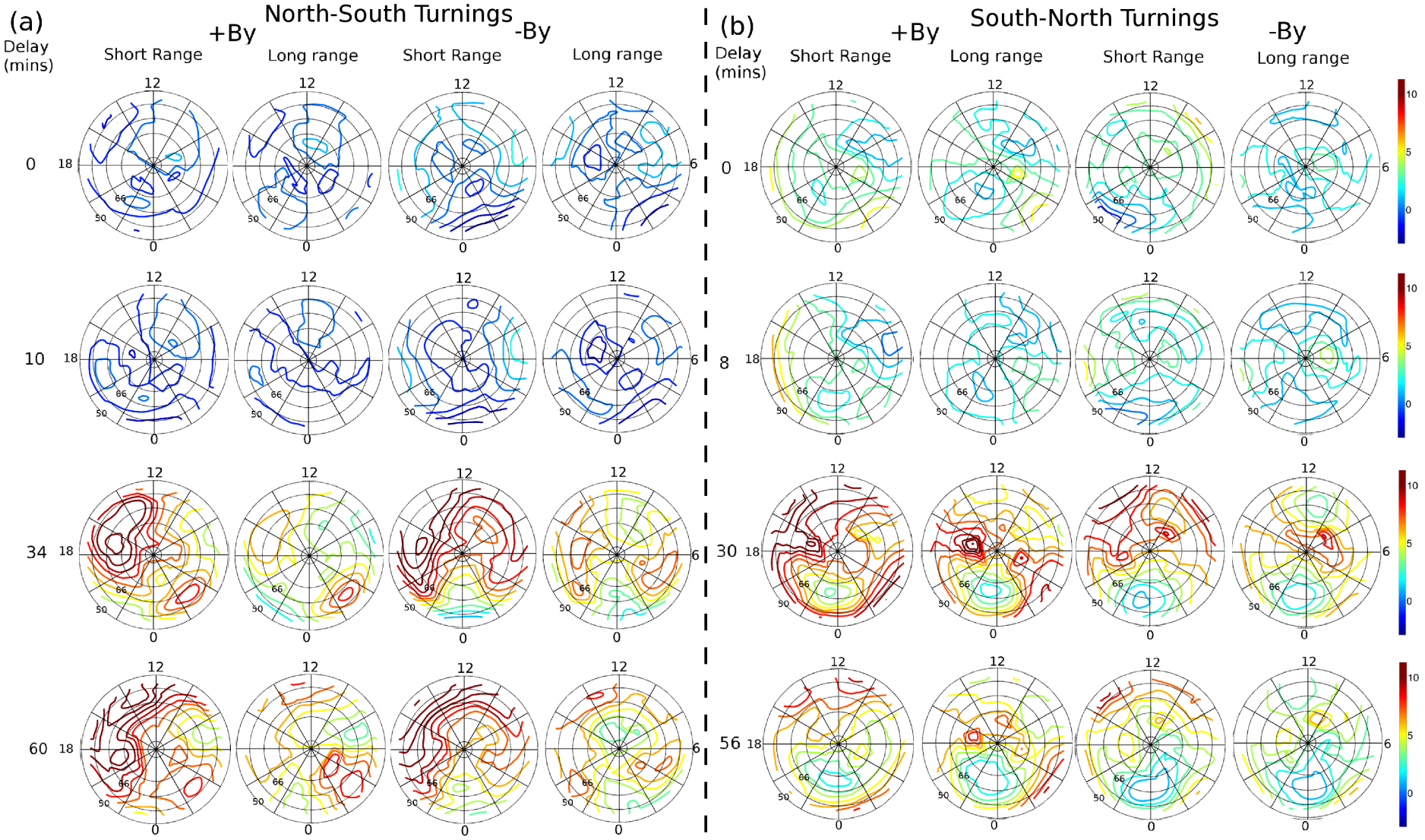

Figure 4.3: Snapshots of the correlation network maps for the north-south turnings at the delays τ following the turnings highlighted by the vertical dashed lines in figure 4.2 (a)(b). The figure is organised as follows: Left The short range degree which quantifies extent of connection between a particular region and all of its close neighbours (regions within 4000 km of each other). Right the long range degree which quantifies the extent of connection between a given region and all other distant regions (regions greater than 4000 km away from each other). The contour values represent the % likelihood, relative to baseline, that a given region is connected to any other region in its network domain. The redder the contour the greater the increase in degree. The black dotted concentric circles represent the MLat contours. They are from outer to inner 50°, 58°, 66°, 74° and 82° MLat contours

the two step process proposed by Lu et al. [2002b]. The correlated response in the magnetometers for the shorter duration event sets is a result of the magneto-acoustic wave initiating the convection change only, rather than a combination of wave and the slower reconfiguration processes.

For the longest interval range 80-150 minutes, figure 4.6, there is an insufficient number of events to divide the north-south and south-north turnings into $+B_y$ and $-B_y$ event sets.

Figure 4.6(a) shows much the same as the 40-80 interval north-south turning event set presented in section 4.3 (figure 4.2). The differences are the increased amount of time that ϕ_n remains above significance which can be explained by the long post-turning southward directed field. And time difference in the peak response of ϕ_d and ϕ_n being 8 minutes, longer than the other event sets.

Figure 4.6(b) shows that the south-north 80-150 minute post-turning interval event set reveals novel features not seen in section 4.3. There is a significant decrease in correlation after $\tau = 56$ mins, reaching a minimum at $\tau = 90$ for dayside correlation with a minimum for nightside correlation 26 minutes after. This drop-out in correlation to below baseline is not seen in any of the shorter turning intervals, possibly because the IMF has not been northward for a long enough period of time. The current systems associated with convection have likely decreased in magnitude.

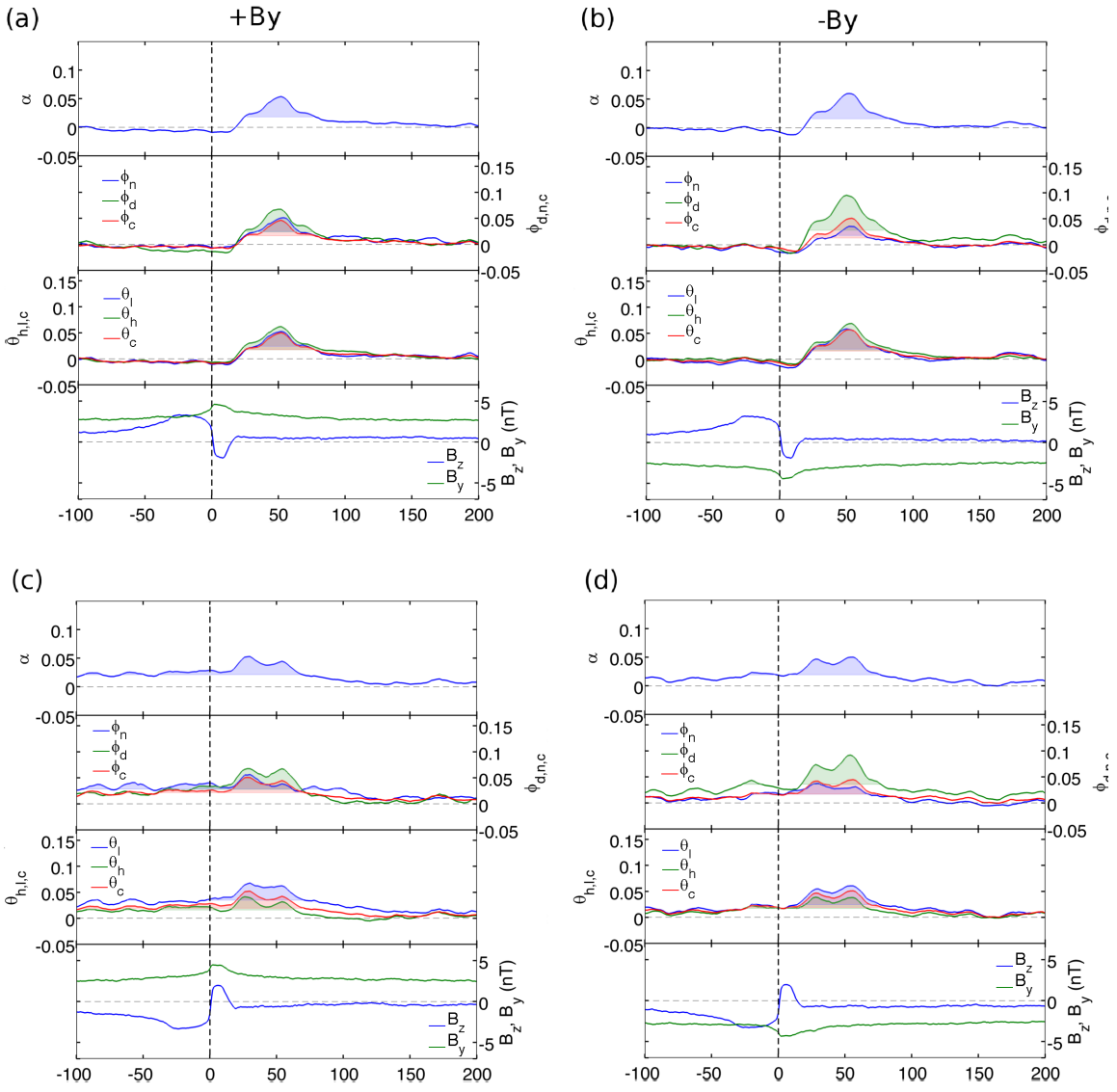

Figure 4.4: The aggregated network parameters for north-south (top panels) and south-north (bottom panels) IMF turnings for $+B_y$ (left panels) and $-B_y$ (right panels) conditions as a function of time delay since the turning for the 10-20 mins interval range. The figure follows the same format as figure 4.2. The time difference between the maximal response in ϕ_d and ϕ_n is 0-2 mins for all 10-20 mins interval event sets.

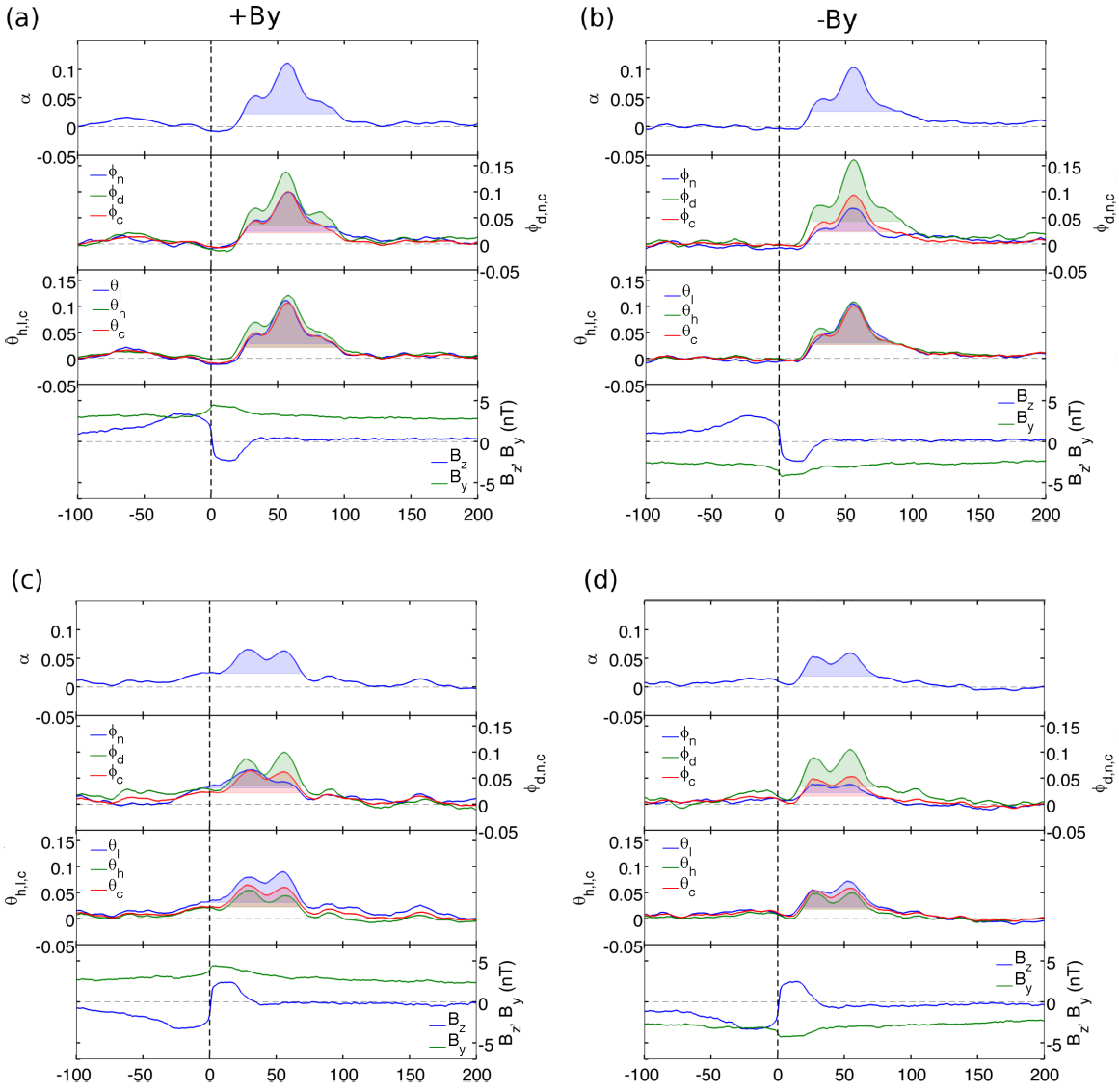

Figure 4.5: The aggregated network parameters for north-south (top panels) and south-north (bottom panels) IMF turnings for $+B_y$ (left panels) and $-B_y$ (right panels) conditions as a function of time delay since the turning for the 20-40 interval range. The figure follows the same format as figure 4.2. The delay between the maximal response in ϕ_d and ϕ_n is 0-2 mins for all 20-40 mins interval event sets.

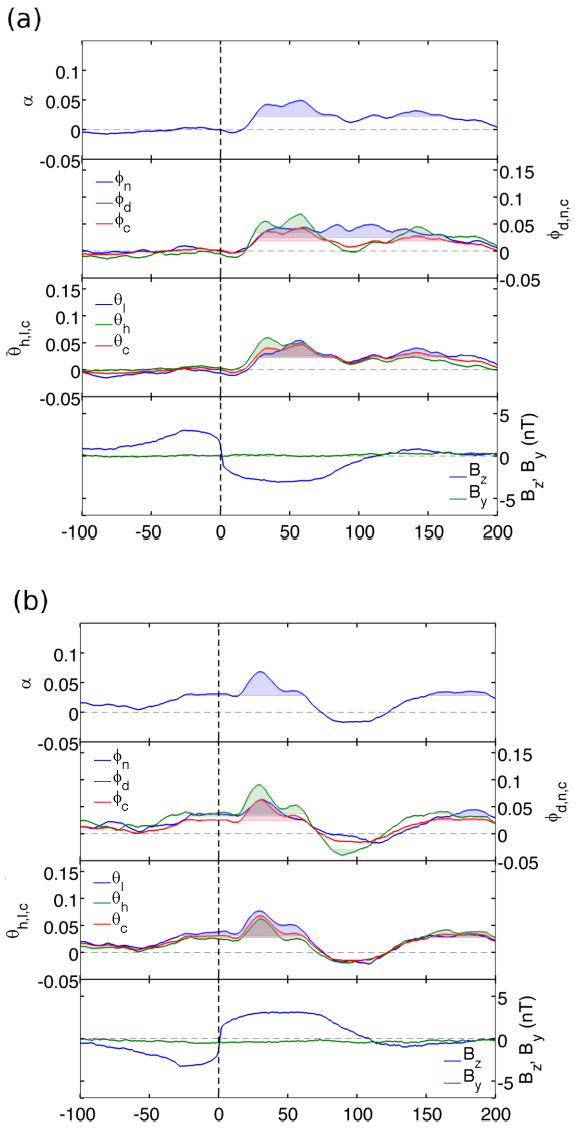

Figure 4.6: The aggregated network parameters for north-south (top panel) and south-north (bottom panel) IMF turnings for the 80-150 mins interval range. The figure follows the same format as figure 4.2. The delay between the maximal response in ϕ_d and ϕ_n is 2 mins for the south-north event sets and 8 mins for the north-south event sets

4.5 Correlation Network Response to Turning Events During Summer and Winter

The north-south and south-north turnings events are sub-divided into sets that occur during the half year centred on winter solstice (winter events) or not (summer events). Figure 4.7 provides the results for the north-south and south-north turnings events in the same format as figure 4.2.

We can see that there are two notable differences between the winter and summer events. The overall response to the turning (α) is larger for the summer events, with the majority of the increased correlation arising from increases in dayside correlation (ϕ_d). Additionally, the south-north turnings shows a stronger response in the low latitude correlation (θ_l) during summer events. Both of these observations are suggest that the ionospheric conductivity due to sunlight, known to have an influence on ionospheric convection Laundal et al. [2016], also has an influence the correlation between regions of the system.

4.6 Correlation Network Response to Turning Events of Differing Magnitude

The north-south and south-north turning events are sub-divided into sets where the post-turning IMF $|B_z|$ is continually $< 2nT$ for the "weak" turnings events and $> 2nT$ for the strong turning events. We did not explicitly control for $|B_z|$ before the turnings nor did we control for B_y post-turning due to an insufficient number of events.

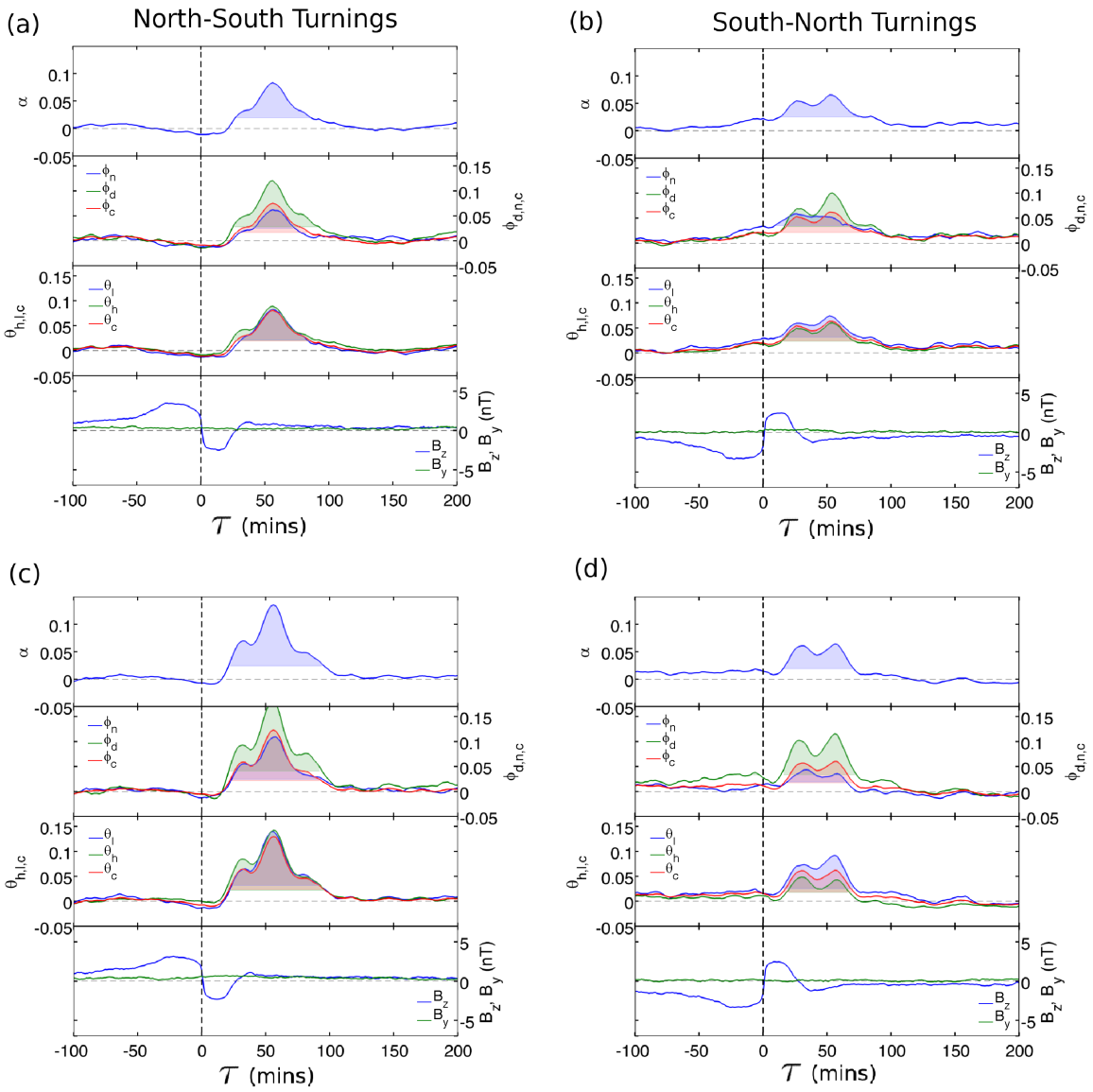

Figure 4.7: The aggregated network parameters for north-south (left panels) and south-north (right panels) IMF turnings for winter (top panels) and summer (bottom panels) conditions as a function of time delay since the turning for the 20-40 interval range. All parameters represent differences between the the aggregate response for each subset of turning events and the baseline network. The summer events show increased correlation overall, with the majority of the increases coming from increases dayside correlation.

We can see from figure 4.8 that there is a significantly reduced response for both the weak north-south and south-north turnings events. Additionally, delays between peaks in ϕ_d and ϕ_n are 4-8 mins for the weak turnings and 0-2 mins for the strong turnings. This may suggest that either the speed of convective change is dependent on the magnitude of the IMF turnings. Or, alternatively the results could be interpreted in the context of the two step process mentioned before Lu et al. [2002b]. If the magnitude of the response in the magnetometers due to a magneto-sonic wave launched by the southward turning is dependent on the magnitude of the turning, and if the magnetometer response due to the slower reconfiguration of the convection system is not as strongly dependent. This would lead to a magnetometer response dominated by the reconfiguration in the weak case and the wave in the strong turning case, leading to respective delays seen in correlation network response.

4.7 A simple Correlation Model for IMF Turnings

Here we show that the dual peak response seen in figure 4.2 may simply arise from the finite length cross-correlation window under-sampling the fine structure in the timeseries. To model the correlated magnetometer response we use a signal $S_i(t) = tanh(t) + R_i(t)$, where R(t) is a randomised $1/f^{\alpha}$ noise (correlated noise) and i references the test "stations" who each have a unique noise signal $R_i(t)$. The tanh function is used to model an IMF turning. Ground station magnetometers typically have an α between 1 and 3 [Jackel et al., 2001], here we chose $\alpha = 2$ for all stations. We use cross-correlation in lieu of

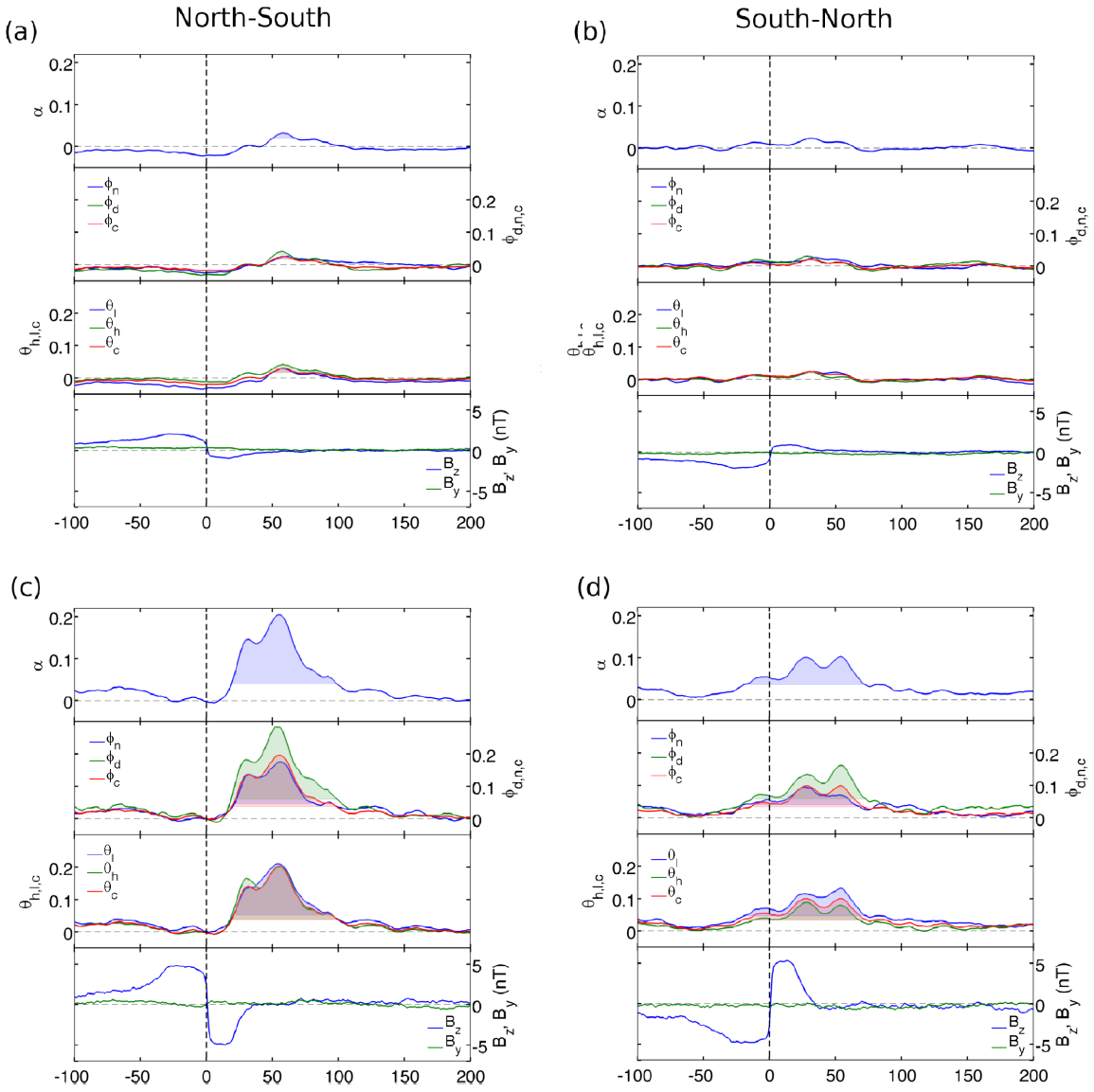

Figure 4.8: The aggregated network parameters for north-south (left panels) and south-north (right panels) IMF turnings for the 20-40 min post-turning interval range. The north-south and south-north turning events are split into those where post-turning $|B_z|$ is continually $< 2nT$ post turning (top panels) and $> 2nT$ for the strong turning events (bottom panels). The strong event sets show a significantly larger response to the turnings and have time differences between the maximums in ϕ_d and ϕ_n of 0-2 mins compared to 4-8 mins for the weak turning event sets.

canonical correlation used to form the real networks since we only have one component in this simplified model. We use an average power for the $R_i(t)$ noise component that is 10 times that of the tanh component signal. 48 test signals $S_i(t)$ are constructed and the cross-correlation between determined in an identical way to the methods found in chapter 2.

Despite the test signals being noise dominated figure 4.9 shows that the model quantitatively recreates the same dual peak feature as found in figure 1(main text). Importantly the separation between the peaks in the model is the same with the as separation between peaks in figure 4.2. We conclude that the dual peak response seen in figure 1 of the main text may be a result of the windowing.

4.8 Conclusions

We used a dynamical network of ground station magnetometers to quantify the quiet-time large scale ionospheric convection system response to north-south and south-north turnings. The spatio-temporal correlation between the full set of ground station magnetometers between 50-82° MLat in the northern hemisphere was used to construct the network. This method does not require any assumptions about the state of the ionosphere such as conductivity but relies on the the amplitude and phase information of all magnetometers time-series to characterise the system. We constructed time varying networks via canonical cross-correlation between the vector timeseries of pairs of magnetometer stations at zero lag for the years 1998-2004. Network information was mapped onto a stationary regular grid in MLT and MLat. We identified north-south and south-north turning events during quiet-time conditions (times in

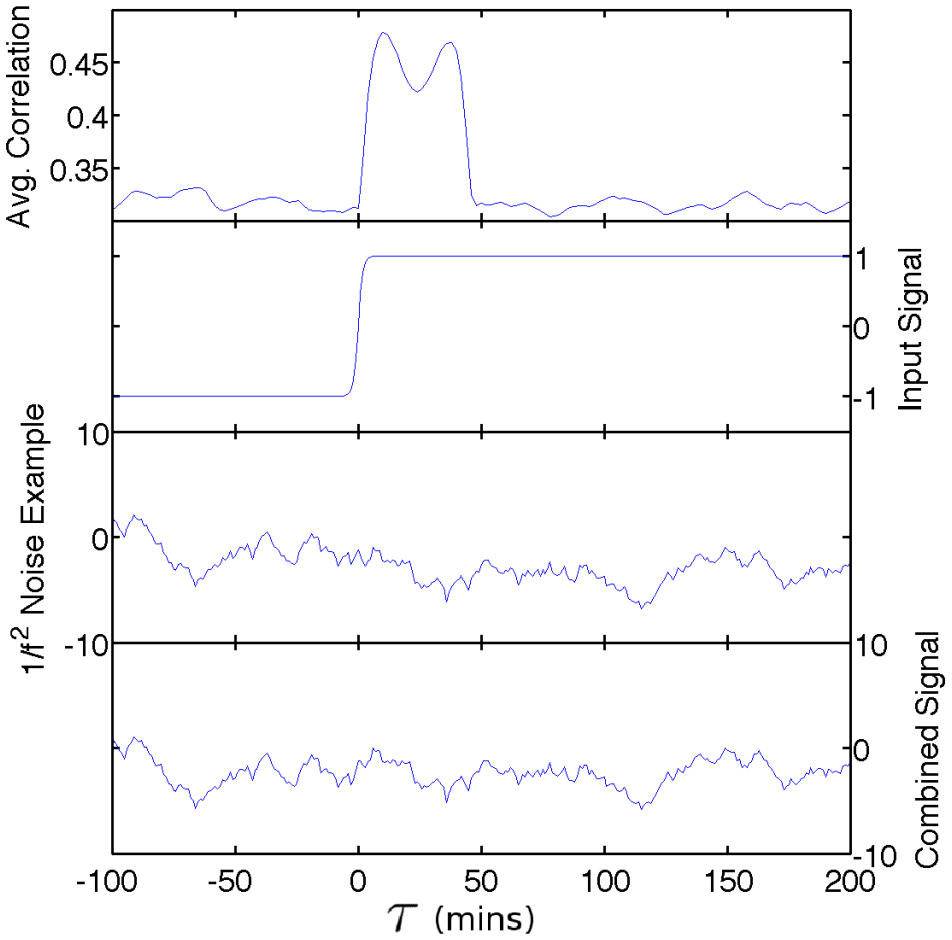

Figure 4.9: The figure from top to bottom shows the average cross-correlation between all test signals as a function of delay since the turning, the tanh(t) signal (exactly the same for all test signals), an example $R_i(t)$ and an example of the noise and the signal combined, $S_i(t)$

which no storms or substorms are occurring) for which B_y is either continually positive or negative after the turnings using ACE IMF data that had been propagated to the magnetopause. Aggregated network responses were formed for similar events as a function of delay (τ) since the north-south and south-north turnings. We find:

- Increases in spatio-temporal correlation in the network following a south-north and north-south turning. The detailed spatial pattern of this response depends on IMF B_y and whether the turning is north-south or south-north.

- There is a delay of ∼8-10 mins between the turning reaching the magnetopause and the response seen in the correlation network.

- The strongest increases in short range (geodesic separation between stations $<$ 4000 km) correlation is almost always in the afternoon-dusk region. Long range (geodesic separation $>$ 4000 km) correlation does not show this bias.

- The spatial pattern of long range correlation is reminiscent of a 2-cell convection pattern.

- Correlation is absent in the south-north turnings at midnight suggesting either weak current systems and/or a unresolved highly structured, fast changing system.

- A 2-8 mins delay between responses within the dayside (ϕ_d)($6 < MLT < 18$) and responses within the nighside ($6 > MLT$ or $MLT > 18$). In addition, there is a significant response in correlation between day and nightside regions, ϕ_c, that occurs shortly after ϕ_d and before ϕ_n

This work illustrates that dynamic correlation networks can characterise the spatio-temporal ionospheric response seen in the full set of ground based magnetometer stations. We find the time between the turnings reaching the magnetopause and a network response to be ∼8-10 minutes. If this time is comparable to the magnetopause-ionosphere information transit time it is consistent with Ridley et al. [1998] and references therein. In addition we find tentative evidence for a two step process in the convection response to an IMF B_z turning, that is, a fast initiation of the onset of convection change between day and night regions (evident from the smaller delay in response between ϕ_d and ϕ_n for shorter in section 4.4) followed by a more gradual reconfiguration occurring sooner on the dayside that the nightside (evident from the longer delays for the longer post-turning intervals in which we expect significant convective change to occur). Also, by the comparing of events occurring during summer and winter in section 4.5 we find that ionospheric conductivity due to sunlight, known to have an influence on ionospheric convection [Laundal et al., 2016], influences the strength of the correlation response in the dayside. Overall our results show that transitions in the convection system occur coherently with significant long range correlation between convective cell locations. Our method could be used to perform detailed comparisons between the extensive sets of observation and dynamical models of ionospheric current systems, to identify the exact physical causes of correlation between regions.

Chapter 5

Conclusions and Future Work

In this thesis we explored the use of dynamical networks in characterising physical processes that occur within the magnetosphere in a quantitatively manner. The dynamical networks were formed from the full set of ground station magnetometers available in the high latitude magnetosphere. Canonical correlation was used to establish the extent of quantitative similarity between the temporal variations of the vector magnetic field as seen in ground based magnetometers. In chapter 2 we found that the differing local characteristics of the ground stations magnetometers, such as different instrument response functions for each station, local ground conductivity, proximity to oceans and likely others, appeared to affect the typical correlation between stations. To address these effects we construct a threshold matrix that attempts to normalises the average degree for individual stations. If the local conditions for all stations in the network were identical, then under the application of a single global threshold, the degree for each station averaged over a sufficient period of time should also be identical. Therefore, any differences in the real world averaged station degree reflects the differing local conditions for each station.

We used this to identify the appropriate thresholds to normalise the average degree. In chapter 2 we also proposed an appropriate regular grid which we map the network on to. We found the most appropriate grid to be one that is regular in MLT and MLat. This aligns the grid with paths traced by the stations as they move through the MLT as the Earth rotates. The usual problem of larger physical spacing for lower latitude grid cells is mitigated by the stations at lower latitudes moving a greater physical distance than those at high latitudes during a finite time window.

In chapter 3 we applied our methodology described in chapter 2 to analyse four test case substorms and compare the responses to a steady magnetic convection event and a day in which no major geomagnetic disturbances occurred ("quiet day"). We found that using a 128 minute correlation window gave the most robust results in terms of the magnitude of the network response and the estimated number of false positives in the network. We compared a network constructed with cross-correlation at a 0 minute lag and at a 4 minute lag. We found that the 0 minute lag network gave a larger overall response to the substorms. In addition, the 4 minute lag network provided no more unique information. The magnitude and spatial extent of the network response to the test case substorms was found to be larger and distinct from the response the the steady magnetic event and the quiet day. Importantly, the distribution of connections in the network response tracked the sequence of events that are known to qualitatively occur during substorms. We associated the initial localised connections at high latitude to localised onset brightening. The transition from a network with a significant number of high latitude connections to a low latitude dominated network during the recovery phase fits the picture of the closed field lines on the nightside convecting around the flanks

of the magnetosphere to the dayside. The aggregate network response to 116 substorm events was also determined. The response showed similar features to that of the test cases, namely a increase in the short range high latitude connections about the expected onset location. In addition, we found a move toward a more global network response in the recovery phase. Inevitably the networks found in chapter 3 have an inhomogeneous spatial distribution of stations, with large gaps in the station coverage. This limits the usefulness of the methodology in quantifying substorms as it is impossible to determine whether different responses are due to characteristics of the event itself or the different distribution of stations in MLT-MLat.

In chapter 4 we characterised the response of the quiet-time large scale ionospheric convection system to north-south and south-north IMF turnings using a regular grid version of the dynamical networks. The influence of IMF B_y is also investigated. We identified several hundred north-south and south-north turning events that occurs during times in which no substorms or storms were occurring and aggregated network information for similar events. The spatial distribution of correlation in the network post north and south turnings was found to coincide with the expected locations of the convection cells. The orientation of the symmetry axis of the regions of increased correlation correlate with the state of IMF B_y in a similar to that of the convection system (see chapter 1.4.2). We found the time between the turnings reaching the magnetopause and a network response to be $\sim$ 8-10 minutes, if this maps onto the magnetopause-ionospheric communication time then it is consistent with that reported in Ridley et al. [1998]. We also examined the question of whether convective change propagates slowly from the dayside of the ionosphere to the nightside ($\sim$ 10 minutes) or if there is fast convective change ($\sim$ 2 minutes).

We observed evidence for both, the shorter post-turning intervals showed a short delay ($\leq$ 2 minutes) in the network response between the dayside and nightside whereas the longer post-turning interval event sets showed a range of delays (2-8 minutes). We interpreted this as a two part process, as per Lu et al. [2002b].

In conclusion dynamical networks appear to be able to distinguish between different large scale space weather events and convective responses. The network responses also seem correspond to the physical processes occurring during the events. In this sense network analysis may prove useful in the automated identification of known physical processes. However, the method has some limitations. The events analysed in this thesis were carefully chosen and the large scale picture of the progression of the events was already known. We have yet to show how to relate specific network responses to unknown physical processes that might be occurring.

5.0.1 Future Work

There are many ways the work presented in this thesis could be extended. Improvements could be made by utilising the recently developed gridded magnetometer data 1.8. This would allow for the construction of the network using spatially uniform data. In addition to this other external sources of information could be incorporated into the network, such as magnetic field measurements from the SWARM satellites and others that are in low Earth orbit. In addition, alternative methods could be used to identify similarity between the vector timeseries of the magnetometers stations, such as mutual information. This may reveal connections not seen in the current framework.

The gridded network data could be used to automate the identification of substorms. The aggregate network response to a set substorm events determined in chapter 3 could be used as a template. This could be used to identify substorms events based on a similarity of a networks response at a given time and the template.

Finally, ways linking a network response to a fundamental spatially distributed temporal pattern or perturbation of the magnetic field that causes the correlation could be considered. Identifying such a mode would allow for greater insights into the physicals processes that cause of the correlation in the network. The set of first canonical components associated with a subset of connected pairs in the network could be considered. Principle component analysis could then be performed on this set of components to see if there are only a few modes needed to explain the variance, and therefore the correlation within the subset.

Bibliography

Bob Abel and Richard M Thorne. Electron scattering loss in earth's inner magnetosphere: 1. dominant physical processes. *Journal of Geophysical Research: Space Physics*, 103(A2):2385–2396, 1998.

S-I Akasofu. The development of the auroral substorm. *Planetary and Space Science*, 12(4):273–282, 1964.

S-I Akasofu. Severalcontroversial'issues on substorms. *Space Science reviews*, 113(1-2):1–40, 2004. doi: 10.1023/B:SPAC.0000042938.57710.fb.

J A Van Allen. Observation of high intensity radiation by satellites 1958 alpha and gamma. *Journal of Jet Propulsion*, 28(9):588–592, 1958.

Vassilis Angelopoulos, James P McFadden, Davin Larson, Charles W Carlson, Stephen B Mende, Harald Frey, Tai Phan, David G Sibeck, Karl-Heinz Glassmeier, Uli Auster, et al. Tail reconnection triggering substorm onset. *Science*, 321(5891):931–935, 2008.

Markus Aschwanden. *Physics of the solar corona: an introduction with problems and solutions*. Springer Science & Business Media, 2006.

WI Axford. Viscous interaction between the solar wind and the earth's magnetosphere. *Planetary and Space Science*, 12(1):45–53, 1964.

Daniel N Baker, TI Pulkkinen, V Angelopoulos, W Baumjohann, and RL McPherron. Neutral line model of substorms: Past results and present view. *Journal of Geophysical Research: Space Physics*, 101(A6):12975–13010, 1996.

DN Baker, TI Pulkkinen, M Hesse, and RL McPherron. A quantitative assessment of energy storage and release in the earth's magnetotail. *Journal of geophysical research*, 102:7159–7168, 1997.

DN Baker, Eamonn Daly, Ioannis Daglis, John G Kappenman, and Mikhail Panasyuk. Effects of space weather on technology infrastructure. *Space Weather*, 2(2), 2004.

WG Baker and DF Martyn. Electric currents in the ionosphere. i. the conductivity. *Philosophical Transactions of the Royal Society of London A: Mathematical, Physical and Engineering Sciences*, 246(913):281–294, 1953.

Sanford Ballard, James Hipp, Brian Kraus, Andre Encarnacao, and Christopher Young. Geotess: A generalized earth model software utility. *Seismological Research Letters*, 87(3):719–725, 2016.

Marcelo Barreiro, Arturo C Marti, and Cristina Masoller. Inferring long memory processes in the climate network via ordinal pattern analysis. *Chaos: An Interdisciplinary Journal of Nonlinear Science*, 21(1):013101, 2011.

Ludwig Biermann. Kometenschweife und solare korpuskularstrahlung. *Zeitschrift fur Astrophysik*, 29:274, 1951.

DH Boteler. Geomagnetic effects on the pipe-to-soil potentials of a continental pipeline. *Advances in Space Research*, 26(1):15–20, 2000.

Thomas James Morrow Boyd and Jeffrey John Sanderson. Plasma dynamics. *Plasma dynamics, by TJM Boyd and JJ Sanderson. London, Nelson, 1969. Series: Applications of mathematics series ISBN: 177616113*, 1, 1969.

Ao Brekke, JR Doupnik, and PM Banks. A preliminary study of the neutral wind in the auroral e region. *J. Geophys. Res.*, 78(34):8235–8250, 1973.

D. R. Brillinger. *Time Series: Data Analysis and Theory*. Holden-Day, 1975.

M Brittnacher, M Fillingim, G Parks, G Germany, and J Spann. Polar cap area and boundary motion during substorms. *Journal of Geophysical Research: Space Physics*, 104(A6):12251–12262, 1999.

Seth Bullock, Lionel Barnett, and Ezequiel A Di Paolo. Spatial embedding and the structure of complex networks. *Complexity*, 16(2):20–28, 2010. doi: 10.1002/cplx.20338.

R. K. Burton, R. L. McPherron, and C. T. Russell. An empirical relationship between interplanetary conditions and dst. *Journal of Geophysical Research*, 80(31):4204–4214, 1975. ISSN 2156-2202. doi: 10.1029/JA080i031p04204. URL `http://dx.doi.org/10.1029/JA080i031p04204`.

S Chapman and VCA Ferraro. The geomagnetic ring-current: Iits radial stability. *Terrestrial Magnetism and Atmospheric Electricity*, 46(1):1–6, 1941.

Sydney Chapman and Vincent CA Ferraro. A new theory of magnetic storms. *Terrestrial Magnetism and Atmospheric Electricity*, 36(2):77–97, 1931.

SWH Cowley. The causes of convection in the earth's magnetosphere: A review of developments during the ims. *Reviews of Geophysics*, 20(3):531–565, 1982.

NU Crooker. Dayside merging and cusp geometry. *Journal of Geophysical Research: Space Physics*, 84(A3):951–959, 1979.

EA Davey, M Lester, SE Milan, RC Fear, and C Forsyth. The orientation and current density of the magnetotail current sheet: A statistical study of the effect of geomagnetic conditions. *Journal of Geophysical Research: Space Physics*, 117(A7), 2012.

AD DeJong, AJ Ridley, and CR Clauer. Balanced reconnection intervals: Four case studies. 2008.

J. Dods, S. C. Chapman, and J. W. Gjerloev. Network analysis of geomagnetic substorms using the supermag database of ground-based magnetometer stations. *J. Geophys. Res.*, 120(9):7774–7784, 2015. ISSN 2169-9402. doi: 10.1002/2015JA021456. URL `http://dx.doi.org/10.1002/2015JA021456`. 2015JA021456.

Jonathan F Donges, Yong Zou, Norbert Marwan, and Jürgen Kurths. The backbone of the climate network. *EPL (Europhysics Letters)*, 87(4):48007, 2009. doi: 10.1209/0295-5075/87/48007.

James W Dungey. Interplanetary magnetic field and the auroral zones. *Physical Review Letters*, 6(2):47, 1961.

James Wynne Dungey. Electrodynamics of the outer atmosphere. In *Physics of the Ionosphere*, volume 1, page 229, 1955.

TE Eastman, LA Frank, WK Peterson, and W Lennartsson. The plasma sheet boundary layer. *Journal of Geophysical Research: Space Physics*, 89(A3): 1553–1572, 1984.

Gary M Erickson. A quasi-static magnetospheric convection model in two dimensions. *Journal of Geophysical Research: Space Physics*, 97(A5):6505–6522, 1992.

Ya I Feldstein and AE Levitin. Solar wind control of electric fields and currents in the ionosphere. *J of Geomagn. and Geoelectr.*, 38(11):1143–1182, 1986.

R. A. D. Fiori, D. H. Boteler, and A. V. Koustov. Response of ionospheric convection to sharp southward imf turnings inferred from magnetometer and radar data. *J. Geophys. Res.*, 117(A9), 2012. ISSN 2156-2202. doi: 10.1029/2012JA017755. URL `http://dx.doi.org/10.1029/2012JA017755`. A09302.

M Forster, SE Haaland, GJ Paschmann, M Quinn, RB Torbert, H Vaith, and CA Kletzing. High-latitude plasma convection during northward imf as derived from in-situ magnetospheric cluster edi measurements. volume 26, page 2685. Citeseer, 2008.

Linton C Freeman. A set of measures of centrality based on betweenness. *Sociometry*, pages 35–41, 1977.

C Gabrielse, V Angelopoulos, A Runov, HU Frey, J McFadden, DE Larson, K-H Glassmeier, S Mende, CT Russell, S Apatenkov, et al. Timing and localization of near-earth tail and ionospheric signatures during a substorm onset. *Journal of Geophysical Research: Space Physics*, 114(A1), 2009.

Supriya B Ganguli. The polar wind. *Reviews of Geophysics*, 34(3):311–348, 1996.

Henry Berry Garrett. The charging of spacecraft surfaces. *Reviews of Geophysics*, 19(4):577–616, 1981.

JW Gjerloev. The supermag data processing technique. *J. Geophys. Res.*, 117 (A9), 2012. doi: 10.1029/2012JA017683.

JW Gjerloev and RA Hoffman. The large-scale current system during auroral substorms. *J. Geophys. Res.*, 119(6):4591–4606, 2014. doi: 10.1002/2013JA019176.

JW Gjerloev, RA Hoffman, MM Friel, LA Frank, and JB Sigwarth. Substorm behavior of the auroral electrojet indices. *Annales Geophysicae*, 22(6):2135–2149, 2004.

JW Gjerloev, RA Hoffman, JB Sigwarth, and LA Frank. Statistical description of the bulge-type auroral substorm in the far ultraviolet. *Journal of Geophysical Research: Space Physics*, 112(A7), 2007.

Melvyn L Goldstein and D Aaron Roberts. Magnetohydrodynamic turbulence in the solar wind. *Physics of Plasmas (1994-present)*, 6(11):4154–4160, 1999.

DO Gough and ME McIntyre. Inevitability of a magnetic field in the sun's radiative interior. *Nature*, 394(6695):755–757, 1998.

RA Greenwald, WA Bristow, GJ Sofko, C Senior, J-C Cerisier, and A Szabo. Super dual auroral radar network radar imaging of dayside high-latitude convection under northward interplanetary magnetic field: Toward resolving the distorted two-cell versus multicell controversy. *J. Geophys. Res.*, 100 (A10):19661–19674, 1995.

Adrian Grocott and Stephen Eric Milan. The influence of imf clock angle timescales on the morphology of ionospheric convection. *Journal of Geophysical Research: Space Physics*, 119(7):5861–5876, 2014.

SE Haaland, G Paschmann, M Förster, JM Quinn, RB Torbert, CE McIlwain, H Vaith, PA Puhl-Quinn, and CA Kletzing. High-latitude plasma convection from cluster edi measurements: method and imf-dependence. In *Annales Geophysicae*, volume 25, pages 239–253, 2007.

George E Hale. On the probable existence of a magnetic field in sun-spots. *The astrophysical journal*, 28:315, 1908.

John Keith Hargreaves. *The Solar-Terrestrial Environment: An Introduction to Geospace-the Science of the Terrestrial Upper Atmosphere, Ionosphere, and Magnetosphere*. Cambridge University Press, 1992.

Eo G Harris. On a plasma sheath separating regions of oppositely directed magnetic field. *Il Nuovo Cimento (1955-1965)*, 23(1):115–121, 1962.

Jobst Heitzig, Jonathan F Donges, Yong Zou, Norbert Marwan, and Jürgen Kurths. Node-weighted measures for complex networks with spatially embedded, sampled, or differently sized nodes. *The European Physical Journal B-Condensed Matter and Complex Systems*, 85(1):1–22, 2012. doi: 10.1140/epjb/e2011-20678-7.

MG Henderson, GD Reeves, RD Belian, and JS Murphree. Observations of magnetospheric substorms occurring with no apparent solar wind/imf trigger. *Journal of Geophysical Research: Space Physics*, 101(A5):10773–10791, 1996.

EW Hewson. A survey of the facts and the theories of the aurora. *Reviews of Modern Physics*, 9(4):403, 1937.

Jaroslav Hlinka, David Hartman, Martin Vejmelka, Jakob Runge, Norbert Marwan, Jürgen Kurths, and Milan Paluš. Reliability of inference of directed climate networks using conditional mutual information. *Entropy*, 15(6): 2023–2045, 2013.

Roger W Hockney and James W Eastwood. *Computer simulation using particles*. CRC Press, 1988.

Edward W Hones. Plasma sheet behavior during substorms. *Magnetic reconnection in space and laboratory plasmas*, pages 178–184, 1984.

Takesi Iijima and Thomas A Potemra. Field-aligned currents in the dayside cusp observed by triad. *Journal of Geophysical Research*, 81(34):5971–5979, 1976.

Brian J Jackel, Paul Eglitis, Eric F Donovan, Ari T Viljanen, Don D Wallis, Leroy L Cogger, and Hermann J Opgenoorth. Observations of highly correlated near-simultaneous magnetic field perturbations at contraposed ground stations. *J. Geophys. Res.*, 106(A11):25857–25872, 2001. doi: 10.1029/2001JA000105.

AS Janzhura and OA Troshichev. Determination of the running quiet daily geomagnetic variation. *Journal of Atmospheric and Solar-Terrestrial Physics*, 70(7):962–972, 2008.

Charles Y Johnson. Ion and neutral composition of the ionosphere. *Annals of the IQSY*, 5:197–213, 1969.

Jo Ann Joselyn. Geomagnetic quiet day selection. In *Quiet Daily Geomagnetic Fields*, pages 333–341. Springer, 1989.

Y Kamide and S Kokubun. Two-component auroral electrojet: Importance for substorm studies. *J. Geophys. Res.*, 101(A6):13027–13046, 1996.

Y Kamide, PD Perreault, S-I Akasofu, and JD Winningham. Dependence of substorm occurrence probability on the interplanetary magnetic field and on the size of the auroral oval. *Journal of Geophysical Research*, 82(35): 5521–5528, 1977.

Y Kamide, W Baumjohann, IA Daglis, WD Gonzalez, M Grande, JA Joselyn, RL McPherron, JL Phillips, EGD Reeves, G Rostoker, et al. Current understanding of magnetic storms: Storm-substorm relationships. *Journal of Geophysical Research: Space Physics*, 103(A8):17705–17728, 1998.

John G Kappenman. Geomagnetic storms and their impact on power systems. *IEEE Power Engineering Review*, 16(5):5, 1996.

H Khan and SWH Cowley. Observations of the response time of high-latitude ionospheric convection to variations in the interplanetary magnetic field using eiscat and imp-8 data. *Ann. Geophys.*, 17(10):1306–1335, 1999.

Margaret G Kivelson and Christopher T Russel. *Introduction to Space Physics*. CRC Press, 1995.

Stephen Knight. Parallel electric fields. *Planetary and Space Science*, 21(5): 741–750, 1973.

Hannu Koskinen. *Physics of Space Storms: From the Solar Surface to the Earth*. Springer Science & Business Media, 2011.

KM Laundal, JW Gjerloev, N Østgaard, JP Reistad, S Haaland, K Snekvik, P Tenfjord, S Ohtani, and SE Milan. The impact of sunlight on high-latitude equivalent currents. *J. Geophys. Res.*, 2016.

Naiguo Lin, H. U. Frey, S. B. Mende, F. S. Mozer, R. L. Lysak, Y. Song, and V. Angelopoulos. Statistical study of substorm timing sequence. *Journal of Geophysical Research: Space Physics*, 114(A12): n/a–n/a, 2009. ISSN 2156-2202. doi: 10.1029/2009JA014381. URL `http://dx.doi.org/10.1029/2009JA014381`. A12204.

M Lockwood and SWH Cowley. Comment on a statistical study of the ionospheric convection response to changing interplanetary magnetic field conditions using the assimilative mapping of ionospheric electrodynamics technique by aj ridley et al. *J. Geophys. Res.*, 104(A3):4387–4391, 1999.

M Lockwood, AP Van Eyken, BJI Bromage, DM Willis, and SWH Cowley. Eastward propagation of a plasma convection enhancement following a southward turning of the interplanetary magnetic field. *Geophys. Res. Lett.*, 13(1):72–75, 1986.

CA Loewe and GW Prölss. Classification and mean behavior of magnetic storms. *Journal of Geophysical Research: Space Physics*, 102(A7):14209–14213, 1997.

G. Lu, S.W.H. Cowley, S.E. Milan, D.G. Sibeck, R.A. Greenwald, and T. Moretto. Solar wind effects on ionospheric convection: a review. *Journal of Atmospheric and Solar-Terrestrial Physics*, 64(2):145 – 157, 2002a. ISSN 1364-6826. doi: http://dx.doi.org/10.1016/S1364-6826(01)00080-3.

G Lu, TE Holzer, D Lummerzheim, JM Ruohoniemi, P Stauning, O Troshichev, PT Newell, M Brittnacher, and G Parks. Ionospheric response to the interplanetary magnetic field southward turning: Fast onset and slow reconfiguration. *J. Geophys. Res.*, 107(A8):SIA–2, 2002b.

ATY Lui, V Angelopoulos, O LeContel, H Frey, E Donovan, DG Sibeck, W Liu, HU Auster, D Larson, X Li, et al. Determination of the substorm initiation region from a major conjunction interval of themis satellites. *Journal of Geophysical Research: Space Physics*, 113(A1), 2008.

John G Lyon. The solar wind-magnetosphere-ionosphere system. *Science*, 288 (5473):1987–1991, 2000.

LR Lyons. Substorms: Fundamental observational features, distinction from other disturbances, and external triggering. *Journal of Geophysical Research: Space Physics*, 101(A6):13011–13025, 1996.

Nishant Malik, Bodo Bookhagen, Norbert Marwan, and Jürgen Kurths. Analysis of spatial and temporal extreme monsoonal rainfall over south asia using complex networks. *Climate dynamics*, 39(3-4):971–987, 2012. doi: 10.1007/s00382-011-1156-4.

McPherron RLRH Manka. Dynamics of the 1054 ut march 22. 1979. substorm event: Cdaw 6. *Journal of Geophysical Research*, 90(A2):1175–1190, 1985.

R L McPherron, C T Russell, and M P Aubry. Satellite studies of magnetospheric substorms on august 15, 1968: 9. phenomenological model for substorms. *J. Geophys. Res.*, 78(16):3131–3149, 1973. doi: 10.1029/JA078i016p03131.

Ching-I Meng and Kan Liou. Substorm timings and timescales: A new aspect. *Space science reviews*, 113(1-2):41–75, 2004. doi: 10.1023/B:SPAC.0000042939.88548.68.

Stanley Milgram. The small world problem. *Psychology today*, 2(1):60–67, 1967.

Susumu Mori, Walter E Kaufmann, Christos Davatzikos, Bram Stieltjes, Laura Amodei, Kim Fredericksen, Godfrey D Pearlson, Elias R Melhem, Meiyappan Solaiyappan, Gerald V Raymond, et al. Imaging cortical association tracts in the human brain using diffusion-tensor-based axonal tracking. *Magnetic resonance in medicine*, 47(2):215–223, 2002.

Tsutomu Nagatsuma. Saturation of polar cap potential by intense solar wind electric fields. *Geophysical Research Letters*, 29(10):62–1–62–4, 2002. ISSN 1944-8007. doi: 10.1029/2001GL014202. URL `http://dx.doi.org/10.1029/2001GL014202`.

P. T. Newell and J. W. Gjerloev. Substorm and magnetosphere characteristic scales inferred from the supermag auroral electrojet indices. *J. Geophys. Res.*, 116(A12):n/a–n/a, 2011a. ISSN 2156-2202. doi: 10.1029/2011JA016936. URL `http://dx.doi.org/10.1029/2011JA016936`. A12232.

P. T. Newell and J. W. Gjerloev. Evaluation of supermag auroral electrojet indices as indicators of substorms and auroral power. *J. Geophys. Res.*, 116 (A12):n/a–n/a, 2011b. ISSN 2156-2202. doi: 10.1029/2011JA016779. URL `http://dx.doi.org/10.1029/2011JA016779`. A12211.

M. E. J. Newman. *Networks: An Introduction*. Oxford University Press, 2010.

Ruth M Nicol, Sandra C Chapman, Petra E Vértes, Pradeep J Nathan, Marie L Smith, Yury Shtyrov, and Edward T Bullmore. Fast reconfiguration of high-frequency brain networks in response to surprising changes in auditory input. *J. Neurophys*, 107(5):1421–1430, 2012. doi: 10.1152/jn.00817.2011.

A Nishida and Nl Nagayama. Synoptic survey for the neutral line in the magnetotail during the substorm expansion phase. *Journal of Geophysical Research*, 78(19):3782–3798, 1973.

Atsuhiro Nishida. Formation of plasmapause, or magnetospheric plasma knee, by the combined action of magnetospheric convection and plasma escape from the tail. *Journal of Geophysical Research*, 71(23):5669–5679, 1966.

John V Olson. Pi2 pulsations and substorm onsets: A review. *Journal of Geophysical Research: Space Physics*, 104(A8):17499–17520, 1999.

Eugene N Parker. Sweet's mechanism for merging magnetic fields in conducting fluids. *Journal of Geophysical Research*, 62(4):509–520, 1957.

Eugene N Parker. Dynamics of the interplanetary gas and magnetic fields. *The Astrophysical Journal*, 128:664, 1958.

Paul Perreault and SI Akasofu. A study of geomagnetic storms. *Geophysical Journal International*, 54(3):547–573, 1978.

Harry E Petschek. Magnetic field annihilation. *NASA Special Publication*, 50: 425, 1964.

Alexander Piel and Michael Brown. Plasma physics: An introduction to laboratory, space, and fusion plasmas. *Physics Today*, 64(6):55, 2011.

Tuija Pulkkinen. Space weather: terrestrial perspective. *Living Reviews in Solar Physics*, 4(1):1–60, 2007.

Alexander Radebach, Reik V Donner, Jakob Runge, Jonathan F Donges, and Jürgen Kurths. Disentangling different types of el niño episodes by evolving climate network analysis. *Physical Review E*, 88(5):052807, 2013. doi: 10.1103/PhysRevE.88.052807.

AD Richmond. Assimilative mapping of ionospheric electrodynamics. *Advan. in Space Res.*, 12(6):59–68, 1992.

AJ Ridley, Gang Lu, CR Clauer, and VO Papitashvili. Ionospheric convection during nonsteady interplanetary magnetic field conditions. *J. Geophys. Res.*, 102(A7):14563–14579, 1997.

AJ Ridley, Gang Lu, CR Clauer, and VO Papitashvili. A statistical study of the ionospheric convection response to changing interplanetary magnetic field conditions using the assimilative mapping of ionospheric electrodynamics technique. *J. Geophys. Res.*, 103(A3):4023–4039, 1998.

AJ Ridley, TI Gombosi, and DL DeZeeuw. Ionospheric control of the magnetosphere: Conductance. In *Annales Geophysicae*, volume 22, pages 567–584, 2004.

JM Ruohoniemi and KB Baker. Large-scale imaging of high-latitude convection with super dual auroral radar network hf radar observations. *Journal of Geophysical Research: Space Physics*, 103(A9):20797–20811, 1998.

JM Ruohoniemi and RA Greenwald. Statistical patterns of high-latitude con-

vection obtained from goose bay hf radar observations. *JOURNAL OF GEOPHYSICAL RESEARCH-ALL SERIES-*, 101:21–743, 1996.

JM Ruohoniemi and RA Greenwald. The response of high-latitude convection to a sudden southward imf turning. *Geophys. Res. Lett.*, 25(15):2913–2916, 1998.

Christopher T Russell. Geophysical coordinate transformations. *Cosmic Electrodynamics*, 2(2):184–196, 1971.

K Schindler. A theory of the substorm mechanism. *Journal of Geophysical Research*, 79(19):2803–2810, 1974.

V. A. Sergeev, V. Angelopoulos, and R. Nakamura. Recent advances in understanding substorm dynamics. *Geophysical Research Letters*, 39(5): n/a–n/a, 2012. ISSN 1944-8007. doi: 10.1029/2012GL050859. URL `http://dx.doi.org/10.1029/2012GL050859`. L05101.

VA Sergeev, R Jo Pellinen, and TI Pulkkinen. Steady magnetospheric convection: A review of recent results. *Space Science Reviews*, 75(3-4):551–604, 1996.

K Shiokawa, W Baumjohann, G Haerendel, G Paschmann, JF Fennell, E Friis-Christensen, H Lühr, GD Reeves, CT Russell, Po R Sutcliffe, et al. High-speed ion flow, substorm current wedge, and multiple pi 2 pulsations. *Journal of Geophysical Research: Space Physics*, 103(A3):4491–4507, 1998.

David G Sibeck, RE Lopez, and EC Roelof. Solar wind control of the magnetopause shape, location, and motion. *J. Geophys. Res.*, 96(A4):5489–5495, 1991.

Fikret Sivrikaya and Bülent Yener. Time synchronization in sensor networks: a survey. *Network, IEEE*, 18(4):45–50, 2004. doi: 10.1109/MNET.2004.1316761.

Dirk JA Smit, Cornelis J Stam, Danielle Posthuma, Dorret I Boomsma, and Eco JC De Geus. Heritability of small-world networks in the brain: a graph theoretical analysis of resting-state eeg functional connectivity. *Human brain mapping*, 29(12):1368–1378, 2008.

MT Syrjasuo, EF Donovan, X Qin, et al. Automatic classification of auroral images in substorm studies. *International Conference on Substorms (ICS8), University of Calgary, Alberta, Canada*, pages 309–313, 2007.

T Tanaka. Interplanetary magnetic field b y and auroral conductance effects on high-latitude ionospheric convection patterns. *Journal of Geophysical Research: Space Physics*, 106(A11):24505–24516, 2001.

H Todd, SWH Cowley, Mike Lockwood, DM Willis, and H Lühr. Response time of the high-latitude dayside ionosphere to sudden changes in the north-south component of the imf. *Plan. & Space Sci.*, 36(12):1415–1428, 1988.

Anastasios A Tsonis and Paul J Roebber. The architecture of the climate network. *Physica A: Statistical Mechanics and its Applications*, 333:497–504, 2004.

Andrew P Walsh, Stein Haaland, Colin Forsyth, Amy M Keesee, Jennifer Kissinger, Kun Li, Andrei Runov, Josef Soucek, Brian M Walsh, Simon Wing, et al. Dawn-dusk asymmetries in the coupled solar wind-magnetosphere-ionosphere system: A review. *Ann. Geophys.*, 2014. doi: 10.5194/angeo-32-705-2014.

Jinhui Wang, Liang Wang, Yufeng Zang, Hong Yang, Hehan Tang, Qiyong Gong, Zhang Chen, Chaozhe Zhu, and Yong He. Parcellation-dependent small-world brain functional networks: a resting-state fmri study. *Human brain mapping*, 30(5):1511–1523, 2009.

Masakazu Watanabe, George J Sofko, Konstantin Kabin, Robert Rankin, Aaron J Ridley, C Robert Clauer, and Tamas I Gombosi. Origin of the inter-hemispheric potential mismatch of merging cells for interplanetary magnetic field by-dominated periods. *Journal of Geophysical Research: Space Physics*, 112(A10), 2007.

CL Waters, JW Gjerloev, M Dupont, and RJ Barnes. Global maps of ground magnetometer data. *Journal of Geophysical Research: Space Physics*, 120 (11):9651–9660, 2015.

D. R. Weimer. Correction to predicting interplanetary magnetic field (imf) propagation delay times using the minimum variance technique. *J. Geophys. Res.*, 109(A12):n/a–n/a, 2004. ISSN 2156-2202. doi: 10.1029/2004JA010691. URL `http://dx.doi.org/10.1029/2004JA010691`. A12104.

D. R. Weimer, D. M. Ober, N. C. Maynard, M. R. Collier, D. J. McComas, N. F. Ness, C. W. Smith, and J. Watermann. Predicting interplanetary magnetic field (imf) propagation delay times using the minimum variance technique. *J. Geophys. Res.*, 108(A1):n/a–n/a, 2003. ISSN 2156-2202. doi: 10.1029/2002JA009405. URL `http://dx.doi.org/10.1029/2002JA009405`. 1026.

DJ Williams. Dynamics of the earth's ring current: Theory and observation. *Space Science Reviews*, 42(3-4):375–396, 1985.

Kazuko Yamasaki, Avi Gozolchiani, and Shlomo Havlin. Climate networks based on phase synchronization analysis track el-nino. *Progress of Theoretical Physics Supplement*, 179:178–188, 2009.

Yiqun Yu and Aaron J Ridley. Response of the magnetosphere-ionosphere system to a sudden southward turning of interplanetary magnetic field. *J. Geophys. Res.*, 114(A3), 2009.

B Zhang, W Lotko, O Brambles, P Damiano, M Wiltberger, and J Lyon. Magnetotail origins of auroral alfvénic power. *Journal of Geophysical Research: Space Physics*, 117(A9), 2012.